

CHARACTERIZING THE SENSITIVITY OF 2DEG-BASED MAGNETIC FIELD
AND ULTRAVIOLET LIGHT SENSORS IN SPACE-SIMULANT
ENVIRONMENTS

A DISSERTATION
SUBMITTED TO THE DEPARTMENT OF AERONAUTICS AND
ASTRONAUTICS
AND THE COMMITTEE ON GRADUATE STUDIES
OF STANFORD UNIVERSITY
IN PARTIAL FULFILLMENT OF THE REQUIREMENTS
FOR THE DEGREE OF
DOCTOR OF PHILOSOPHY

Hannah S. Alpert
October 2020

© 2020 by Hannah Sara Alpert. All Rights Reserved.

Re-distributed by Stanford University under license with the author.



This work is licensed under a Creative Commons Attribution-Noncommercial 3.0 United States License.

<http://creativecommons.org/licenses/by-nc/3.0/us/>

This dissertation is online at: <http://purl.stanford.edu/dy471qr5529>

I certify that I have read this dissertation and that, in my opinion, it is fully adequate in scope and quality as a dissertation for the degree of Doctor of Philosophy.

Debbie Senesky, Primary Adviser

I certify that I have read this dissertation and that, in my opinion, it is fully adequate in scope and quality as a dissertation for the degree of Doctor of Philosophy.

Jim Plummer

I certify that I have read this dissertation and that, in my opinion, it is fully adequate in scope and quality as a dissertation for the degree of Doctor of Philosophy.

George Springer

Approved for the Stanford University Committee on Graduate Studies.

Stacey F. Bent, Vice Provost for Graduate Education

This signature page was generated electronically upon submission of this dissertation in electronic format. An original signed hard copy of the signature page is on file in University Archives.

Abstract

Instruments and vehicles used in space experience a wide range of extreme environments, including high and low pressures, hypervelocity impacts from micro-meteorites, radiation exposure, and high and low temperatures. A major challenge in space exploration is that the electronics used in satellites and space vehicles are often made of silicon; however, silicon-based electronics tend to fail at temperatures above 200°C. In order to operate in the high-temperature environments of outer space, these electronics often require external cooling mechanisms, thus adding further bulk, complexity, and cost to the system. Gallium nitride (GaN) has a much wider temperature range than silicon (up to 1000°C) and has also shown to be more radiation-hardened, making it a viable platform for robust space-grade electronics. In this thesis, I discuss the design, testing, and implementation of two different GaN-based sensors: a Hall-effect (magnetic field) sensor and a UV photodetector.

The first part of this thesis focuses on how changing the geometry of the Hall-effect sensor affects its sensitivity, offset, and noise behavior. The experimental results show that the octagonal AlGaN/GaN and InAlN/GaN Hall plates follow the same behavior trends as theorized in the literature for silicon Hall plates: devices with the shortest contacts have the highest current-scaled sensitivity, while devices shaped as regular octagons have the highest voltage-scaled sensitivity. Low frequency noise is shown to increase with contact size, while at high frequency the dominant form of noise is thermal noise, for which an optimization on device shape is also described.

After comprehensively characterizing GaN-based Hall-effect sensors in an ambient environment, they are evaluated in various space-simulant environments. The main focus is on high temperature environments; the sensitivity of AlGaN/GaN and InAlN/GaN devices is characterized between room temperature and 576°C. Both devices show decreasing voltage-scaled magnetic sensitivity at high temperatures, but little hysteresis over 2-3 thermal cycles and nearly full recovery of initial sensitivity at room temperature. Additionally, current-scaled sensitivities remain stable over the temperature range, due to the minimal temperature dependence of the electron sheet density on the 2-dimensional electron gas (2DEG). Stability at high temperature is further exhibited through long-term high temperature storage tests as well as a 10-day exposure to a Venus-analogue environment (460°C, 96.5 bar, CO₂ atmosphere).

The last section of this thesis details the characterization of an AlGaN/GaN photodetector in

a high temperature environment (up to 250°C) and discusses the reasons for its dramatic drop in responsivity at this high temperature. The photodetector is then implemented for combustion monitoring in two different hybrid rocket motor applications. In addition to successfully detecting the duration of the combustion, the measurements from the photodetector vary with oxygen-to-fuel ratio for a hybrid rocket motor igniter plume. Additionally, the measurements from the photodetector are used to estimate the flame temperature for the igniter plume as well as in the center of a solid transparent hybrid rocket motor fuel grain.

The results from thorough testing of GaN-based Hall-effect sensors and photodetectors suggest that this material platform is a good candidate for use in outer space and terrestrial harsh environments. Further, by demonstrating the functionality of these sensors on space systems, we contributed to increasing the technology readiness level of GaN-based sensors and pushing them one step closer towards industrial use.

Acknowledgments

I absolutely could not have completed my PhD without the technical and personal support from a huge group of people. First, I would like to thank my advisor, Prof. Debbie Senesky. She took a chance on me five years ago when she allowed me to join the lab with no background in aerospace engineering, let alone electrical engineering, device physics, or materials science. She gave me the time to learn, make mistakes, and figure it out, and offered invaluable guidance throughout the process. I am also grateful to her for allowing me to explore my interests and take (a lot of) time away from research to do multiple internships and learn more about the field as a whole. I mainly attribute the fact that I had such a positive and enriching experience at Stanford to Debbie – it’s been a true privilege to be advised by her.

I would also like to thank the other educators who helped me get where I am today. Grad school would never have happened without my undergraduate advisor, Prof. Louise Edwards, who introduced me to this thing called “research” and has continued to be a mentor and supporter. Many thanks to Prof. George Springer, who came to campus multiple times just to meet with me and discuss research and life advice, and has given me endless laughs. I’ll never forget the opening to his quals question: “Have you ever killed a chicken?” (answer: no, but if you had to kill one without any weapons you should use torsion). I’d also like to thank Prof. Jim Plummer, Dr. Xiaoqing Xu, the SNF/SNSF staff, and the Aero/Astro faculty for teaching me about device physics, fabrication, and what it means to be an engineer. I owe endless thanks to Helmut Köck and Udo Ausserlechner, my collaborators from Infineon in Austria. They welcomed me to Villach during my first year (when I had no idea what was going on) and since then have proven to be the technically-savvy people I know, always bringing enthusiasm to our meetings (which are at 5pm for them!), coming up with novel ideas, and willing to explain complicated concepts to me. I admire and am immensely grateful for their technical expertise and support. Finally, I want to thank the staff in the Aero/Astro department, especially Patrick Ferguson and Jenny Scholes, who are always willing to help me with anything department-related; the department would not even be close to functional without them!

This work could also not have been done without the other graduate students in the XLab. I owe a huge thank you to Dr. Caitlin Chapin, Dr. Karen Dowling, and Dr. Ananth Yalamarthi for answering millions of dumb questions from the moment I entered the lab through long after they

graduated, and also for being wonderful colleagues and friends. Also thank you to Dr. Ruth Miller, Dr. Jessica Frick, Savannah Benbrook, Tom Heuser, Ricardo Peterson, Ruiqi Chen, Max Holliday, Anand Lalwani, Jiya Janowitz, Jackie Machesky, Peter Satterthwaite, and the many other XLabbers who have given me technical input and put up with my antics throughout grad school.

I am endlessly thankful to the people who made my Stanford Aero/Astro experience so much fun: Tess, Phil, Vince, Jayant, Michelle, Adam, Matt, Jessie, Wally, Karen, and the rest of the 2015 incoming class. Thank you for always being down to play games, drink wine, go for hikes, and listen to me complain, and for building such a strong and fun community for me at Stanford. My other Bay Area friends also made the past five years more fun than I ever could have imagined: Brianna, Sarah, Ben, Mark, Steve, Allison... thank you for always being up for a backpacking trip, book club, board game, ski trip, you name it. And thank you to my close friends from high school and college who I could always count on to listen to me gripe, give me life advice, and even visit sometimes! Samantha, Katie, Katina – thank you for always being there for me.

I also want to thank my grandparents: Grandpa Phil, Grandma Ellen, Grandma Ruth, and Grandpa Arthur. Let's be honest – these are the only people who *might* actually read this thesis, and I am so grateful for their support throughout this process. Grandpa Phil and Grandma Ellen, you could be on my defense committee because you ask such good questions. Grandma Ruth and Grandpa Arthur, I am beyond honored that you were planning to fly across the country to come to my graduation, despite how much you dislike graduations (you and me both!). I am so lucky that you are my grandparents!

Finally, my family. Thank you to my best friends in the entire world, Leah and Daniel. You've pushed me to be where I am today just by being yourselves. (What kind of family do I have where I never win "smartest child"?!). More importantly, I am thankful to have siblings with whom I can talk about anything and be myself. Every second I spend with either (or especially, both) of you is full of laughter and joy, and I love you! Russell, thank you for being such a wonderful 3rd sibling to me – whether it's sending me recipes, going for bike rides, or welcoming me into your home, I'm really grateful to have you in my life. Kevin, thank you for being so supportive throughout my last year of grad school. It turns out, shelter-in-place is not so bad when I have someone to laugh about it with, and I feel insanely lucky to have you in my life. Last, but certainly not least, thank you to my incredible parents, Rebecca and Peter. Thank you for encouraging me to reach for the stars (literally) while being overwhelmingly supportive in every single way. Mom, you're the one person I know who surpasses my enthusiasm and constant need to be active, and I am thankful that you have instilled in me a passion for life, a sense of social justice, and the drive to be a good person. Dad, I know I can count on you to help me rationally make any decision (even if half the time the answer is "Just do what you want!" or "F*** 'em!") and to believe in me even when I don't believe in myself. Mom and Dad, you are the reason I am who I am today, and I will never be able to thank you enough. I love you!

Nomenclature

$(L/W)_{eff}$	Effective number of squares
λ	Ratio of length of sides with contacts to full perimeter of device
μ	Mobility [$\text{m}^2/\text{V}\cdot\text{s}$]
ϕ_b	Energy barrier [J]
ρ_c	Contact resistance [Ωcm^2]
a	Length of sides without contacts
B	Magnetic field [T]
b	Length of sides with contacts
f	Frequency [Hz]
G	Gain
G_H	Shape factor
I	Current [A]
k_B	Boltzmann constant
L_T	Transfer length [μm]
n_s	Sheet electron density [m^{-3}]
q	Electronic charge [C]
r_n	Scattering factor
R_{sh}	Sheet resistance [Ω/\square]
S_i	Current-scaled sensitivity [V/V/T]

S_v	Voltage-scaled sensitivity [V/A/T]
T	Temperature [K]
V	Voltage [V]
V_H	Hall-effect voltage [V]
V_n	Thermal noise [V]

Contents

Abstract	iv
Acknowledgments	vi
1 Introduction	1
1.1 Sensors for Automotive, Aerospace, and Embedded Power Systems	1
1.2 Sensors in Extreme Environments	2
1.2.1 Radiation in the Solar System	2
1.2.2 Current Solutions for Electronics in Extreme Environments	4
1.3 Emerging Semiconductor Materials for Extreme Environment Applications	4
1.3.1 GaN Heterostructures	5
1.4 Thesis Contributions	7
1.5 Thesis Overview	7
2 Background	9
2.1 Magnetic Field Sensors	9
2.1.1 Hall-Effect Sensors	12
2.2 Ultraviolet Photodetectors	20
2.2.1 Operation of AlGa _N /Ga _N Photodetector	20
2.2.2 Optical Temperature Measurements Using Photodetectors	22
2.3 High-Temperature Degradation of Ga _N Sensors	23
2.3.1 Mobility	23
2.3.2 2DEG Sheet Density	25
2.3.3 Ohmic Contacts	27
3 Hall-Effect Sensor Geometry Optimization	31
3.1 Optimization for Sensitivity Performance	32
3.2 Optimization for Noise Performance	32
3.2.1 Types of Noise	32

3.2.2	Optimization for SNR with Respect to Thermal Noise	33
3.3	Final Device Geometries	34
3.4	Device Microfabrication	34
3.5	Experimental Testing	36
3.6	Sensitivity Results	39
3.7	Offset Results	40
3.8	Noise Results	40
3.9	Conclusions	44
4	Extreme Environment Characterization	46
4.1	High Temperature Testing	46
4.1.1	Experimental Setup for Sensitivity Tests	46
4.1.2	Characterization of Chuck Temperature	47
4.1.3	Voltage-Scaled Sensitivity	48
4.1.4	Current-Scaled Sensitivity	49
4.1.5	12-Hour High Temperature Exposure	50
4.1.6	Reliability and Accelerated Aging Testing	52
4.2	Outer Space Environments	56
4.2.1	Venus Chamber	56
4.2.2	KickSat-2	58
4.2.3	Radiation Testing	58
4.3	Conclusions	59
5	Ultraviolet Photodetectors	62
5.1	AlGa _N /Ga _N UV Photodetector	62
5.2	Device Calibration	63
5.3	Extreme Environment Characterization of UV Photodetectors	65
5.3.1	High Temperature Testing	65
5.3.2	Venus Chamber Testing	67
5.4	Photodetector for Combustion Monitoring	67
5.4.1	JPL Hybrid Rocket Motor Igniter Plume	69
5.4.2	Hybrid Rocket Motor Fuel Grain	75
5.5	Conclusions	79
6	Concluding Remarks and Future Work	80
6.1	Conclusions	80
6.2	Ongoing and Future Work	81
6.2.1	Implementation of Hall-Effect Sensors for Power Applications	81

6.2.2	Reliability and Accelerated Aging Testing	82
6.2.3	High Mobility Materials	83
6.2.4	Novel Methods to Measure AC Magnetic Fields	84
6.2.5	Spinning Frequency	84
6.2.6	Final Remarks	85
	Bibliography	86

List of Tables

2.1	Current-spinning measurement phases. © 2019 IEEE.	18
3.1	Parameters used in optimization of Hall-effect device contact lengths.	35
3.2	Relative design parameters of varied Hall plate geometry.	36
3.3	Sensitivity results. © 2019 IEEE.	40
3.4	Mean offsets of AlGa _N /Ga _N Hall plates at low bias (<300 μ A). © 2019 IEEE. . . .	41
3.5	Mean offsets of InAl _N /Ga _N Hall plates at low bias (<300 μ A). © 2019 IEEE. . . .	41
3.6	Thermal noise results.	43
3.7	Parameters related to noise for devices of different geometries. The thermal noise is calculated for 100- μ m devices and the cutoff frequency is measured at \sim 0.5 V. . . .	43
4.1	Comparison of temperatures measured by the thermocouple (TC) and the resistance temperature detector (RTD). Reprinted from [73], with the permission of AIP Publishing.	48
4.2	Sheet resistance, mobility, and 2DEG carrier concentration of devices that were exposed to a Venus environment and identical devices that had not be exposed.	58
5.1	Values associated with various test conditions. © 2019 IEEE.	69

List of Figures

1.1	Temperature range of planets in the Solar System.	3
1.2	Potential application spaces for GaN sensors.	5
1.3	Formation of the 2DEG in an AlGaIn/GaN heterostructure due to spontaneous and piezoelectric polarization.	6
1.4	Monolithic integration of sensors and supporting circuitry on an AlGaIn/GaN platform.	7
2.1	A comparison of a selection of magnetic field sensing technologies, where red, yellow, and green cells indicate increasingly desirable properties.	10
2.2	Worldwide market breakdown of magnetic field sensing technologies in 2016 [36].	13
2.3	Operation of a brushless DC motor (BLDC).	13
2.4	Operating principle of Hall-effect sensor. Reprinted from [73] with the permission of AIP Publishing.	14
2.5	Illustration of effective number of squares ($(L/W)_{eff}$).	15
2.6	Sensor offset.	16
2.7	Four phases of current spinning.	17
2.8	Absolute values of the offset voltages of individual phases (colored lines) and the resulting offset when all phases are added (black line) as a function of bias current, for octagonal InAlN/GaN device with equal sides and an internal resistance of $431 \pm 2 \Omega$. © 2019 IEEE.	18
2.9	(a) Restricted conduction path due to formation of a reverse bias during operation in Si Hall-effect sensor. (b) GaN Hall-effect sensor with carriers confined in the 2DEG, reducing the effect of resistive asymmetries that result in offset. © 2020 IEEE.	19
2.10	Band diagrams and operation principle of (a) MSM photodetectors and (b) AlGaIn/GaN photodetectors. Reprinted (adapted) with permission from P. F. Satterthwaite, A. S. Yalamarthy, N. A. Scandrette, A. K. M. Newaz, and D. G. Senesky. High responsivity, low dark current ultraviolet photodetectors based on two-dimensional electron gas interdigitated transducers. ACS Photonics, 5(11):4277–4282, 2018. Copyright 2018 American Chemical Society.	21

2.11	Diagram showing operation of interdigitated AlGaIn/GaN photodetector.	22
2.12	Contribution of various scattering mechanisms to total carrier mobility in AlGaIn/GaN 2DEG. Reprinted from “S. Birner. Mobility in two-dimensional electron gases (2DEGs). www.nextnano.de/nextnano3/tutorial/1Dtutorial_2DEGmobility.htm .”	24
2.13	Diagram of Ohmic contact layers on GaN before and after rapid thermal anneal. . .	28
2.14	Auger electron spectroscopy (AES) atomic concentration depth profiles of rapid thermally annealed Ti/Al/Pt/Au Ohmic contacts. Reprinted from “M. Hou and D. G. Senesky. Operation of ohmic Ti/Al/Pt/Au multilayer contacts to GaN at 600°C in air. <i>Applied Physics Letters</i> , 105(8):081905, 2014.” with the permission of AIP Publishing.	28
2.15	Images of Ti/Al/Mo/Au contacts (a) before and (b) after thermal storage at 850°C for 5 hours. Adapted with permission from Springer Nature Customer Service Centre GmbH: D. Selvanathan, L. Zhou, V. Kumar, I. Adesida, and N. Finnegan. Long-term thermal stability of Ti/Al/Mo/Au ohmic contacts on n-GaN. <i>J. of Elec. Mater.</i> , 32:335–340, ©2003.	29
2.16	Images of Ti/Al/Ni/Au contacts after thermal exposure at 340°C for 2000 hours. The gray areas are Ga-rich and the white areas Au-rich. Reprinted from “M. Piazza, C. Dua, M. Oualli, E. Morvan, D. Carisetti, and F. Wyczisk. Degradation of TiAlNiAu as ohmic contact metal for GaN HEMTs. <i>Microelectronics Reliability</i> , 49(9):1222–1225, ©2009.” with permission from Elsevier.	30
3.1	$(L/W)_{eff}$ values that maximize Hall-effect sensitivities with respect to supply current (left) and supply voltage (right) in Equations 2.4 and 2.5. © 2019 IEEE.	32
3.2	$(L/W)_{eff}$ values that maximize SNRs with respect to supply current (left) and supply voltage (right) in Equations 3.3 and 3.4	34
3.3	Images of 100- μ m-diameter Hall plates with various geometries, where b is the length of the contacts and a is the length of the sides without the contacts. The device with point-like contacts is optimized for S_i , the device with short contacts is optimized for SNR/I, the device with equal sides is optimized for S_v , and the device with long contacts is optimized for SNR/V. © 2019 IEEE.	35
3.4	Fabrication process of AlGaIn/GaN and InAlN/GaN Hall-effect sensors.	37
3.5	Cross-sectional schematic of the material stack of the AlGaIn/GaN and InAlN/GaN Hall-effect sensors fabricated at the Stanford Nanofabrication Facility. Reprinted from [73] with the permission of AIP Publishing.	37
3.6	Diagram of test setup used to measure sensitivity and offset of Hall-effect sensors in ambient environment.	38

3.7	Output Hall voltage (after current spinning) versus magnetic field for one of the AlGa _N /Ga _N devices and one of the InAlN/Ga _N devices with a supply voltage of 300 μ A, showing linearity of the response in the range of -4 mT to 4 mT. All devices used in this study showed similar linear behavior. © 2019 IEEE.	38
3.8	Voltage-scaled and current-scaled magnetic sensitivity for various octagonal AlGa _N /Ga _N and InAlN/Ga _N Hall plates. Both sets of devices follow the predicted trend: the devices with equal sides have the highest S_v and the devices with point-like contacts have the highest S_i . The colored line shows the theoretical values based on sweeping λ between 0 and 1 and calculating G_H and $(L/W)_{eff}$; S_i varies directly with G_H , while S_v varies with $G_H/(L/W)_{eff}$. The error bars depict the standard deviation of the sensitivity values over multiple supply currents from 60 μ A to 1.2 mA. © 2019 IEEE.	39
3.9	Measured magnetic field offsets of the AlGa _N /Ga _N and InAlN/Ga _N devices with equal sides. Offsets tend to be <20 μ T at low bias currents (<300 μ A) and greater at higher bias currents (up to 1.2 mA). © 2019 IEEE.	41
3.10	Mean Hooge parameter for each geometry vs. corner frequency measured at \sim 0.5 V.	42
3.11	Summary of effect of geometry of Hall-effect sensor on various performance parameters.	45
4.1	Diagram of the experimental setup. During testing, the Hall-effect sensor was epoxied to an aluminum sheet placed atop the heating stage, and the device was wire bonded directly to pins connecting to electrical feedthroughs. Reprinted from [73], with the permission of AIP Publishing.	47
4.2	Image of test setup used to characterize difference of temperature between the control unit setting and the chuck itself. Reprinted from [73], with the permission of AIP Publishing.	48
4.3	Voltage-scaled sensitivity of (a) InAlN/Ga _N and (b) AlGa _N /Ga _N samples between room temperature and 576°C. Reprinted from [73], with the permission of AIP Publishing.	49
4.4	Mobility of AlGa _N /Ga _N and InAlN/Ga _N samples between room temperature and 576°C. Reprinted from [73], with the permission of AIP Publishing.	50
4.5	Current-scaled sensitivity of (a) InAlN/Ga _N and (b) AlGa _N /Ga _N samples between room temperature and 576°C. Reprinted from [73], with the permission of AIP Publishing.	51
4.6	2DEG sheet density of InAlN/Ga _N and AlGa _N /Ga _N samples as a function of temperature from room temperature to 576°C. The inset shows the AlGa _N /Ga _N 2DEG sheet density over temperature on tighter axes. Reprinted from [73], with the permission of AIP Publishing.	51

4.7	2DEG sheet density as a function of temperature, with first temperature cycle depicted with red markers and ensuing temperature cycles with gray. Reprinted from [73], with the permission of AIP Publishing.	52
4.8	Resistance of ten InAlN/GaN devices measured throughout 96-hour storage at 450°C.	53
4.9	SEM images of an InAlN/GaN device before the high temperature exposure and then after 8 hours, 16 hours, and 24 hours at 450°C. The last three images are all of the 50- μ m device with short contacts, while the first image is of the 100- μ m device of the same geometry.	54
4.10	Resistance of five AlGaIn/GaN devices measured throughout 368-hour storage at 450°C.	55
4.11	SEM images of two AlGaIn/GaN devices after being exposed to 450°C for 368 hours.	55
4.12	Resistance of eight AlGaIn/GaN devices measured throughout 24-hour storage at 600°C.	56
4.13	Voltage-scaled sensitivity vs. current-scaled sensitivity for three InAlN/GaN Hall-effect sensors before (solid points) and after (open points) exposure in Venus chamber.	57
4.14	Image of 5 mm \times 5 mm chip containing InAlN/GaN Hall-effect sensors and the KickSat-2 motherboard on which they were integrated.	59
4.15	NASA image of the Cygnus spacecraft docked with the ISS, where KickSat-2 can be seen attached near the docking arm of the ISS.	60
4.16	Plot of Hall-effect sensor measurements from KickSat-2 over 8 days in orbit.	61
4.17	Plot of resistance measurements across Hall-effect sensors during exposure to \sim 20 krad of gamma radiation.	61
5.1	Image and cross-sectional diagram of AlGaIn/GaN UV photodetector.	63
5.2	Spectral responsivity vs. wavelength, measured at a bias voltage of 5 V and incident power of 10^5 mW. © 2019 IEEE.	64
5.3	Plots of (a) responsivity versus incident power and (b) current versus incident power for a wide range of incident optical powers.	64
5.4	Plots of (a) responsivity and (b) Normalized photocurrent to dark current ratio (NPDR) versus temperature. © 2019 IEEE.	65
5.5	Expected trend of responsivity vs. temperature for devices with varying gap widths between electrodes. If the increase in electron-hole recombination rate is the main contributor to the responsivity reduction at high temperature, then devices with wider gaps would exhibit a greater decrease in responsivity.	66
5.6	Plots of peak wavelength versus temperature for (a) measured data and (b) theoretical calculations. © 2019 IEEE.	67
5.7	Response of photodetectors before and after exposure to Venus-analogue environment.	68
5.8	SEM images of photodetector contacts on photodetectors that (a) had not been exposed to Venus-analogue environment and (b) had been exposed to the Venus-analogue environment.	68

5.9	(a) Image of photodetector setup. The sensor is being held by the clamp on the left and the igniter plume is emitted from the hole in the middle. (b) Schematic of flame and photodetector where d is the radial distance between the two, l is the length of the flame, and r is the radius of the flame. © 2019 IEEE.	69
5.10	Plot of current measured across the photodetector versus time for a series of three fires. © 2019 IEEE.	70
5.11	Images of (a) the igniter before the burn, (b) the igniter plume during the burn, and (c) the data from the photodetector throughout the course of the burn. © 2019 IEEE.	70
5.12	Plot of incident optical power versus O/F ratio, showing a trend of increasing optical power with increasing fuel concentration, and decreasing optical power with larger separation between photodetector and plume. © 2019 IEEE.	71
5.13	Plot of calculated average plume temperature vs. distance of the photodetector from the plume for the three O/F ratios. The inset shows that the average calculated plume temperature for each O/F ratio was between 880 K and 940 K. © 2019 IEEE.	73
5.14	Plot of theoretical nozzle temperatures over a range of O/F ratios for two different chamber pressures calculated using CEA. © 2019 IEEE.	74
5.15	Photograph of combustion reaction taking place in hybrid rocket motor fuel grain (image from F.S. Mechantel et al., <i>AIAA 2018 Propulsion and Energy Forum</i> , (2018)).	75
5.16	Image of 3D-printed holders that kept the AlGa _N /Ga _N (top) and commercial (bottom) photodetectors in place on the fuel grain.	76
5.17	Images of the hybrid rocket motor fuel grain before and during the burn.	76
5.18	Current output from top and bottom photodetectors in OSI sensors over the course of the hybrid rocket motor burn, placed near the fore end (1) and the aft end (2) of the fuel grain.	78
5.19	(a) Current output from an AlGa _N /Ga _N photodetector over the course of the hybrid rocket motor burn. (b) Output current (red dashed line) overlaid on top of calibration data (also shown in Fig. 5.3b).	78
6.1	(a) Image of InAlN/GaN Hall-effect sensor wirebonded to PCB. (b) and (c) Images of placement of sensor in the power electronics testbed at the University of Illinois Urbana-Champaign for current monitoring of the DC link between a rectifier and inverter.	82
6.2	Depiction of how Arrhenius model is used in calculating activation energy required for device failure.	83
6.3	Schematic showing operational principles of the 2ω technique.	84

Chapter 1

Introduction

1.1 Sensors for Automotive, Aerospace, and Embedded Power Systems

A sensor is a device that measures a physical quantity (e.g., temperature, pressure, vibration, chemical concentration, displacement, magnetic field, light intensity) and converts it into an electrical (or otherwise-readable) signal. Sensors are widely used in industries spanning consumer electronics, environmental monitoring, medical equipment, industrial automation, transportation, and communication, among several others. A 2019 market research report indicates that in 2017 the global sensor market was valued at \$139 billion, and it is expected to grow to \$287 billion by 2025, mainly fueled by increased usage of smart phones and other electronic devices, advances in automation, and the growing trend towards internet of things (IoT) [1].

The automotive industry is one of the largest consumers of sensors, comprising over 20% of the market share [2]. There are 60 to 100 sensors in a single car [3], monitoring everything from door and window positions to battery and engine temperatures to fuel and oil levels, and also providing other safety functions like rollover detection and crash sensing [4]. As cars trend towards more autonomy, an increased number of sensors will be required to ensure the safety and reliability of vehicles on the roads. In the aerospace sector, sensors serve similarly critical functions; these include inertial navigation, structural health monitoring, and heat flux sensing for thermal management purposes, among others [5]. Within the power electronics arena, sensors are used to monitor the high currents, voltages, and temperatures that these devices experience. As automotive, aerospace, and power electronic systems become progressively more autonomous and complex, the need for miniaturized sensors with increased accuracy, robustness, and reliability grows ever greater.

1.2 Sensors in Extreme Environments

There is a growing need for electronic components, including sensors, that can operate under extreme conditions, specifically in downhole environments, in industrial systems, and in outer space. These harsh environments may include extremely high and low temperatures, high heat fluxes and thermal cycling, hypervelocity impacts, large accelerations, exposure to caustic chemicals, high and low pressures, and high doses of radiation [6]. Electronics are being operated in these sorts of environments every day in automobile and airplane engines, down-hole oil exploration and well logging, and implanted biomedical devices [7], but further improvements are needed to increase the efficiency and reliability of sensors in these applications, as well as to open doors further into outer space.

Environments can vary dramatically within the space domain alone, and thus designing components for space applications comes with several challenges which may differ depending on the mission. Our nearest neighboring planet, Venus, has an average surface temperature of 470°C , an atmosphere that is predominantly made up of CO_2 , sulfuric acid clouds, and an average atmospheric pressure at the surface of 93 bar (over 90 times that of Earth) [8, 9]. Further, the combination of the 225-day orbital period and the 243-day rotational period causes each solar day to be equivalent to 117 Earth days, meaning that a given spot on the surface is in sunlight and then darkness for 58.5 days each [8]. These harsh conditions have made it very difficult to study the Venusian core, surface, and atmosphere; no probe has survived on Venus for longer than the Soviet lander Venera 13, which lasted a mere 127 minutes.

Another body that has garnered significant scientific interest is Jupiter's moon Europa, which is thought to have the potential for life due to its subsurface liquid water ocean [10]. In contrast to Venus' high surface temperatures, Europa's surface temperatures average -150°C to -180°C [6, 9]. Within the planets in our Solar System alone, the surface temperatures can range from close to -300°C on Pluto (technically not a planet, but still interesting to study) up to nearly 500°C on Venus (Fig. 1.1). Many spacecraft also experience high temperatures due to solar heating and power dissipation [11].

Beyond the extremely cold environment, the high radiation dose of 20-40 krad/day [6] poses further challenges to sending instruments to study the environment.

1.2.1 Radiation in the Solar System

Radiation comes from many sources throughout the universe, and there are multiple mechanisms through which radiation exposure can damage electronics. Solar wind, solar flares, and galactic cosmic radiation can produce energetic protons, electrons, heavy ions, and photons that have potentially harmful interaction with electronics. Additionally, there are regions around Earth known as the Van Allen Belts that have high concentrations of charged particles, which are trapped there due to Earth's magnetic field [9, 12, 13]. These forms of radiation can manifest themselves in different

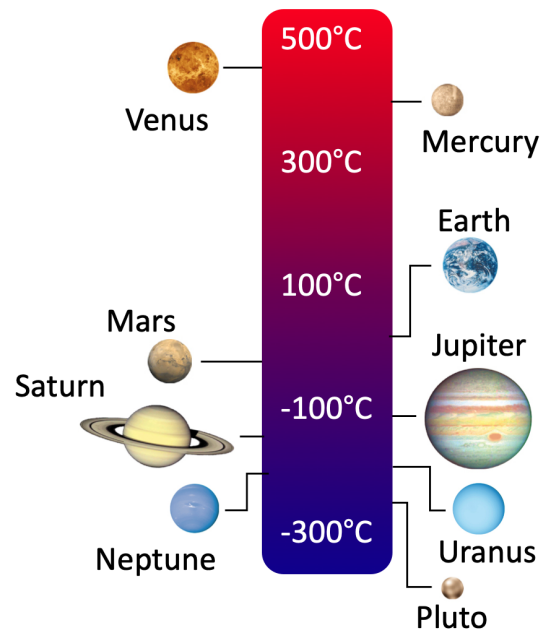


Figure 1.1: Temperature range of planets in the Solar System.

ways to damage electronics. **Total ionizing dose (TID)** effects are caused by excess energy being deposited into a material, breaking bonds and creating point defects that can trap charge [9]. This can lead to macroscopic effects in device performance, such as increased leakage current [13]. **Displacement effects** occur when the energy supplied to an atom by an incident ion knocks it out of its original position, displacing the atom and creating a vacancy. This can disturb device operation by creating new current paths and thus increasing leakage currents and background noise, or making flow less efficient in regions designed for conduction [12, 13]. **Single event effects (SEE)** occur when a high energy particle passes through the part. This can result in the switching of a transistor, a logic state switch in a digital circuit, or a bit flip in a variety of other flight-critical systems [9].

Satellites experience a range of radiation doses depending on their orbital paths. Satellites in low-Earth orbit (LEO), such as Earth-observation satellites and the International Space Station, orbit at an altitude of 100 to 1000 km and experience radiation doses of ~ 0.1 krad/year, mostly coming from galactic cosmic rays and solar flares. Geostationary satellites are those in geosynchronous Earth orbit (GEO). At an altitude of 36,000 km, they are exposed to ~ 10 krad/year from solar flares and cosmic rays as well as some charged particles in the outer Van Allen belts. Satellites in medium Earth orbit (MEO) like GPS constellations are exposed to the harshest conditions, as they are well within the Van Allen belts and can experience dose rates of ~ 100 krad/year. In addition to high doses of radiation, orbiting spacecraft are often exposed to extreme temperature swings between -120 and 150°C depending on their proximity and orientation with respect to the Sun [9].

1.2.2 Current Solutions for Electronics in Extreme Environments

Scientists and engineers have implemented ways to partially mitigate the effects of exposure to extreme temperatures and radiation doses. Electronics are often integrated with external cooling mechanisms to maintain operational temperatures, such as thermal insulation to passively keep the electronics cool, radiators to radiate excess heat into space, and active refrigeration techniques [14]. Radiation effects from TID can be reduced through shielding, because particles lose energy as they are transported through the extra layers of material, resulting in not enough energy to damage the electronics. For particles that are not sufficiently blocked by shielding, such as high energy protons and galactic cosmic rays, circuit level mitigation may be implemented to detect and correct errors. In addition, mission-critical parts may be duplicated or tripled in order create redundancy and thus ensure fault tolerance [13]. Implementing these cooling and shielding processes comes with several drawbacks. They require additional power and contribute further bulk and complexity to the system, leading to increased size, weight, and overall costs of the system [6]. Additionally, packaging can introduce more stress into the system and comes with the added threat of contamination during assembly [5]. Thus, components that can operate at extreme temperatures with minimal cooling and shielding are necessary for achieving higher efficiency, higher reliability, and lower cost systems.

1.3 Emerging Semiconductor Materials for Extreme Environment Applications

Electronic components are typically made of silicon due to its low cost, ease of fabrication, and complementary metal-oxide-semiconductor (CMOS) compatibility; however, silicon's narrow bandgap of 1.1 eV limits its functionality to temperatures below 200°C [15, 16]. This temperature limitation can be overcome by using materials with wide bandgaps, such as silicon carbide (SiC), aluminum nitride (AlN), diamond, and gallium nitride (GaN) [17, 18, 19]. The wide bandgap of these materials leads to a much lower intrinsic carrier concentration (n_i), as per Eq. 1.1,

$$n_i = \sqrt{N_C N_V} e^{-E_g/2k_B T} \quad (1.1)$$

where N_C is the effective density of states for the conduction band, N_V is the effective density of states for the valence band, E_g is the bandgap, k_B is Boltzmann's constant, and T is temperature. The room temperature intrinsic carrier concentration, n_i , for GaN ($E_g = 3.4$ eV) is $\sim 10^{-10}$ cm $^{-3}$, while for Si it is on the order of 10^{10} cm $^{-3}$ [17]. Intrinsic doping concentration increases with temperature; this, is problematic for silicon electronics, which rely on doped regions to function. When the intrinsic carrier concentration approaches the doping concentration, the devices stop working. Silicon is seldom doped beyond $\sim 10^{20}$ cm $^{-3}$ due to the solubility limit of dopants in

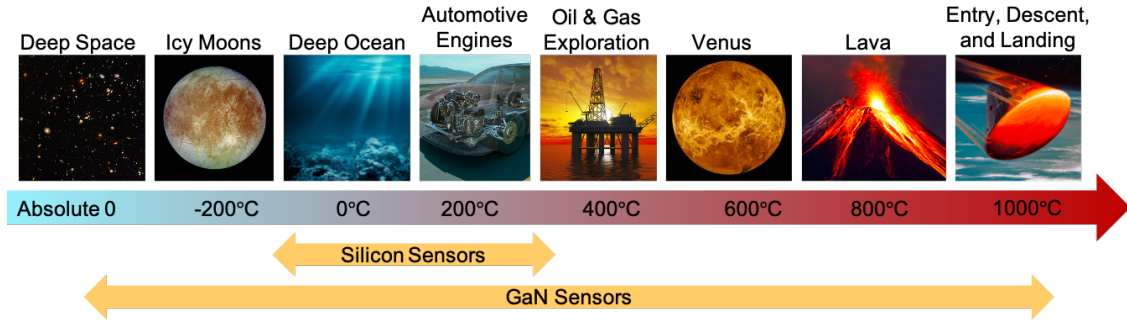


Figure 1.2: Potential application spaces for GaN sensors.

silicon [20]. Therefore, lightly doped regions must be doped to concentrations well below the heavy-doping limit. The intrinsic carrier concentration nears the value of lightly doped regions (10^{14} - 10^{17}) at a temperature of $\sim 200^\circ\text{C}$ [17], rendering many devices unusable in this temperature range.

Meanwhile, heterostructures made using GaN have previously shown operation up to 1000°C [21]. They have also exhibited radiation hardness beyond that of silicon [22, 23], due to a higher mean displacement energy (energy required to displace an atom from the lattice) than silicon [24]. These two robustness properties make GaN a potentially viable material for space applications. It has additionally become a promising material platform for power electronics due to its high breakdown field and potential for monolithic integration with silicon electronics [25], and may be suitable for use in other industries that experience harsh environments, such as oil and gas exploration (Fig. 1.2).

1.3.1 GaN Heterostructures

GaN heterostructures have a 2-dimensional electron gas (2DEG) that is formed when a nanometers-thick layer of unintentionally doped aluminum or indium aluminum nitride (AlGaIn or InAlN) is deposited on an underlying GaN layer. An electric field across the III-nitride layer is set up due to both spontaneous polarization (due to the difference in charge between the gallium and nitrogen atoms, which separates to form a dipole) and piezoelectric polarization (due to the different in lattice constant between the two layers, inducing strain at the interface), as shown in Fig. 1.3 [26, 27]. In AlGaIn/GaN heterostructures the contributions from spontaneous polarization and piezoelectric polarization are fairly equal [28]. However, with the appropriate aluminum concentration (17%) InAlN/GaN heterostructures may be lattice-matched, and thus all the polarization field is entirely due to spontaneous polarization.

Because the GaN and the alloy have different bandgaps, there is a discontinuity in their conduction bands when they are brought together (Fig. 1.3d). If the AlGaIn or InAlN layer is beyond a critical thickness, the GaN will dip below the Fermi level. This thickness is defined by the energy

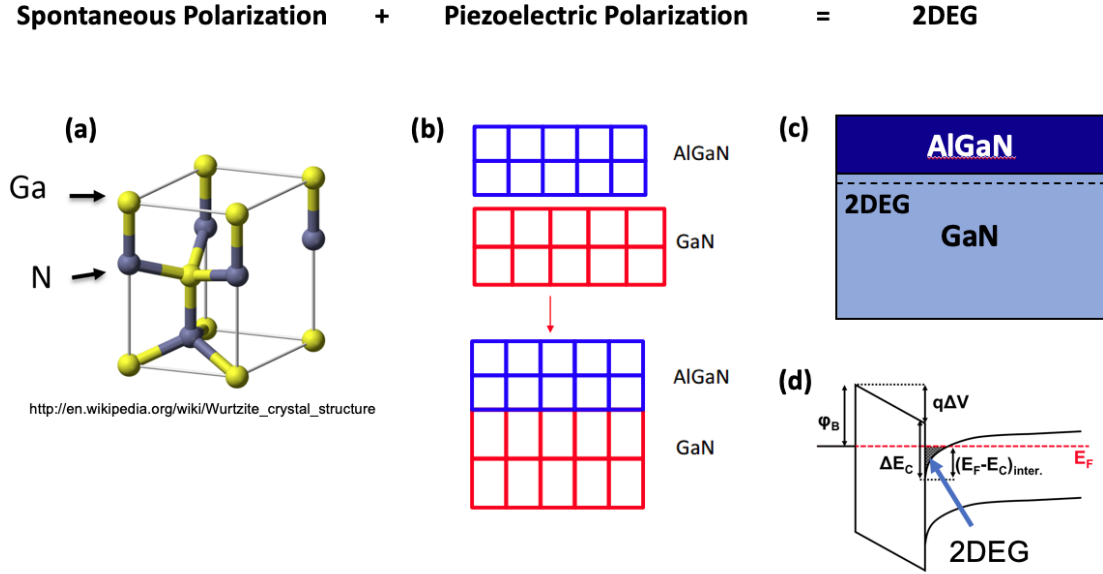


Figure 1.3: Formation of the 2DEG in an AlGaN/GaN heterostructure due to spontaneous and piezoelectric polarization.

level of the surface donor states (E_D) and the difference between the conduction band levels of GaN and the alloy (ΔE_C); the alloy layer must be thick enough such that the conduction band of GaN is below the Fermi level at the interface. The source of electrons differs for different material platforms. In AlGaAs/GaAs heterostructures, the electrons come from the doped AlGaAs layer. GaN-based heterostructures are *unintentionally doped*, meaning that dopants are not added to either layer during the fabrication process. Instead, the source of electrons are the surface states, which act as electron donors [29]. These electrons are carried by the electric field and accumulate at the interface, forming a quantum well, known as the 2DEG [30, 31, 28]. The 2DEG sheet carrier concentration depends on several parameters, including thicknesses of the two layers, the dielectric constants of the layers, the polarization of the layers, the Schottky barrier height, and the conduction band offset at the interface [32]. The 2DEG has a high electron mobility (1500 to 2000 $\text{cm}^2/\text{V}\cdot\text{s}$ at room temperature for AlGaN/GaN [15, 22, 33, 34, 35]), and can be leveraged for many sensing applications (Fig. 1.4). The high mobility, combined with the aforementioned low intrinsic carrier concentration, gives GaN-based heterostructures the ability to thrive in high temperature environments [17]. Thus, AlGaN/GaN heterostructures are useful for a variety of sensing applications and have the potential to be monolithically integrated with supporting circuitry (Fig. 1.4).

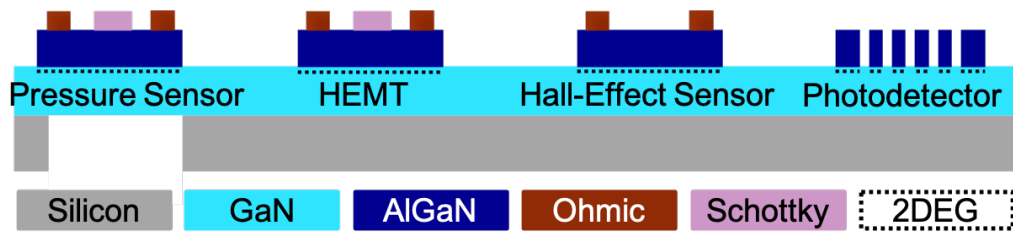


Figure 1.4: Monolithic integration of sensors and supporting circuitry on an AlGaIn/GaN platform.

1.4 Thesis Contributions

The major contributions of this thesis are the following:

- Conducted the first comprehensive experimental validation of how the shape factor affects Hall-effect sensor sensitivity. The results also show that 2DEG-based Hall plates have the same geometry-dependent properties as silicon-based devices.
- Characterized the sensitivity of InAlN/GaN and AlGaIn/GaN Hall-effect sensors up to a record-high temperature of 576°C. The continued operation of the devices at high temperature (over multiple thermal cycles) and subsequent recovery of original sensitivity after being returned to room temperature suggest that the high temperature exposure has little to no permanent effect on the device. Along with results from the Venus chamber, these results demonstrate the viability of the material platform, including the Ohmic contact stack, for use in high temperature and space applications.
- Raised the technology readiness level (TRL) of GaN-based sensors by demonstrating their functionality on space systems. We demonstrated the viability of GaN-based Hall-effect sensors in a Venus-analogue environment and on a CubeSat in space. Additionally, we characterized the responsivity of AlGaIn/GaN UV photodetectors up to 250°C and demonstrated the use of this device for combustion monitoring on a hybrid rocket motor.

1.5 Thesis Overview

- Chapter 2 lays the technical foundation for the reader to understand the details and results presented in the subsequent chapters. This chapter first discusses the applications and operational principles of Hall-effect sensors and UV photodetectors. We then review the possible high-temperature degradation modes of AlGaIn/GaN and InAlN/GaN-based sensors.
- Chapter 3 describes the design, fabrication, and testing of Hall-effect sensors with varying geometries. In particular, this chapter discusses how changing the length of the Ohmic contacts affects the sensitivity and noise behavior of the device.

- Chapter 4 examines the behavior of the GaN-based Hall-effect sensors under extreme temperatures and a Venus-analogue environment, and the implications of the results for the material platform.
- Chapter 5 covers the characterization of AlGaIn/GaN photodetectors in high temperature environments and the mechanisms driving their changing performance characteristics. This is followed by a discussion of two experiments that demonstrated the use of UV photodetectors for combustion monitoring in hybrid rocket motors.
- Chapter 6 provides conclusions and proposed next steps to further the work on sensors for extreme environments.

Chapter 2

Background

2.1 Magnetic Field Sensors

The magnetic field sensing industry had a market value in 2016 of \$1.64 billion, which is expected to increase to \$2.52 billion by 2022 [36]. There are many different technologies that can be used to measure magnetic fields, which span a huge range of costs, sizes, operating principles, and application spaces. A selection of magnetic field sensing technologies is discussed here, and a subset of these is summarized in Fig. 2.1.

SQUID Magnetometer

SQUID (superconducting quantum interference device) magnetometers rely on the principle of superconductivity – at extremely cold temperatures, the electrical resistance of certain materials drops to nearly zero. Additionally, magnetic flux lines cannot exist within a superconducting region. Thus, if a ring-shaped superconducting material is in a magnetic field and then cooled to below its transition temperature, the flux inside the ring gets trapped. When the magnetic field is removed, there is current induced around the ring to keep the flux on the inside of the ring constant; this current does not decay because the material has no electrical resistance. Finally, if the loop of superconducting wire is interrupted by a small resistive region (Josephson junction), electrons will tunnel across from one superconducting region to the other, according to the Josephson effect [37]. There is a measurable voltage drop across the junction, with the period of voltage variation changing with a resolution of a single flux quantum [38]. Thus, SQUID magnetometers are among the most sensitive and lowest-noise of all magnetic sensing technologies [39], leading them to be used for high-precision geophysics and medical applications (e.g., neuromagnetism, magnetocardiography, liver magnetic susceptibility) [37]. A major drawback of these sensors, however, is that they require cryogenic temperatures to operate, leading to strict packaging requirements, larger sizes, and high costs.





	SQUID 	Fluxgate 	Magnetoresistive 	Hall-Effect 
Cost	\$100,000	\$1000	\$1	< \$1
Size	cm → m	cm	μm → mm	μm → mm
Accuracy	10 ⁻¹⁵ T	10 ⁻⁹ T	10 ⁻⁶ T	10 ⁻⁴ T
Complexity				
Operating Principle	Electrons tunnel between superconducting regions	Magnetic susceptibility of core	Resistance varies with external B-field	Voltage generated proportional to B-field
Uses	Biomagnetism Geophysics	Vehicle detection Archaeology Drilling	Compasses Hard drives	Motor position & speed Automotives
Limitations	Requires cryogenic operation	Size/complexity vs. accuracy	Non-linear	Noisy Temperature sensitive

Figure 2.1: A comparison of a selection of magnetic field sensing technologies, where red, yellow, and green cells indicate increasingly desirable properties.

Proton Precession Magnetometer

Another type of extremely high-accuracy magnetic field sensor is the proton precession magnetometer. In this system, a proton-rich fluid such as hydrogen or kerosene sits in a tube around which a magnetic field is generated. The protons in the fluid align themselves with this field, and then when the magnetic field is removed they realign themselves with the ambient field. The realignment process does not happen instantly; rather, the protons precess at a frequency that is proportional to the ambient field, thus producing a rotating magnetic field that is picked up by an inductor and subsequently amplified [39]. Although the proton precession magnetometer has a low sample rate, large size, and high power consumption, it finds use in applications that require high sensitivity and are not size-constrained, such as archaeology, mineral exploration, and surveys of unexploded ordnance [40].

Optically Pumped Magnetometer

A third type of high-sensitivity sensor, also used in archaeology and geophysics, is an optically pumped magnetometer, which includes caesium vapour and potassium vapour magnetometers. In this type of system, there is a chamber containing an alkali-metal vapor between a laser and a photodiode. The laser beam is used to “optically pump” the atoms; after being hit by a photon, the atom is excited to a higher energy state, emits a photon, and falls to a lower energy state that is transparent to photons. Thus, light can completely pass through the optically pumped vapor and be detected by the photodiode. An external magnetic field causes the atoms to jump into

different polarization states, making the vapor no longer fully optically pumped. This variation in polarization changes the transparency of the vapor to the laser, and thus the output of the photodiode is proportional to the magnetic field strength [41].

Fluxgate Magnetometer

The type of magnetic field sensor most commonly used to measure the Earth's (and other planetary bodies') magnetic field is the fluxgate magnetometer. It is composed of a magnetically susceptible core wrapped by two coils of wire, wound in different directions. An alternating current passes through one of the coils, magnetizing, un-magnetizing, and inversely magnetizing the core, which in turn generates a current in the second coil that is read by a detector. In the absence of an external magnetic field the input and output currents match. However, when there is a magnetic field present, the core becomes more easily magnetized in one direction (the direction of the external magnetic field) than in the other. Therefore the current in the second coil varies proportionally to the external field. In addition to space applications, fluxgate magnetometers are often used in vehicle (e.g., submarine) detection, archaeology, and drilling because of its trade-off between sensitivity, stability, power consumption, and size [39, 42].

Search Coil (Inductive) Magnetometer

Search coil, or inductive, magnetometers are also commonly used in outer space, but because they only measure AC fields they are often used to measure electromagnetic waves in space plasmas. Their frequency range, sensitivity, size, mass, and power consumption make them suitable for this application [43]. Like the fluxgate magnetometer, the search coil magnetometer has a coil wound around a core of high magnetic permeability. In this case, there is no current sent through the coil; rather, when placed in a changing external magnetic field, the core concentrates the magnetic flux fluctuations inside the coils. According to Faraday's Law, a changing magnetic flux in a coil induces a voltage in the coil, and this voltage can be amplified and measured [39].

Magnetoresistive Devices

Magnetoresistive devices are one of the most widely used type of magnetic field sensors because they are cheap and have low power consumption. Magnetoresistance relies on the fact that the electrical resistance of particular materials changes in the presence of a magnetic field. *Ordinary magnetoresistance (OMR)* refers to this effect occurring in nonmagnetic metals, where the change in resistivity will be positive for both parallel and transverse magnetic fields. In *anisotropic magnetoresistive (AMR)* devices, a ferromagnetic strip is magnetized in a preferred direction during the fabrication process. This causes the change in resistivity to depend on the orientation of the magnetic field [44]. To increase the magnitude of the effect, *giant magnetoresistive (GMR)* devices

include alternating layers of ferromagnetic and non-magnetic materials. When no external magnetic field is present, half of the ferromagnetic layers will be oriented in one direction and half in the other. As the external magnetic field is increased, the orientation of the ferromagnetic layers lines up with the field, reducing the electrical resistance due to decreased scattering [45]. Finally, *tunneling magnetoresistance (TMR)* occurs when two ferromagnetic layers are separated by an insulating thin film of ~ 1 nm, through which electrons are able to tunnel. In this case, one of the ferromagnetic layers can be “pinned” to have a specific magnetic orientation, while the other layer will change orientation depending on the external magnetic field. When both layers are oriented in the same direction, more electrons are able to tunnel so the measured tunneling current will be large, whereas when the layers are oriented in opposite directions the tunneling current will be much smaller [46]. Magnetoresistive devices are often used in compasses and hard drives and for position sensing [39].

MEMS Magnetometers

Magnetometers that detect magnetic field based on motion (like a compass) have existed for a long time, but recently this same principle has been applied in the development of microelectromechanical systems (MEMS) magnetometers. An example of this type of device detects the motion of a miniature bar magnet, built by the electrodeposition of a permanent magnetic material. The bar lies perpendicular to a torsion beam about which it can rotate. The amount of rotation, and thus tip deflection, is proportional to the external magnetic field [47]. While these sensors have a small size, low power consumption, and the potential for IC compatibility, they are often very difficult to fabrication [39].

2.1.1 Hall-Effect Sensors

Magnetic field sensors based on the Hall effect are advantageous over other magnetic field sensing technologies because they are low-cost, easy to integrate with other circuit components, and linear over a wide range of magnetic fields [48]. These factors contribute to their widespread use in the automotive industry (e.g., valve positions, gear rotation speed, fuel tank level, seat-belt buckle clamping, heading determination, steering wheel angle), in power electronics for current sensing and anomaly detection, and within inertial measurement units (IMUs) for navigation and position sensing. In 2016, Hall-effect sensors comprised 71% of the market share of magnetic field sensing technologies worldwide (Fig. 2.2) [36].

Hall-effect sensors are used extensively to monitor the speed and position of rotating parts, particularly in brushless DC motors. In these motors, a current is sent through coils wrapped around the stator in an alternating fashion, thus generating alternating magnetic fields. The permanent magnet in the center rotates as it is attracted and repelled by the fields generated by the stator (Fig. 2.3). For many applications, it is essential to have accurate measurements of the position

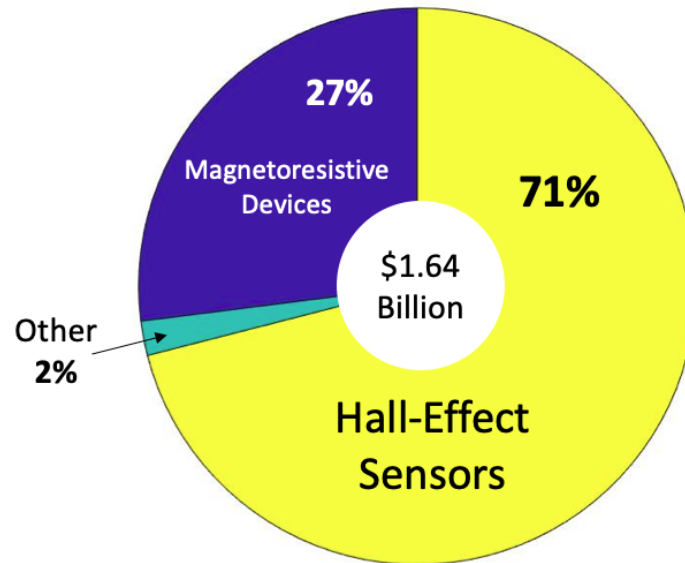


Figure 2.2: Worldwide market breakdown of magnetic field sensing technologies in 2016 [36].

and velocity of the rotor to feed back into the system; therefore, Hall-effect sensors (usually at least three) are integrated into the motor to determine its position and speed.

Applications of Hall-effect sensors within the space sector include current monitoring in hybrid rocket motors, power modules, and spacecraft motor control units [49, 50]. Additionally, their use for speed and position sensing of rotating parts have led them to be integrated into the robotic arm on the Mars rover (for improving accuracy of arm position for drilling), the wheels of the lunar roving vehicle, and reaction wheels in multiple satellites. A reaction wheel is a flywheel used by a satellite for attitude control. The orientation of the satellite can be adjusted by a slight change in the direction or speed of spinning of the reaction wheel – due to conservation of momentum, the

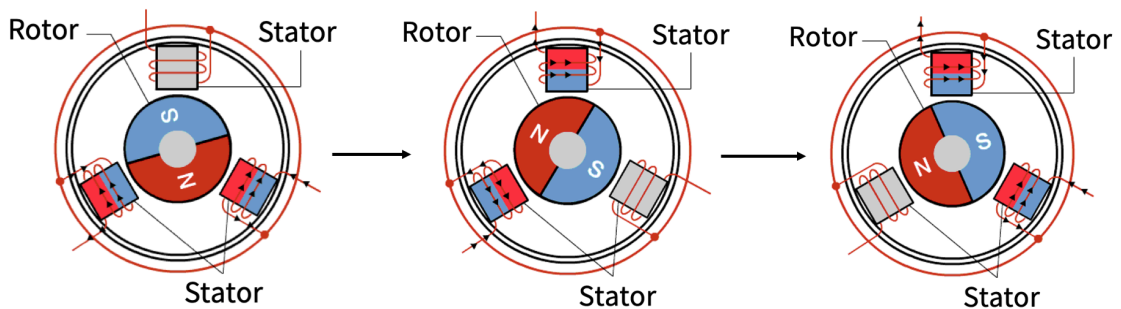


Figure 2.3: Operation of a brushless DC motor (BLDC).

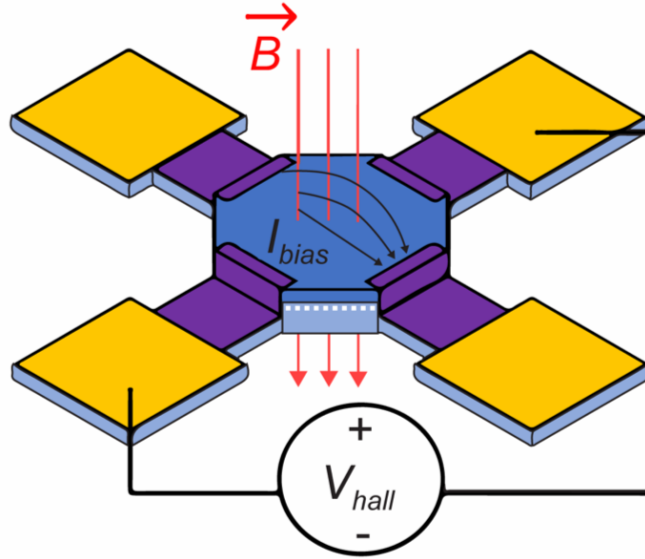


Figure 2.4: Operating principle of Hall-effect sensor. Reprinted from [73] with the permission of AIP Publishing.

orientation of the satellite will change accordingly. In space, Hall-effect sensors may endure a wide range of temperatures and harsh conditions that would not be experienced in terrestrial applications. Additionally, it currently costs about \$10,000 to launch one pound of payload into space [51]; thus, there is a need for robust sensors that can operate at high temperatures without bulky and complex external cooling and shielding mechanisms.

Principle of Operation

Hall-effect sensors are devices with four terminals where current is applied across two of them and voltage is measured across the other two. In the presence of a magnetic field perpendicular to the otherwise straight path of the current, the moving electrons experience a force (the Lorentz force), which bends their path. The bending of the path of the electrons results in an accumulation of charges; it is measured perpendicular to both the applied current (I) and the external magnetic field (B), and is known as the Hall voltage (V_H). The Hall voltage is defined as:

$$V_H = \frac{IBr_n G_H}{qn_s}, \quad (2.1)$$

where r_n is the scattering factor of the material (~ 1.1 for GaN) [52], G_H is the shape factor, q is the electronic charge, and n_s is the sheet electron density. A schematic showing the operating principle of a Hall-effect sensor is in Fig. 2.4.

The shape factor, G_H , accounts for the reduction in Hall voltage and change in linearity due to

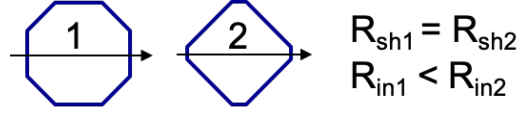


Figure 2.5: Illustration of effective number of squares $((L/W)_{eff})$.

the short-circuiting effect of having finite contacts [53, 54, 55]. For Hall-effect plates with four-fold rotational symmetry at low magnetic fields, G_H depends only on the geometry of the Hall-effect plate and the contacts. The magnetic field may be considered low if its magnitude multiplied by the Hall mobility is much less than unity [56], as is the case throughout this work. Under these conditions, G_H can be approximately written as a function of the effective number of squares $(L/W)_{eff}$ [57];

$$G_H \approx \frac{(\frac{L}{W})_{eff}^2}{\sqrt{(\frac{L}{W})_{eff}^4 + \frac{(\frac{L}{W})_{eff}^2}{2} + 4}}. \quad (2.2)$$

The effective number of squares, $(L/W)_{eff}$, is defined as the ratio of the internal resistance over the sheet resistance. Multiple devices of the same material but different shapes should all have the same sheet resistance (R_{sh}) but may have different internal resistances (R_{in}), as shown in Fig. 2.5.

The expression given in Eq. 2.2 is exact when $(L/W)_{eff} = \sqrt{2}$, and has an error of up to 2% for the geometries studied here [56]. The error can be reduced by over two orders of magnitude by multiplying the previously calculated G_H by the following factor:

$$1 + \Lambda \times e^{(-2.279 - (1.394 \times \Lambda)^2 + (0.6699 \times \Lambda)^4 - (0.4543 \times \Lambda)^6)} \quad (2.3)$$

where $\Lambda = \ln(\frac{(L/W)_{eff}}{\sqrt{2}})$, further described in [56].

Sensitivity

The sensitivity of a sensor is defined as the output divided by the input; thus, in the case of a Hall-effect sensor, the absolute sensitivity is the Hall voltage (output) divided by the external magnetic field (input). From the Hall voltage equation, it is clear that the Hall voltage also increases proportionally to the applied current (or voltage). To make the sensitivity independent of this additional applied parameter, the sensitivity can be scaled by the applied current (I) or applied voltage (V_s).

The sensitivity of a Hall-effect device scaled by supply current (S_i) is proportional to G_H and inversely proportional to n_s ;

$$S_i = \frac{V_H}{IB} = \frac{r_n}{qn_s} G_H. \quad (2.4)$$

The sensitivity scaled supply voltage (S_v) is proportional to both $G_H/(L/W)_{eff}$ and the Hall

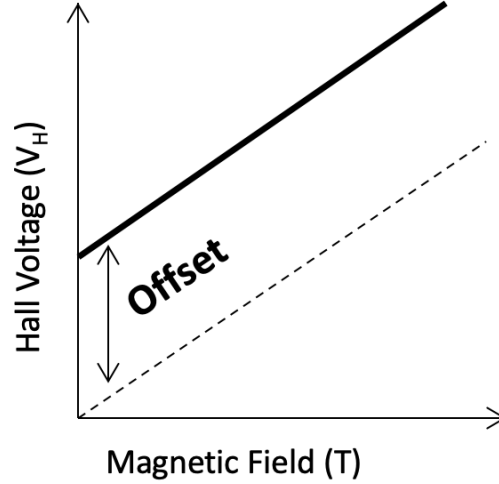


Figure 2.6: Sensor offset.

mobility of the electrons μ_H ;

$$S_v = \frac{V_H}{V_s B} = \frac{r_n G_H}{R q n_s} = \mu_H r_n \frac{G_H}{\left(\frac{L}{W}\right)_{eff}} \quad (2.5)$$

where R is device resistance. Equations 2.4 and 2.5 show that high Hall mobility is necessary for high voltage-related sensitivity and low sheet density is needed for a high current-related sensitivity.

Offset

In addition to high sensitivity, another desirable parameter in a Hall-effect device is low offset. From the Hall voltage equation, it would seem that when the external magnetic field (B) was 0, the Hall voltage would also be 0; however this is not actually the case. The offset voltage is defined as the Hall voltage measured in the absence of a magnetic field (Fig. 2.6).

Offset voltages are usually caused by mechanical stress, thermal gradients, geometrical errors, defects, and other irregularities within the device [58, 59]. Implementing current-spinning has been shown to reduce the offset voltage by a factor of over 1000 [60, 61]. In this method, the direction and polarity of the sourcing and sensing contacts are swapped, resulting in eight total configurations (phases) in which the Hall voltage is measured. The last four phases are identical to the first four phases, but the polarity of the voltage measurement is swapped in order to cancel out multimeter error. The first four phases are depicted in figure 2.7. Due to the measurement configurations (shown in Table 2.1, where the four contacts are labeled N, W, S, E corresponding to their location on the Hall plate), four of the Hall voltages are positive and four are negative. When these Hall voltages

are added together a large portion of the raw offset is canceled out, as shown in Figure 2.8.

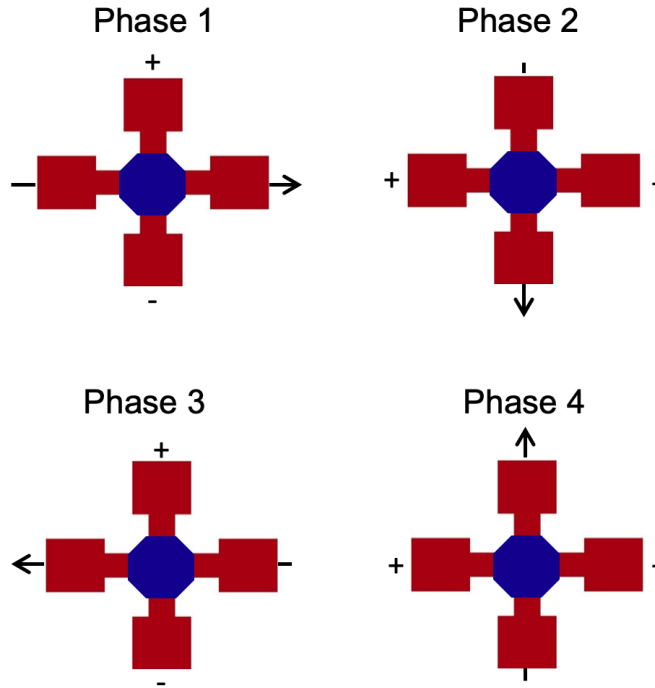


Figure 2.7: Four phases of current spinning.

The magnetic field offset (B_{off}) is calculated, using the Hall voltage after current-spinning, as

$$B_{off} = \frac{V_H}{V_s \times S_v}. \quad (2.6)$$

Even after implementing current spinning, small offsets still remain in the Hall-effect sensor measurements; this is known as the “residual offset”. Since spinning cancels out linear and non-directional offsets, residual offsets are generated by nonlinear or directional sources that may be external or internal to the sensor itself. External sources include stray fields in the test setup or packaging. These can be caused by poor shielding from the Earth’s magnetic field, magnetization of test boards, or magnetic fields generated by the current-carrying wirebonds. Other external sources of offset include noise in the measurement equipment and mechanical stress on the sensor [62].

A major internal source of offset is dynamic resistance asymmetry, which is caused by the formation of a p-n junction (and thus, depletion region) between the substrate and the active device layer. During operation of the sensor, a reverse bias will form and limit the conduction path, which results in an asymmetric resistance in the device (Fig. 2.9a) [63]. This asymmetry varies with supply

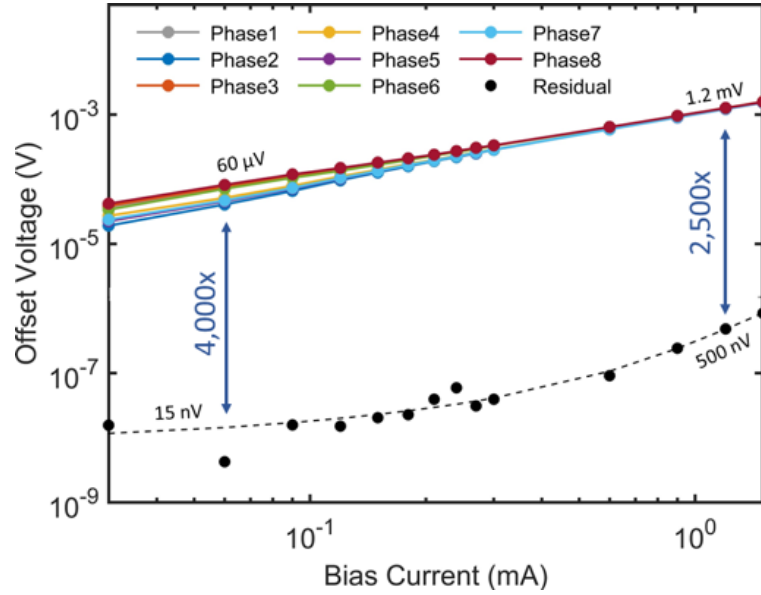


Figure 2.8: Absolute values of the offset voltages of individual phases (colored lines) and the resulting offset when all phases are added (black line) as a function of bias current, for octagonal InAlN/GaN device with equal sides and an internal resistance of $431 \pm 2 \Omega$. © 2019 IEEE.

current or voltage and will not be fully canceled by current spinning. Another source of internal offset is thermal gradients caused by Joule heating, which induces a voltage via the Seebeck effect. Joule heating is the process by which energy from a flowing current is converted into heat. This results in thermal gradients in the device, which in turn generate a thermoelectric voltage that do not fully cancel during current spinning due to their asymmetric nature. Other internal sources of offset include self-magnetic fields (a small magnetic field is generated due to current flowing across the device) and nonlinear or asymmetric contacts due to microfabrication error [62].

Phase #	I+	I-	V+	V-	Hall Signal
1	E	W	N	S	+
2	N	S	W	E	+
3	W	E	S	N	+
4	S	N	E	W	+
5	E	W	S	N	-
6	N	S	E	W	-
7	W	E	N	S	-
8	S	N	W	E	-

Table 2.1: Current-spinning measurement phases. © 2019 IEEE.

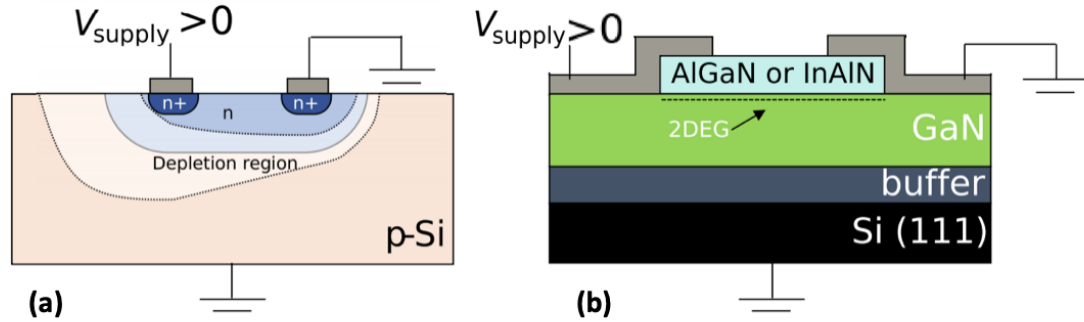


Figure 2.9: (a) Restricted conduction path due to formation of a reverse bias during operation in Si Hall-effect sensor. (b) GaN Hall-effect sensor with carriers confined in the 2DEG, reducing the effect of resistive asymmetries that result in offset. © 2020 IEEE.

GaN Hall-Effect Sensors

Silicon-based Hall-effect sensors are standard in the electronics industry. However, the limitations of silicon described in Section 1.3 make it less than ideal as a material platform for Hall-effect sensors that may experience harsh environmental conditions. In particular, silicon Hall-effect sensors rely on having doped regions, but at temperatures above $\sim 200\text{--}300^\circ\text{C}$, the intrinsic carrier concentration nears the dopant concentrations. Other materials currently used for commercial off-the-shelf (COTS) Hall-effect sensors include gallium arsenide (GaAs), indium arsenide (InAs), and indium antimonide (InSb); these semiconductors have extremely high electron mobilities (~ 8000 to $80,000\text{ cm}^2/\text{V}\cdot\text{s}$) and thus have higher sensitivity values than silicon sensors. While sensors made from these materials have extremely high sensitivities at room temperature and low temperatures, their narrow band gaps (0.17 to 1.4 eV) hinder their functionality at high temperature. Thus, they cannot be used in the extreme thermal environments found in space.

Alternatively, GaN-based Hall-effect sensors have shown room temperature sensitivity and offset characteristics similar to those of silicon Hall-effect sensors [64, 65, 66, 67, 68, 59, 54, 69], but also reliable operation up to 400°C [50, 70, 71, 15, 72] and beyond [73]. Further, 2DEG-based Hall-effect sensors have the potential for lower magnetic field offsets than silicon-based devices [74, 75, 76]. Offset caused by the resistive asymmetries, as described in Section 2.1.1, can be quite large in junction isolated silicon-based Hall-effect sensors [77], while 2DEG-based Hall-effect plates do not face this limitation (Fig. 2.9b).

2.2 Ultraviolet Photodetectors

Ultraviolet (UV) photodetectors are used for chemical analysis in environmental applications, optical communication between satellites, UV astronomy, flame detection for fire alarms, and combustion monitoring [78, 79]. The parameters that determine photodetector performance include signal-to-noise ratio, response time, dark current (the output from the sensor when there is no light shining on it), and responsivity [79, 80], among others. The responsivity (R) of a photodetector is analogous to the sensitivity of any arbitrary sensor: it is the ratio of the photocurrent, I_{photo} , (with the dark current, I_{dark} , subtracted off) to the incident optical power (P_{opt}):

$$R = \frac{I_{photo} - I_{dark}}{P_{opt}}. \quad (2.7)$$

It is desirable to have a low dark current both to improve the responsivity of the photodetector as well as to minimize its quiescent power. A parameter that incorporates both of these metrics is the normalized photocurrent-to-dark current ratio (NPDR) [81, 82, 83],

$$NPDR = \frac{R}{I_{dark}}. \quad (2.8)$$

Another important metric is the UV-to-visible rejection ratio, which describes the cross-sensitivity of the detector to visible light. A high UV-to-visible rejection ratio ensures that the majority of the output signal measured is in response to UV light as opposed to light at other wavelengths.

2.2.1 Operation of AlGaIn/GaN Photodetector

A standard metal-semiconductor-metal (MSM) photodetector consists of two metallic electrodes on a semiconductor material, forming Schottky contacts (band diagram shown in Fig. 2.10a). When voltage is applied across the electrodes, thermal generation of electron-hole pairs causes a small current (I_{dark}) to flow, as electrons drift towards the positive electrode and holes drift towards the negative electrode. When light shines on the device, photogeneration causes a significant increase in electron-hole pair generation, and thus a much larger current (I_{photo}) flows. The magnitude of the photocurrent scales with the intensity of the light [84, 85].

In an AlGaIn/GaN photodetector, AlGaIn electrodes are grown atop a GaN substrate; therefore, a 2DEG is present at each electrode (Fig. 2.10b). Similar to the MSM photodetector, there is a small dark current when no light is applied, due to thermal generation of electron-hole pairs. However, when light shines on the device and more electron-hole pairs are generated, the AlGaIn barrier keeps the holes from escaping, and as a result they accumulate at the interface. This accumulation lowers the barrier that the electrons in the 2DEG must overcome to generate a current, so the electrons require less energy to escape from the 2DEG well; thus a very high current flows [83].

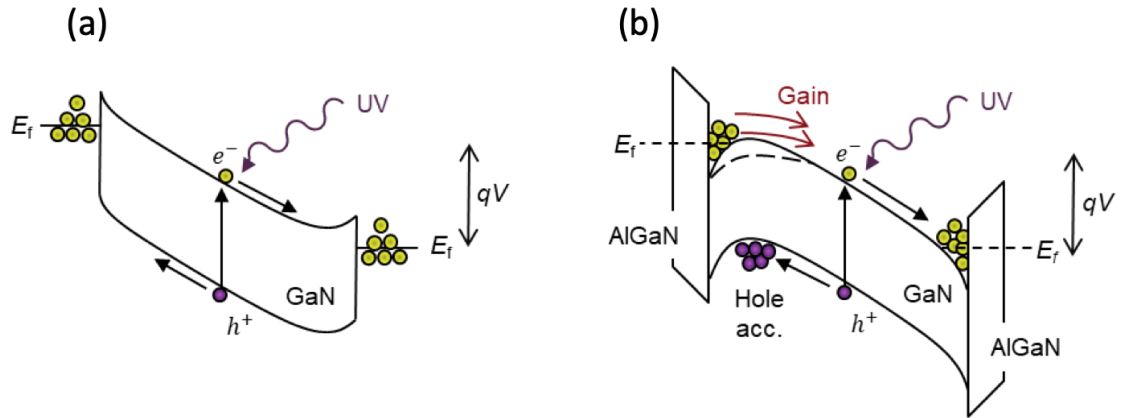


Figure 2.10: Band diagrams and operation principle of (a) MSM photodetectors and (b) AlGaIn/GaN photodetectors. Reprinted (adapted) with permission from P. F. Satterthwaite, A. S. Yalamarthy, N. A. Scandrette, A. K. M. Newaz, and D. G. Senesky. High responsivity, low dark current ultraviolet photodetectors based on two-dimensional electron gas interdigitated transducers. *ACS Photonics*, 5(11):4277–4282, 2018. Copyright 2018 American Chemical Society.

Many photodetector designs utilize interdigitated electrodes to improve response time and responsivity, as decreasing the distance between adjacent electrodes allows the electrons in the conduction band to be collected by the electrode before recombining [86, 87]. A diagram depicting the operation of an interdigitated AlGaIn/GaN photodetector is shown in Fig. 2.11.

Quantum Efficiency

The quantum efficiency (QE) of a photodetector measures that ability of the device to convert light energy into electrical current. It is defined as the ratio of the number of charges that jump into the conduction band and flow as current, to the number of photons that are incident on the surface of the device. The quantum efficiency may be limited by (1) fast recombination between the generated electron-hole pairs before they can be collected by the electrodes, and (2) incident light being reflected, rather than absorbed, at the surface of the device [88, 84]. While some photodetector architectures (e.g., photoconductors [89], phototransistors [90]) are conducive to quantum efficiencies well above 100% due to their internal gain mechanisms, MSM photodetectors tend to be limited. Despite their lower QEs, MSM photodetectors are still preferred in some applications because of their fabrication simplicity, low cost, high speed operation ability, and potential to be co-fabricated or monolithic integration with transistors and other circuit components [84]. The AlGaIn/GaN photodetector described in this thesis has many of the same advantages as MSM photodetectors without compromising its extremely high quantum efficiency due to the internal gain mechanism described above [83].

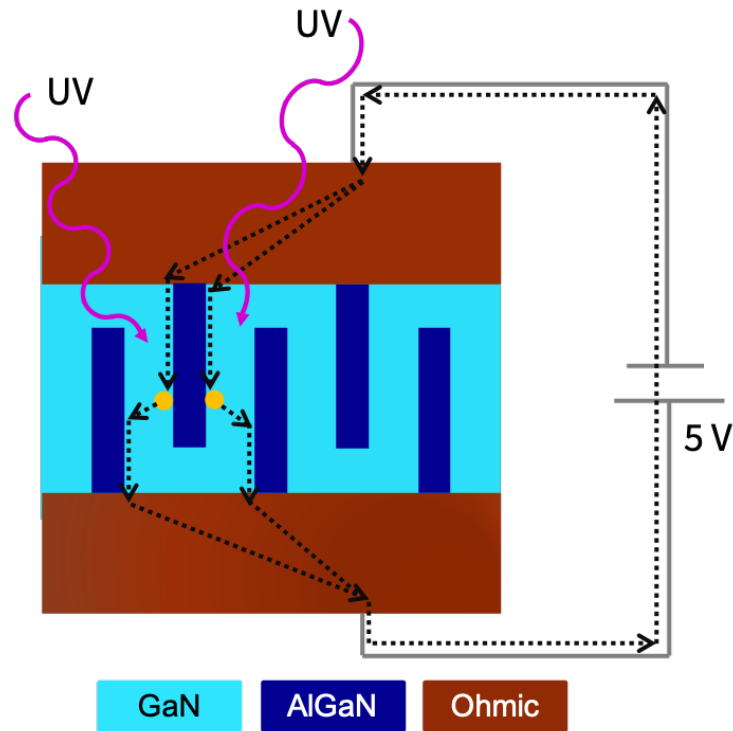


Figure 2.11: Diagram showing operation of interdigitated AlGaIn/GaN photodetector.

2.2.2 Optical Temperature Measurements Using Photodetectors

One use of photodetectors is for combustion monitoring and flame temperature sensing. Optical measurement of flame temperature is typically done using two photodetectors whose spectral responsivities peak at different wavelengths [91]. The ratio of the emission intensities measured by the two photodetectors changes with flame temperature, with the key advantage being that this measurement is not affected by the area of the emitting source. Flame temperature sensors in literature accomplish this dual-spectrum response using a variety of strategies: filtering one half of the photodetector to block certain wavelengths while leaving the other half unfiltered [92, 93], varying the alloy content in photodetectors made with heterostructure materials to change the absorptivity and wavelength of peak responsivity [94], or using two separate photodetectors altogether that have different optical properties [95]. Integrating photodetectors into systems for combustion monitoring or flame temperature sensing may expose them to harsh conditions such as high temperatures, and thus robust photodetectors are desirable.

2.3 High-Temperature Degradation of GaN Sensors

GaN-based devices have shown to be robust in various harsh environments, but may still experience degradation when exposed to high temperatures for long periods of time. Three mechanisms that limit the reliability of GaN Hall-effect sensors at high temperatures are a decline in mobility, permanent change in 2DEG sheet density, and degradation of the Ohmic contacts.

2.3.1 Mobility

Mobility characterizes how quickly a carrier can move through a material in the presence of an electric field. The electron mobility in the 2DEG is limited by scattering, a process by which the carrier's direction or energy is changed due to collisions. There are many different scattering mechanisms, the most important of which are summarized below.

- **Coulomb scattering** includes scattering due to ionized impurities, dopants, or interface charges. Ionized impurity scattering plays a large role in limiting the mobility of heavily doped semiconductors, because the charge of the donors and/or acceptors causes approaching carriers to be deflected. In GaN-based heterostructures, the main contributor to this type of scattering is residual ionized impurities in the GaN layer [96], and it tends to be more important at low temperatures [97].
- **Phonon scattering** includes deformation potential acoustic phonon scattering, piezoelectric acoustic phonon scattering, and polar optical phonon scattering [96, 98]. Phonons are packets of energy associated with the vibration of atoms at any temperature above absolute zero. Acoustic phonons are due to two atoms in a unit cell vibrating in the same direction. Deformation potential acoustic phonons are associated with small changes of the crystal potential due to atomic displacements, while piezoelectric acoustic phonons are related to the polarization of crystals under applied strain [99]. Optical phonons, in contrast, are associated with two atoms in a unit cell vibrating in opposite directions. Acoustic phonons have a lower energy than optical phonons; thus acoustic phonon scattering is more prevalent at room temperature, while optical phonon scattering tends to prevail at higher temperatures [97, 100, 99].
- **Alloy disorder scattering** occurs when electrons from the 2DEG penetrate into the AlGaIn alloy and is highly dependent on 2DEG sheet density [96]. Adding an AlN interlayer between the AlGaIn and the GaN can increase the mobility of the heterostructure by reducing the penetration of electrons into the AlGaIn layer [98].
- **Interface roughness scattering** occurs due to roughness between the AlGaIn and GaN layers. Significant interface roughness can be induced by strain relaxation, thus contributing more to scattering at higher temperatures [98].

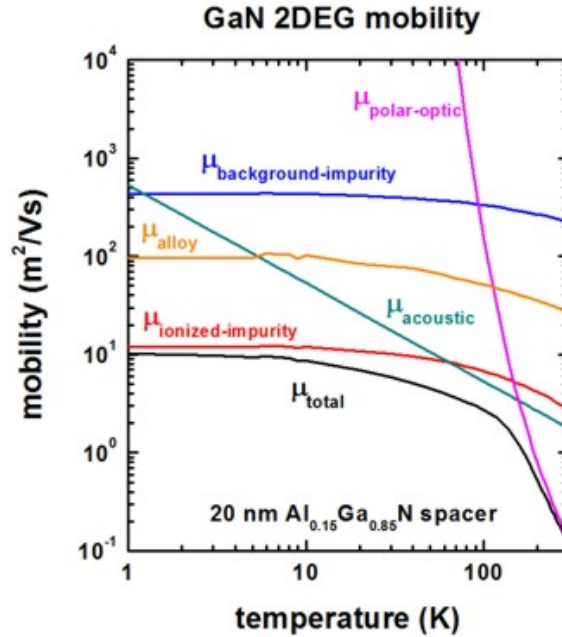


Figure 2.12: Contribution of various scattering mechanisms to total carrier mobility in AlGaN/GaN 2DEG. Reprinted from “S. Birner. Mobility in two-dimensional electron gases (2DEGs). www.nextnano.de/nextnano3/tutorial/1Dtutorial_2DEGmobility.htm.”

The 2DEG sheet density plays a role in mobility due to its effect on different scattering mechanisms. Alloy disorder scattering and interface roughness scattering increase with 2DEG sheet density because the electrons can penetrate deeper into the AlGaN barrier [101]. On the other hand, the electrons in the 2DEG can screen the effects of optical phonon scattering and ionized impurity scattering, so these tend to decrease with increasing 2DEG sheet density [102]. Additionally, while some scattering mechanisms (e.g., residual impurity scattering) are largely unaffected by temperature, others, like optical phonon scattering and interface roughness scattering, have strong temperature dependencies [96, 103, 104]. Thus, the mobility of the 2DEG decreases dramatically with temperature (Fig. 2.12).

AlGaN/GaN has shown to have an electron mobility at room temperature of ~ 1500 to 2500 $\text{cm}^2/\text{V}\cdot\text{s}$, but this diminishes with temperature, eventually decreasing by a factor of 4 to 8 at 300°C [15, 33, 105, 106]. InAlN/GaN has a slightly lower electron mobility at room temperature of ~ 1000 to 1500 $\text{cm}^2/\text{V}\cdot\text{s}$ [107, 108, 109], likely due to greater alloy disorder scattering in InAlN than in AlGaN [110, 111, 112]. Fewer comprehensive studies of its mobility at high temperature have been conducted, but its mobility tends to decrease by a factor of 2 to 4 from room temperature to beyond 300°C [112, 108].

2.3.2 2DEG Sheet Density

The 2DEG in AlGaIn/GaN devices is, in large part, formed by the piezoelectric polarization that arises from the strain induced by lattice mismatch between the AlGaIn and GaN layers. At high temperatures, AlGaIn/GaN devices may experience *strain relaxation*, a process by which tensile strain energy builds up at the interface and causes defects, relieving some of the strain [113]. Strain relaxation leads to a decrease in the piezoelectric polarization, causing a decrease in 2DEG sheet density. It also results in dislocation motion and defects at the interface which negatively affect the mobility, as this upsurge in defects increases the scattering of electrons [114, 115, 116].

Various studies in the literature have investigated the effects of high temperature on mobility and 2DEG sheet density of AlGaIn/GaN devices; however, fewer studies have focused on InAlN/GaN structures. Feng et al. (2004) studied how the mobility and sheet density of devices with and without silicon nitride (SiN) passivation layers changed over the course of a 170-hour exposure to 500°C in a nitrogen atmosphere [116]. They found that the unpassivated devices showed a significant decrease in mobility and 2DEG sheet density due to strain relaxation. A higher degree of strain relaxation was observed in structures with a thicker AlGaIn layer, continuing to increase as the thickness approaches the critical thickness. The passivated structures showed significantly less 2DEG and mobility degradation, leading the authors to conclude that SiN passivation improves the thermal stability of AlGaIn/GaN devices. In a follow-up study, the authors found that the addition of a GaN cap on the top of structure also suppressed some of the strain relaxation through dislocation pinning (requiring more energy to initiate dislocation motion) [115]. This further reduces the scattering, mitigating some of the negative effects on 2DEG sheet density and mobility.

Chen et al. also studied strain relaxation in AlGaIn/GaN heterostructures between room temperature and 526°C. For unpassivated devices, they saw a temperature-dependent strain relaxation beginning at 250°C, which is when the strain energy density has increased enough to change the defect concentration and cause crack formation and extension [114]. The passivated devices, in contrast, showed an increasing 2DEG sheet density as the temperature increased from room temperature to 236°C, as the initial increase in strain enhanced the piezoelectric polarization of the structure. Past a critical temperature, however, the sheet density began to rapidly decrease, once again due to sufficient strain energy to cause dislocation motion, an increasing defect concentration, and crack propagation. For the unpassivated devices, a thinner AlGaIn layer resulted in less strain relaxation. Ultimately, over the whole temperature range, the strain relaxation increased by about 10% and 33% for the unpassivated and passivated samples, resulting in decreases in 2DEG sheet density of about 4% and 16% respectively. An earlier paper from the same group just looked at two unpassivated devices with AlGaIn layer thicknesses of 50 nm and 100 nm [117]. Their finding was that the strain relaxation increased by 12% and 15% over the temperature range (room temperature to 526°C) for the thin and thick samples, with a corresponding reduction of 2DEG sheet density of 5% and 6% respectively.

Finally, in a more recent study by Hou et al. (2017), the authors annealed passivated and unpassivated AlGaIn/GaN devices in argon and in air for 5 hours at 600°C [118]. They found that the passivated devices showed less 2DEG degradation than the unpassivated devices; just within the first hour, the passivated devices were already exhibiting strain relaxation due to high tensile stress exerted by the passivation layer, while the unpassivated devices remained stable. Over the subsequent 4 hours, the unpassivated structures annealed in air showed less strain relaxation than those annealed in argon. This behavior is explained by the fact that oxidation reactions can aid in crack healing [119, 120], and the devices exposed to air had a significantly higher oxygen content than those exposed to argon. Thus, after small cracks developed in both sets of devices induced by strain, the structures exposed to air were more readily healed due to oxidation reactions. Additionally, the surface oxide layer that formed on the samples annealed in air may have helped mitigate the strain relaxation by acting as a dislocation pinning layer, further suppressing crystal glide [118].

Because the 2DEG in InAlIn/GaN devices is formed solely by spontaneous polarization, rather than a combination of that and piezoelectric polarization, strain relaxation should have less of an effect. In one high temperature study of InAlIn/GaN, Xue et al. showed that the 2DEG sheet density decreased only slightly between room temperature and 350°C (from 1.6×10^{13} to $\sim 1.5 \times 10^{13}$).

An observant reader may notice that current-scaled sensitivity of a Hall-effect sensor is inversely proportional to 2DEG sheet density, and thus for this metric a lower sheet density is desirable. However, there are two main reasons that a decrease in 2DEG sheet density via strain relaxation is problematic:

1. Strain relaxation has a permanent effect on 2DEG sheet density and thus current-scaled sensitivity. While the scattering effects at high temperature do substantially decrease mobility, these effects are reversible. Therefore, the device can be calibrated to account for scattering effects at high temperature. Permanent changes to the device through strain relaxation make it difficult to calibrate a device for use in real-world applications.
2. A reduction in 2DEG sheet density leads to an increase in the resistance of the device. Operating a Hall-effect sensor with higher supply current results in a stronger output Hall voltage from sensor, which is generally desirable in sensor measurements. However, a higher resistance device requires more power to achieve the same supply current, given the relationship between power (P), current (I), and resistance (R): $P = I^2 R$. Degradation of the 2DEG results in a need for higher power operation of the device. Additionally, higher operating power contributes to increased self-heating and thermal gradients, which induces a voltage (from the Seebeck effect). As mentioned in section 2.1.1, this Seebeck voltage may be a major contributor to device offset.

2.3.3 Ohmic Contacts

Ohmic contacts are junctions between the semiconductor and metal that have linear current-voltage (I-V) characteristics. High contact resistance can lead to sub-optimal device performance; fabricating devices with low contact resistance is necessary to attain high current density, high sensitivity, and low Joule heating loss, especially at high temperatures [121, 122].

Formation of Ohmic Contacts to GaN

GaN's wide bandgap of 3.4 eV makes it difficult substrate on which to form contacts with low resistance [121]. Currently, Ohmic contacts to GaN tend to be made from a stack of metals in the following order from bottom to top: titanium (Ti); aluminum (Al); a blocking metals such as Ti, molybdenum (Mo), nickel (Ni), tantalum (Ta), or platinum (Pt); gold (Au). The metal stack generally undergoes a high temperature rapid thermal anneal (RTA). This results in the Ti extracting N from the GaN, which leaves behind N vacancies and allows for the formation of TiN, an alloy with a low work function [123, 124, 125]. The contact stack before and after thermal annealing is depicted in Fig. 2.13, while the atomic concentration of the various components is shown in Fig. 2.14 [126]. The high density of N vacancies creates donor states near the interface, essentially resulting in highly doped n-GaN [122]. If the n-GaN is heavily doped enough, there will be significant band bending at the metal/semiconductor (M/S) interface, creating a very thin region through which electrons can tunnel unhindered [127]. Another consequence of the heavy doping is a lowering of the conduction band, thus reducing the effective M/S barrier height and allowing for increased thermionic emission, further lowering the contact resistance. Ti is also often chosen for the bottom layer because it provides good adhesion to GaN [125]. Like the Ti layer, the Al layer serves to extract N from the GaN to form alloys. Al is also able to form an intermetallic compound with Ti, which keeps the Ti from diffusing down into the contact surface [127].

The blocking metal/Au sequence on top of the Ti/Al may further increase the outdiffusion of N to enhance the n-GaN doping, but more importantly, the Au prevents oxidation of the Al and Ti. The blocking metal between the Al and Au is needed to reduce both the diffusion of Au down into the contact stack and the out-diffusion of Al and Ti [123, 128, 129]. The choice of the blocking metal can have a large effect on the surface morphology and resistance of the Ohmic contact [122, 130].

Oxidation

One mechanism through which contacts may degrade at high temperatures is oxidation of Al, which leads to increase in contact resistance [131, 124]. The Au top layer and the metallic blocking layer serve to reduce this effect; Lee et al. (2000) found that Pt was effective in preventing significant oxidation [129]. Images of Ti/Al/Mo/Au contacts before and after thermal storage at 850°C for 5 hours are shown in Fig. 2.15, where the discoloration after the thermal storage is due to oxidation

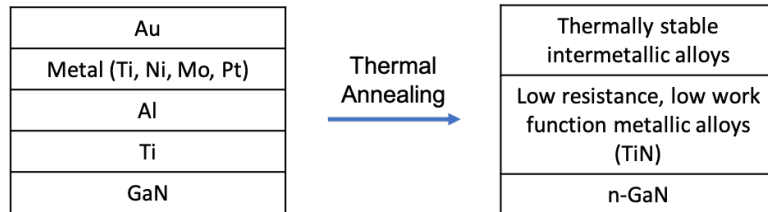


Figure 2.13: Diagram of Ohmic contact layers on GaN before and after rapid thermal anneal.

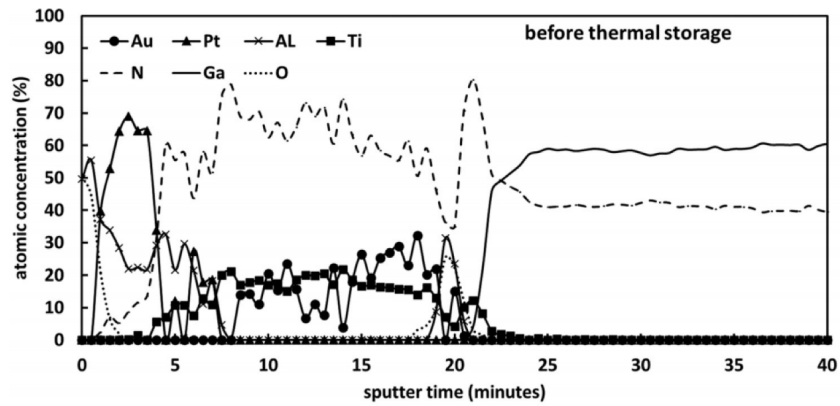


Figure 2.14: Auger electron spectroscopy (AES) atomic concentration depth profiles of rapid thermally annealed Ti/Al/Pt/Au Ohmic contacts. Reprinted from “M. Hou and D. G. Senesky. Operation of ohmic Ti/Al/Pt/Au multilayer contacts to GaN at 600°C in air. *Applied Physics Letters*, 105(8):081905, 2014.” with the permission of AIP Publishing.

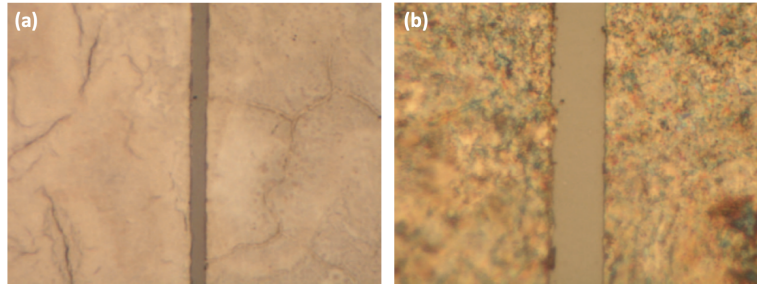


Figure 2.15: Images of Ti/Al/Mo/Au contacts (a) before and (b) after thermal storage at 850°C for 5 hours. Adapted with permission from Springer Nature Customer Service Centre GmbH: D. Selvanathan, L. Zhou, V. Kumar, I. Adesida, and N. Finnegan. Long-term thermal stability of Ti/Al/Mo/Au ohmic contacts on n-GaN. *J. of Elec. Mater.*, 32:335–340, ©2003.

of the contact surface.

Metal Diffusion

Another prominent degradation mode of Ohmic contacts is interdiffusion of the various metals in the contact stack. In a 2003 study on the long-term thermal stability of Ti/Al/Mo/Au contacts at high temperature, Selvanathan et al. found that the Au and Mo diffused down to the GaN interface over the course of the high temperature exposure [132]. Metals with high work functions diffusing down to the surface of the GaN hinders the flow of electrons through the contact, thus increasing the contact resistance. The downward diffusion of Au and subsequent formation of Au-rich intermetallic compounds can lead to voids at the surface of the contact as well as large grains that may crack the passivation layer [133]. In addition to in-diffusion of metals, the out-diffusion of Ga into the metal stacks was also seen by Piazza et al. at high temperatures [133]. Finally, the intermixing of Al and Au (purple plague) also leads to a bumpy surface morphology and higher contact resistance [130, 122]. Fig. 2.16 shows the results of metal interdiffusion in Ti/Al/Ni/Au contacts after thermal exposure at 340°C for 2000 hours; some areas are Ga-rich and some are Au-rich, and voids can be seen in the Au-depleted zones.

Electromigration

Unlike oxidation and metal diffusion, which may happen at high temperature regardless of whether or not the device is biased with current or voltage, electromigration only occurs when a device is being operated. Electromigration is due to the momentum of moving electrons being transferred to metal ions, knocking the ions out of their original lattice positions. Operating a device with higher current density increases the number of electrons available to collide with the ions, thus increasing the rate and magnitude of electromigration. Electromigration results in directional diffusion, causing the formation of voids and hillocks. Electromigration is exacerbated at high temperatures because

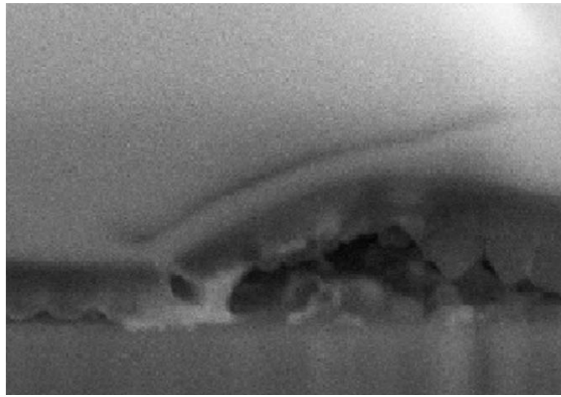


Figure 2.16: Images of Ti/Al/Ni/Au contacts after thermal exposure at 340°C for 2000 hours. The gray areas are Ga-rich and the white areas Au-rich. Reprinted from “M. Piazza, C. Dua, M. Oualli, E. Morvan, D. Carisetti, and F. Wyczisk. Degradation of TiAlNiAu as ohmic contact metal for GaN HEMTs. *Microelectronics Reliability*, 49(9):1222–1225, ©2009.” with permission from Elsevier.

(1) there is increased electron scattering and (2) there is an increased rate of diffusion [134]. Kuzmík et al. (2004) saw the appearance of dark spots on the negatively biased Ti/Al/Ni/Au contact on an AlGaIn/GaN HEMT, which they attributed to electromigration [135]. Similarly, Dietrich et al. (2003) report on electromigration of the metallization, especially gold, in AlGaIn/GaN RF-HEMTs, which increased the source resistance by 40% [136]. Finally, the performance of two different InAlN/GaN HEMTs with Al/Ti/Ni/Au contacts was studied at temperatures beyond 500°C by Maier et al. (2009). One of the devices failed during the 700°C exposure, while the other failed near the beginning of the 800°C exposure. Significant redistribution of Au and Ni were observed, likely resulting from electromigration [137].

Chapter 3

Hall-Effect Sensor Geometry Optimization

Octagonal Hall-effect sensors were designed in order to optimize sensitivity and signal-to-noise ratio (SNR) with respect to thermal noise. Much of this chapter was previously published in [64] (© 2019 IEEE). Devices were designed to optimize the sensitivity scaled by supply current (S_i); sensitivity scaled by supply voltage (S_v); SNR scaled by supply current (SNR/I); and SNR scaled by supply voltage (SNR/V). The general process for this optimization is outlined below:

1. Write each parameter (S_i , S_v , SNR/I, SNR/V) in terms of G_H and $(L/W)_{eff}$.
2. Write each parameter in terms of only $(L/W)_{eff}$ by substituting Eq. 2.2 in for G_H .
3. Take derivatives to get optimal $(L/W)_{eff}$.
4. Plug optimal $(L/W)_{eff}$ into G_H equation (Eq. 2.2).
5. From each optimal G_H , calculate optimal λ using the following equation ([55, 138]:

$$G_H \approx 1 - 1.940 \times \left(\frac{\lambda}{1 + 0.414\lambda} \right)^2 \quad (3.1)$$

where λ is defined as the length of the sides with contacts (b) divided by the sum of the sides with contacts and those without ($a + b$, where a is the length of the sides without contacts).

6. Determine how long contacts need to be by solving for a and b .

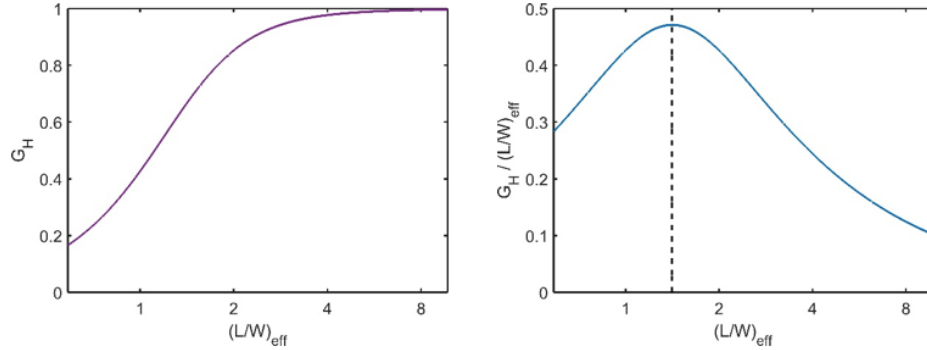


Figure 3.1: $(L/W)_{eff}$ values that maximize Hall-effect sensitivities with respect to supply current (left) and supply voltage (right) in Equations 2.4 and 2.5. © 2019 IEEE.

3.1 Optimization for Sensitivity Performance

Devices were designed according to the above process to have contact lengths that maximized the current-scaled and voltage-scaled sensitivities (S_i and S_v). The optimal $(L/W)_{eff}$ values were calculated by maximizing Eq. 2.4 and Eq. 2.5 respectively, which showed that S_i is proportional to G_H and S_v is proportional to $G_H/(L/W)_{eff}$. A visual depiction of the optimization is presented in Fig. 3.1. These optimal $(L/W)_{eff}$ values (∞ for maximum S_i and 1.41 for maximum S_v) were fed back into Eq. 2.2 to compute the corresponding G_H values. Then, from Eq. 3.1, the optimal λ values of 0 and 0.5 were calculated, resulting in a device with infinitely small contacts for S_i and a device in which the length of the sides with contacts were equal to the length of the sides without contacts for S_v .

3.2 Optimization for Noise Performance

3.2.1 Types of Noise

There are several sources of noise in Hall-effect sensors. Thermal noise, also known as Johnson noise or white noise, is due to thermal agitation of charge carriers and is present in all electronic components and circuits. The equation for thermal noise is

$$V_n = \sqrt{4k_B T R \Delta f}, \quad (3.2)$$

where k_B is the Boltzmann constant, T is the temperature, Δf is the operation bandwidth, and R is the device resistance across transverse contacts, which is also defined as the sheet resistance (R_{sh}) multiplied by $(L/W)_{eff}$. Thermal noise tends to be the dominant form of noise at high frequency.

Flicker noise, also known as 1/f noise, dominates at low frequency, but there is currently no

universally-accepted theory that explains 1/f noise. The number fluctuation theory attributes flicker noise to the trapping and de-trapping of carriers, changing the carrier density in the conducting layer. Meanwhile, the mobility fluctuation theory attributes the noise to the fluctuation of bulk mobility due to phonon scattering [139].

There are additional sources of noise that may be neglected because they have a less noticeable effect than thermal noise and flicker noise. For example, generation-recombination noise, similar to the number fluctuation theory, is caused by carriers in the semiconductor being trapped, and changing the number of carriers and thus the resistance of the conducting layer [140, 141]. Another example is shot noise, which arises due to the discrete nature of electronic particles [140].

Two quantities that can characterize the noise in a semiconductor device are the corner frequency (f_c) and the Hooge parameter (α_H). The corner frequency is the frequency at which the thermal noise begins to dominate over the 1/f noise. The Hooge parameter relates the power spectral density of the noise to the physical quantities of the device in operation, such as total number of carriers and supply voltage. While the Hooge parameter itself has no true physical meaning, it is often used to compare the noise intensity between different materials or devices [142, 143].

3.2.2 Optimization for SNR with Respect to Thermal Noise

Although at low-frequency operation thermal noise is smaller than the offset voltage, it becomes the dominant form of noise as the operating frequency increases. Considering only thermal noise, the SNR can be written as the ratio between the voltage produced by the Hall-effect and the voltage generated by thermal noise: V_H/V_n . It can be shown that given material parameters and operating conditions, both SNR/I and SNR/V are a function only of the geometry of the device, as they are both directly proportional to G_H and have a dependence on $(L/W)_{eff}^{-1/2}$ and $(L/W)_{eff}^{-3/2}$ respectively;

$$\frac{SNR}{I} = \frac{V_H}{V_n I} = \frac{S_i B}{V_n} = \frac{r_n G_H}{q n_s} \frac{B}{\sqrt{4k_B T R \Delta f}} = \frac{r_n G_H}{q n_s} \frac{B}{\sqrt{4k_B T R_{sh} (\frac{L}{W})_{eff} \Delta f}} \propto \frac{G_H}{(\frac{L}{W})_{eff}^{1/2}} \quad (3.3)$$

$$\frac{SNR}{V} = \frac{V_H}{V_n V} = \frac{S_v B}{V_n} = \frac{r_n G_H \mu_H}{(\frac{L}{W})_{eff}} \frac{B}{\sqrt{4k_B T R_{sh} (\frac{L}{W})_{eff} \Delta f}} = \frac{r_n G_H \mu_H}{(\frac{L}{W})_{eff}^{3/2}} \frac{B}{\sqrt{4k_B T R_{sh} \Delta f}} \propto \frac{G_H}{(\frac{L}{W})_{eff}^{3/2}} \quad (3.4)$$

Optimal $(L/W)_{eff}$ values were calculated by maximizing these equations, as shown in Fig. 3.2. Following the same process outline previously, the $(L/W)_{eff}$ values (2 for maximum SNR/I and 1 for maximum SNR/V) were fed back into Eq. 2.3 to compute the G_H values, and then from Eq. 3.1 the corresponding λ values (0.3 for SNR/I and 0.7 for SNR/V) could be calculated. These resulted in devices in which the length of the sides without contacts were 2.33 times greater than those with contacts for SNR/I and the opposite for SNR/V.

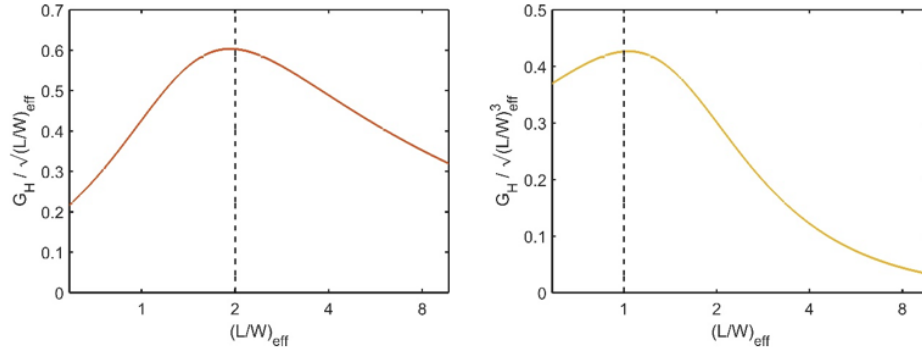


Figure 3.2: $(L/W)_{eff}$ values that maximize SNRs with respect to supply current (left) and supply voltage (right) in Equations 3.3 and 3.4

3.3 Final Device Geometries

The shapes of the fabricated Hall-effect plates are shown in Fig. 3.3 and the geometrical parameters of the four devices fabricated are summarized in Table 3.1. Because true point-like contacts are impossible to realize, the fabricated “point-like” device had a λ of 0.150, which resulted in a G_H of 0.981 and a $(L/W)_{eff}$ of 3.26, corresponding to $a = 5.66b$. The predicted percentage of the sensitivity and SNR relative to the optimized shape is listed in Table 3.2, where the values for the point-like device are based on the dimensions of the fabricated device. For S_i , this percentage is equivalent to the G_H ratio between the given Hall plate and that with point-like contacts, as per Eq. 2.4. Accordingly, for SNR/I, this percentage was calculated as the ratio of $G_H/(L/W)_{eff}^{1/2}$ between the Hall plate and that with short contacts, as per Eq. 3.3. For S_v , this percentage was calculated as the ratio of $G_H/(L/W)_{eff}$ between the Hall plate and that with equal sides, while for SNR/V it is the ratio of $G_H/(L/W)_{eff}^{3/2}$ between the Hall plate and that with long contacts, as per Eq. 2.5 and Eq. 3.4 respectively.

3.4 Device Microfabrication

Two sets of devices were fabricated: one on an AlGaIn/GaN-on-Si wafer grown by metal-organic chemical vapor deposition (MOCVD) in an Aixtron close-coupled showerhead (CCS) reactor in the Stanford Nanofabrication Facility (SNF), and the second on an InAlN/GaN-on-Si wafer purchased from NTT Advanced Technology Corporation. The AlGaIn/GaN stack consists of a 1.5 μm buffer structure, a 1.2 μm GaN layer, a 1 nm AlN spacer, a 30 nm $\text{Al}_{0.25}\text{Ga}_{0.75}\text{N}$ barrier layer, and a 2 nm GaN cap. The InAlN stack consists of a 300 nm buffer structure, a 1 μm GaN layer, a 0.8 nm AlN spacer, and a 10 nm $\text{In}_{0.17}\text{Al}_{0.83}\text{N}$ barrier layer. For the AlGaIn/GaN and InAlN/GaN stacks respectively, the sheet resistances at room temperature were 361 Ω/\square and 248 Ω/\square , the carrier

Device Parameter	S_i	SNR/I	S_v	SNR/V
Maximize	G_H	$\frac{G_H}{(\frac{L}{W})_{eff}^{1/2}}$	$\frac{G_H}{(\frac{L}{W})_{eff}}$	$\frac{G_H}{(\frac{L}{W})_{eff}^{3/2}}$
$(\frac{L}{W})_{eff}$	∞	2	$\sqrt{2}$	1
G_H	1	0.861	0.667	0.430
λ	0	0.3	0.5	0.7
Side Lengths (b = contact length)	$b = 0$	$2.33b = a$	$a = b$	$b = 2.33a$
Name	Point-like	Short Contacts	Equal Sides	Long Contacts

Table 3.1: Parameters used in optimization of Hall-effect device contact lengths.

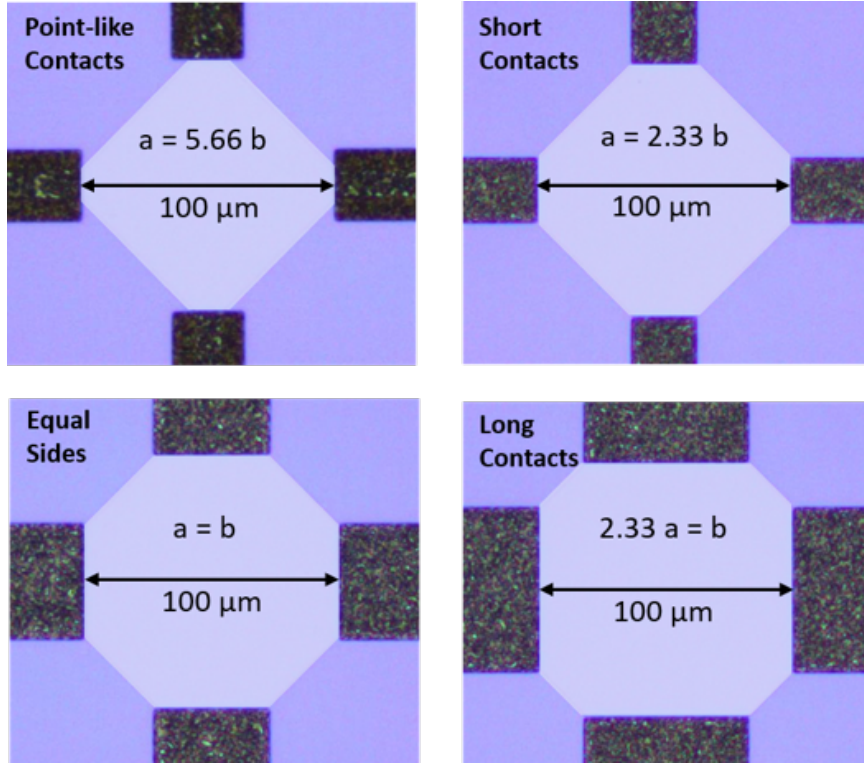


Figure 3.3: Images of 100- μm -diameter Hall plates with various geometries, where b is the length of the contacts and a is the length of the sides without the contacts. The device with point-like contacts is optimized for S_i , the device with short contacts is optimized for SNR/I, the device with equal sides is optimized for S_v , and the device with long contacts is optimized for SNR/V. © 2019 IEEE.

Geometry	S_i	SNR/I	S_v	SNR/V
Point-like	100%	80.2%	51.7%	28.3%
Short Contacts	88.1%	100%	91.3%	70.7%
Equal Sides	68.2%	92.1%	100%	92.1%
Long Contacts	44.0%	70.7%	91.3%	100%

Table 3.2: Relative design parameters of varied Hall plate geometry.

mobilities were $1811 \text{ cm}^2/\text{V}\cdot\text{s}$ and $1143 \text{ cm}^2/\text{V}\cdot\text{s}$, and the sheet electron densities were $9.2 \times 10^{12} \text{ cm}^{-2}$ and $2.1 \times 10^{13} \text{ cm}^{-2}$, measured with Van der Pauw and Hall-effect measurements. The subsequent fabrication process was followed for both sets of devices: a mesa etch was performed on the III-nitride layer, a Ti (20 nm)/Al (200 nm)/Mo (40 nm)/Au (80 nm) metal stack was deposited and annealed for 35 seconds at 850°C to form Ohmic contacts, a 7-nm-thick Al_2O_3 passivation layer was atomic layer deposited (ALD) to prevent oxidation, vias were etched to allow for electrical connection to the contacts, and bond metal. The fabrication process is depicted in Fig. 3.4 and a cross-sectional schematic of the material stack is shown in Fig. 3.5.

3.5 Experimental Testing

The devices were tested in a tunable 3D Helmholtz coil, detailed in [144]. A sourcemeter (Kiethley 2400) generated a current between two contacts across the Hall-effect plate, and a multimeter (Agilent 34410A) measured the Hall voltage generated across the other two contacts. A switching matrix (U2715A) was used to alternate between the eight phases to implement current spinning [144]. During testing, the devices were placed in MuMetal® shielding cannisters to block extraneous magnetic fields; the magnetic field inside the cannisters was below $6 \mu\text{T}$. A diagram of the test setup is shown in Fig. 3.6.

The devices were tested with supply current ranging from $60 \mu\text{A}$ to 1.2 mA , and for sensitivity testing the applied magnetic field was $\pm 2 \text{ mT}$. This applied magnetic field is well within the range for which the Hall voltage of the device is linear with respect to magnetic field. Fig. 3.7 shows the output voltage Hall voltage with respect to magnetic fields ranging from -4 mT to 4 mT , with a supply current of $300 \mu\text{A}$, for two of the devices studied in this chapter; it should be noted that all the Hall-effect sensors discussed here show similar linear characteristics. The offset voltages were measured over the same range of supply current ($60 \mu\text{A}$ to 1.2 mA) with no external applied magnetic field; 300 measurements were taken at each current value.

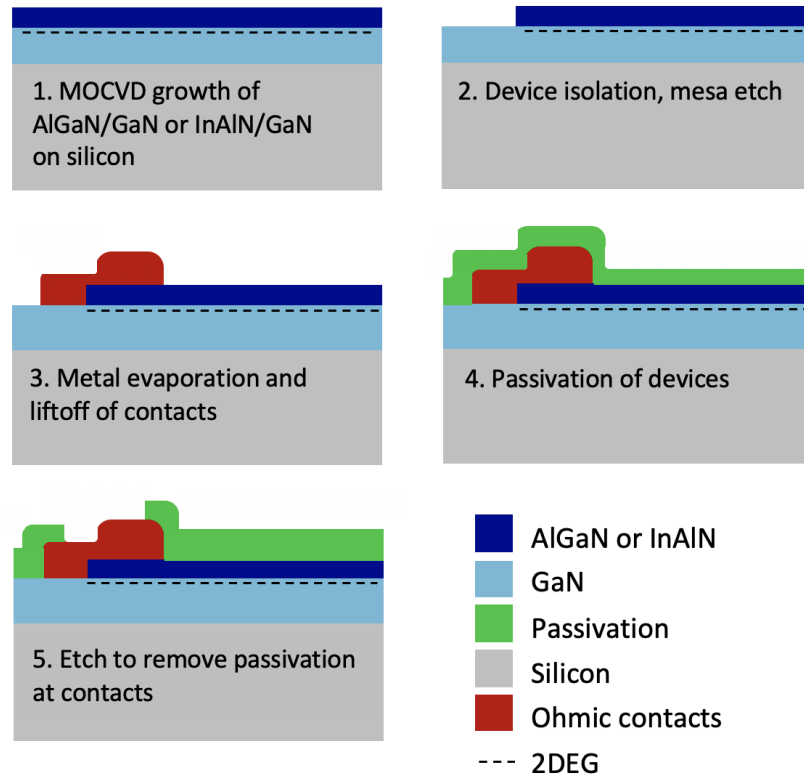


Figure 3.4: Fabrication process of AlGaIn/GaN and InAlN/GaN Hall-effect sensors.

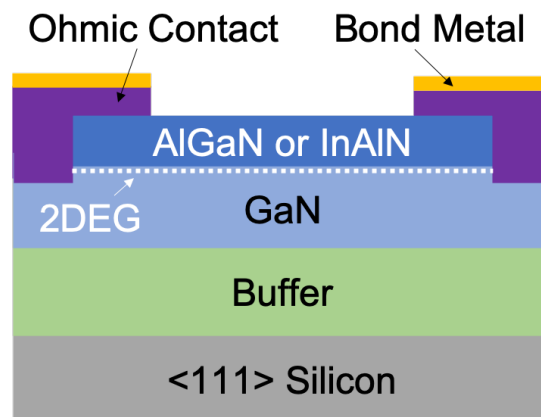


Figure 3.5: Cross-sectional schematic of the material stack of the AlGaIn/GaN and InAlN/GaN Hall-effect sensors fabricated at the Stanford Nanofabrication Facility. Reprinted from [73] with the permission of AIP Publishing.

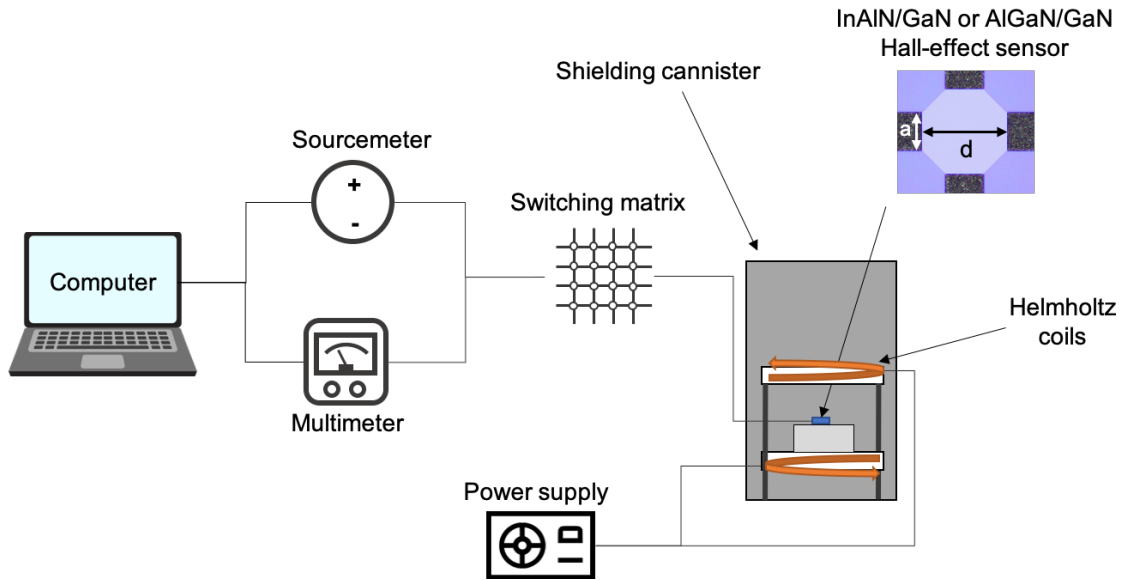


Figure 3.6: Diagram of test setup used to measure sensitivity and offset of Hall-effect sensors in ambient environment.

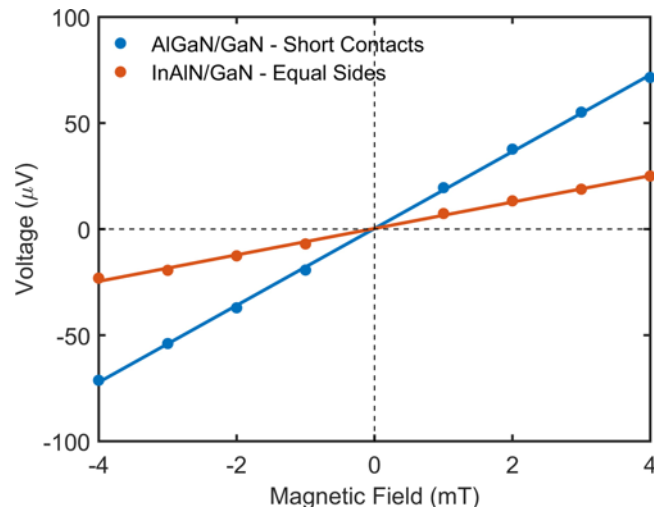


Figure 3.7: Output Hall voltage (after current spinning) versus magnetic field for one of the Al-GaN/GaN devices and one of the InAlN/GaN devices with a supply voltage of $300 \mu\text{A}$, showing linearity of the response in the range of -4 mT to 4 mT . All devices used in this study showed similar linear behavior. © 2019 IEEE.

3.6 Sensitivity Results

For both material platforms, the devices with the point-like contacts had the highest current-related sensitivity and the devices with equal sides had the highest voltage-related sensitivity. The measured S_i and S_v closely follow the predicted trends in Table 3.2. The device sensitivities for both samples are shown in Fig. 3.8 and they are listed in Table 3.3 along with the percentage of the maximum value, for comparison. The AlGaIn/GaN devices consistently have higher current- and voltage-related sensitivities than the InAlIn/GaN devices. Since the AlGaIn/GaN device has lower sheet concentration and higher mobility than the InAlIn/GaN device, these trends hold with Eq. 2.4 and Eq. 2.5 respectively. The InAlIn/GaN Hall plate voltage-related sensitivities are an average of 64.7% of the values for the AlGaIn/GaN Hall plates, which closely corresponds to the ratio between the mobilities of the materials (63.1%). Similarly, the InAlIn/GaN current-related sensitivities are an average of 46.3% of the AlGaIn/GaN values, which corresponds to the ratio between their sheet electron densities (43.7%).

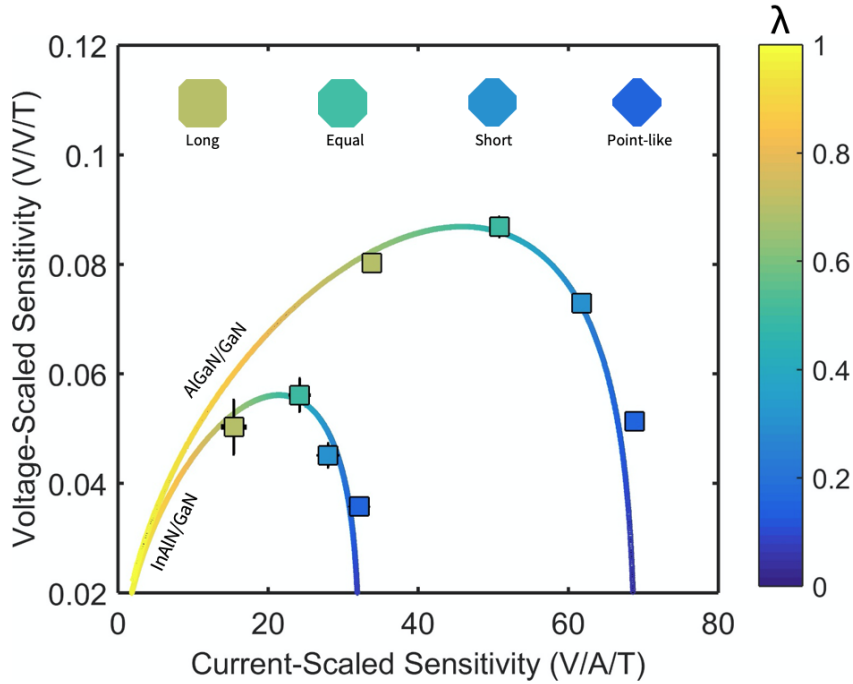


Figure 3.8: Voltage-scaled and current-scaled magnetic sensitivity for various octagonal AlGaIn/GaN and InAlIn/GaN Hall plates. Both sets of devices follow the predicted trend: the devices with equal sides have the highest S_v and the devices with point-like contacts have the highest S_i . The colored line shows the theoretical values based on sweeping λ between 0 and 1 and calculating G_H and $(L/W)_{eff}$; S_i varies directly with G_H , while S_v varies with $G_H/(L/W)_{eff}$. The error bars depict the standard deviation of the sensitivity values over multiple supply currents from 60 μA to 1.2 mA. © 2019 IEEE.

	S_i ($\text{VA}^{-1}\text{T}^{-1}$)		S_v ($\text{VV}^{-1}\text{T}^{-1}$)	
	Value	% Max	Value	% Max
<i>AlGaIn/GaN</i>				
Point-like	68.85	100%	51.36	59.1%
Short Contacts	61.77	89.7%	72.92	84.0%
Equal Sides	50.82	73.8%	86.85	100%
Long Contacts	33.82	49.1%	80.23	92.4%
<i>InAlN/GaN</i>				
Point-like	32.18	100%	35.77	63.7%
Short Contacts	28.00	87.0%	45.15	80.4%
Equal Sides	24.20	75.2%	56.13	100%
Long Contacts	15.45	48.0%	50.31	89.6%

Table 3.3: Sensitivity results. © 2019 IEEE.

3.7 Offset Results

At low bias currents ($<300 \mu\text{A}$), the offset voltages of all the AlGaIn/GaN and InAlN/GaN devices were consistently in the nanovolt range, corresponding to a magnetic field offset below $20 \mu\text{T}$, detailed in Table 3.4 and Table 3.5. For both material platforms the point-like devices showed higher offset voltages than the other geometries; however, their higher internal resistances lead to larger bias voltages for the same supply current, resulting in magnetic field offsets that are similar in magnitude to that of the other devices. At high biases (up to 1.2 mA), the magnetic field offsets for some of the devices remained constant below $20 \mu\text{T}$, while some showed larger increases, up to $80 \mu\text{T}$. The magnetic field offsets of the AlGaIn/GaN and InAlN/GaN devices with equal sides are shown in Fig. 3.9, and similar trends were seen for the other geometries. There is no strong correlation between Hall-effect plate geometry and offset; the variation may be due to minor flaws during fabrication or slight differences in packaging.

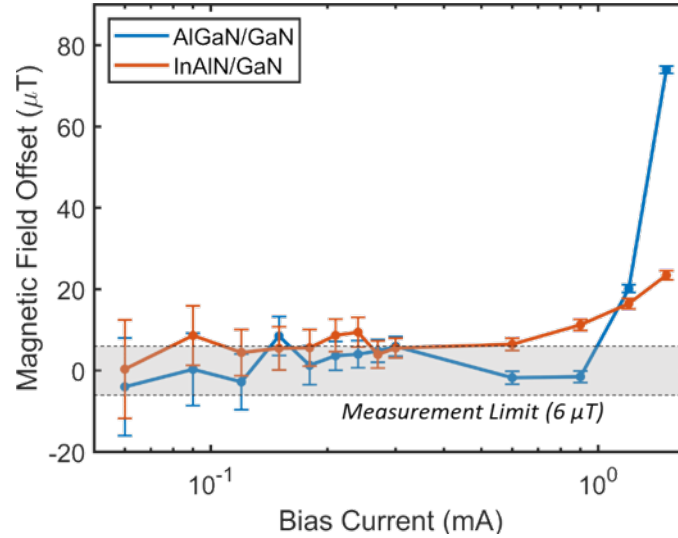
3.8 Noise Results

The variation in signal-to-noise behavior between the Hall-effect plates with differing geometry was investigated by Dowling (2019) [62]. The corner frequency and Hooge parameter were measured for each of the four InAlN/GaN devices. An examination of the corner frequencies showed that for any given supply voltage, the devices with shorter contacts had a lower f_c . This means that the $1/f$ noise

Geometry	Offset Voltage (nV)	Magnetic Field Offset (μT)
Point-like	66.8	6.84
Short Contacts	45.4	4.72
Equal Sides	37.3	4.17
Long Contacts	37.1	11.0

Table 3.4: Mean offsets of AlGaIn/GaN Hall plates at low bias ($<300 \mu\text{A}$). © 2019 IEEE.

Geometry	Offset Voltage (nV)	Magnetic Field Offset (μT)
Point-like	70.7	14.6
Short Contacts	73.8	2.98
Equal Sides	25.4	1.03
Long Contacts	13.4	7.56

Table 3.5: Mean offsets of InAlIn/GaN Hall plates at low bias ($<300 \mu\text{A}$). © 2019 IEEE.Figure 3.9: Measured magnetic field offsets of the AlGaIn/GaN and InAlIn/GaN devices with equal sides. Offsets tend to be $<20 \mu\text{T}$ at low bias currents ($<300 \mu\text{A}$) and greater at higher bias currents (up to 1.2 mA). © 2019 IEEE.

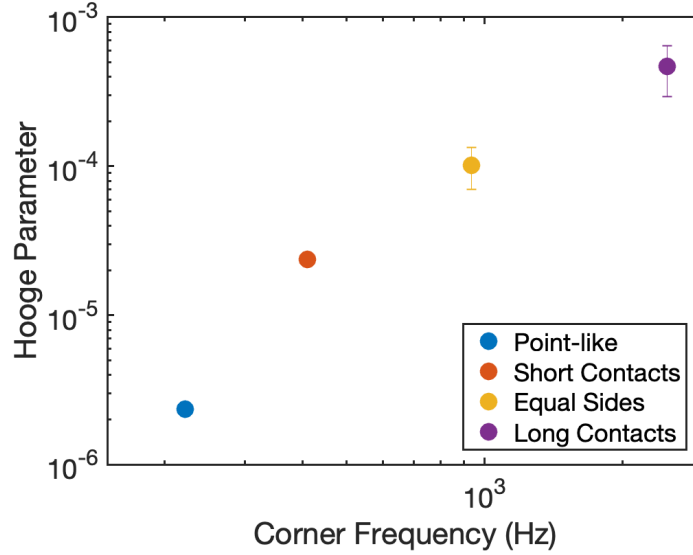


Figure 3.10: Mean Hooge parameter for each geometry vs. corner frequency measured at ~ 0.5 V.

in devices with short contacts will fall below the thermal noise floor at a lower frequency than for the devices with longer contacts. Devices with shorter contacts also proved to have a lower Hooge parameter. Possible explanations for this trend include: 1) devices with longer contacts have larger active areas and thus are influenced by a greater number of carriers, and 2) devices with longer contacts have lower resistances and thus a higher power density for a given supply voltage, which may relate to carrier vibrational energy [62]. However, the Hooge parameters measured for the $50\text{-}\mu\text{m}$, $100\text{-}\mu\text{m}$, and $200\text{-}\mu\text{m}$ devices with a given geometry did not vary significantly, whereas this parameter did vary significantly between geometries [62]. Fig. 3.10 plots the mean Hooge parameter for each geometry against the corner frequency measured at ~ 0.5 V.

The signal-to-noise ratio (SNR) with respect to thermal noise was not measured directly, but can be calculated to determine the theoretical noise floor of each device (shown along with Hooge parameter and cutoff frequency in table 3.7). The parameters SNR/V and SNR/I can be calculated as follows:

$$\frac{\text{SNR}}{V} = \frac{V_H}{V_n V} \quad (3.5)$$

$$\frac{\text{SNR}}{I} = \frac{V_H}{V_n I}. \quad (3.6)$$

For the same four devices, SNR/V and SNR/I were calculated using Hall voltage measurements taken with applied current between $60\ \mu\text{A}$ and $1.2\ \text{mA}$. Table 3.6 compares the measurements with the expected relative magnitudes of these SNR parameters. For all of the devices except that with short contacts, the SNR/V matched expected values quite well (within 1%). For the SNR/I , the

	SNR/V ($\text{Hz}^{1/2}\text{V}^{-1}$)			SNR/I ($\text{Hz}^{1/2}\text{V}^{-1}$)		
	Value	% Max	Expected	Value	% Max	Expected
Point-like	1.77×10^4	38.0%	38.7%	1.59×10^4	92.4%	89.2%
Short Contacts	2.77×10^4	59.6%	70.6%	1.72×10^7	100%	100%
Equal Sides	4.24×10^4	91.3%	92.0%	1.83×10^7	106.4%	92.1%
Long Contacts	4.64×10^4	100%	100%	1.43×10^7	83.0%	70.8%

Table 3.6: Thermal noise results.

Geometry	Thermal Noise ($\text{nV}/\sqrt{\text{Hz}}$)	Hooge Parameter	Cutoff Frequency (Hz)
Point-like	3.86	2.35×10^{-6}	222.29
Short Contacts	3.20	2.37×10^{-5}	409.63
Equal Sides	2.67	1.02×10^{-4}	937.50
Long Contacts	2.25	4.69×10^{-4}	2502.42

Table 3.7: Parameters related to noise for devices of different geometries. The thermal noise is calculated for $100\text{-}\mu\text{m}$ devices and the cutoff frequency is measured at $\sim 0.5\text{ V}$.

values were less consistent with the expected values. To calculate the expected percentages, all of the values were scaled against the expected highest value, which in this case was the device with short contacts. The values of SNR/V suggested that there may have been an issue with the device with short contacts; thus scaling all of the SNR/I values against this device is likely the reason that the measurements do not match the expected percentages.

The trends in Hooge parameter and corner frequency do not match up with the optimization done with respect to thermal noise. This discrepancy leads to the following conclusions:

- At low frequency operation, devices with longer contacts have more noise.
- Because devices with longer contacts have a larger magnitude of $1/f$ noise, the corner frequency is also higher, as the $1/f$ noise will not fall below the thermal noise floor until a higher frequency is reached.
- If the sensors can be operated at a sufficiently high frequency (e.g., fast current spinning and readout circuitry), then the thermal noise will be the dominant form of noise, and the optimized Hall plates will have the least noise.

3.9 Conclusions

In this chapter, we present the first comprehensive study of how the shape factor affects the sensitivity, offset, and noise of Hall-effect sensors, the results of which are summarized in Fig. 3.11. The experimental results show that the sensitivity and low frequency (thermal) noise characteristics of both the AlGa_N/Ga_N and InAl_N/Ga_N sensors follow the trends originally theorized for silicon Hall plates, confirming the validity of the shape factors over multiple material platforms. An investigation into the low frequency noise characteristics of the Hall-effect sensors shows that devices with shorter contacts have a lower corner frequency and Hooge parameter. However, at frequencies in the kHz range, the flicker noise drops below the thermal noise floor, and then the shape factor theory becomes valid. The consistent low offset of the various devices suggests that this parameter is not of utmost importance in selecting the geometry of a Hall-effect sensor; rather, the operating conditions (e.g., voltage vs. current bias, low frequency vs. high frequency) should be carefully considered for optimal sensor design.

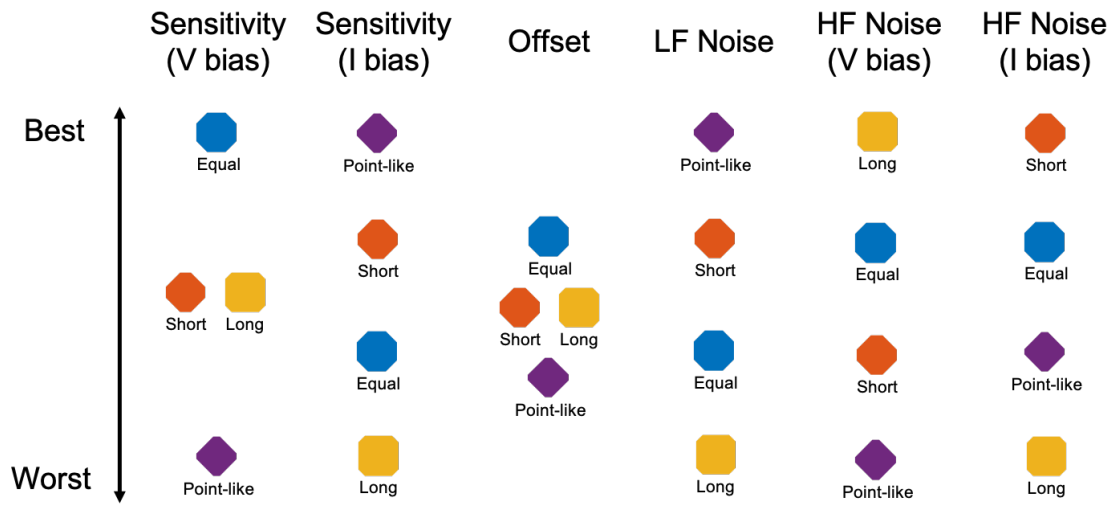


Figure 3.11: Summary of effect of geometry of Hall-effect sensor on various performance parameters.

Chapter 4

Extreme Environment Characterization of Hall-Effect Sensors

The previous chapter discussed the comprehensive characterization of sensitivity, offset, and noise of Hall-effect sensors in an ambient environment. This chapter will explore how the sensors behave when subjected to harsh conditions, with the main focus on high temperature environments. Much of this chapter was previously published in [73] with the permission of AIP Publishing.

4.1 High Temperature Testing

4.1.1 Experimental Setup for Sensitivity Tests

To conduct the high temperature sensitivity tests, the devices were diced into square dies with side lengths of ~ 2 mm and epoxied with Durabond 952 Epoxy to a 1 in. \times 1 in. aluminum sheet with a thickness of 1 mm, which was subsequently placed on a heating stage manufactured by Linkam Scientific Instruments. The contacts were wirebonded directly to the electrical connections of the chamber, which were then connected to a sourcemeter (Keithley 2400) to generate a voltage between two contacts, and a multimeter (Agilent 34410A) to measure the Hall voltage generated across the two transverse contacts. A switching matrix (U2715A) was used to implement current spinning, by alternating the source and sense contacts between the eight configurations described in section 2.1.1. The heating stage was placed between two copper coils wound around a 3D-printed scaffold, and current was applied through the coils to generate a magnetic field of 2 mT. A diagram of the test setup is shown in Figure 4.1.

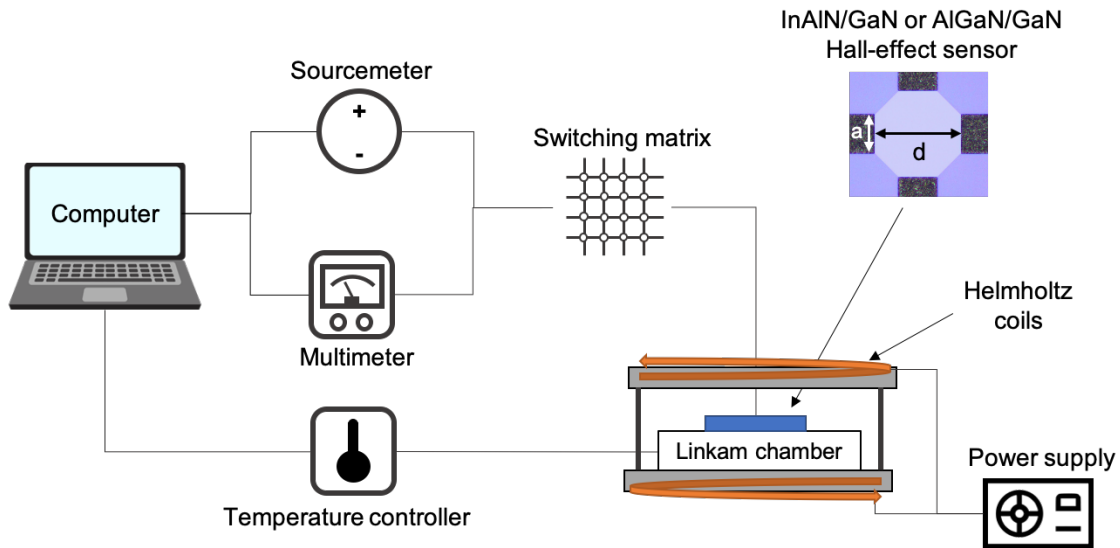


Figure 4.1: Diagram of the experimental setup. During testing, the Hall-effect sensor was epoxied to an aluminum sheet placed atop the heating stage, and the device was wire bonded directly to pins connecting to electrical feedthroughs. Reprinted from [73], with the permission of AIP Publishing.

For the initial sensitivity sweep, the device was supplied with three different bias voltages (0.3 V, 0.5 V, and 1 V), and ten measurements were taken under each bias condition. The sensor was biased with voltage rather than current because the resistance across the device increases dramatically as the temperature increases, leading to extremely high voltages when biased with current. Measurements were first taken at room temperature and then subsequently at higher temperatures in steps of 25-50°C, until reaching 576°C. The temperature was then ramped back down to room temperature. The InAlN/GaN sample underwent two temperature cycles, while the process was repeated a third time for the AlGaN/GaN sample.

For the 12-hour high temperature test, the same measurements (10 measurements at each of three supply voltages) were taken at room temperature, and then the device was held at 576°C for 12 hours and subsequently returned to room temperature, where the measurements were taken once again.

4.1.2 Characterization of Chuck Temperature

Although the heating stage itself is capable of reaching 600°C, there was a substantial difference between the temperature of the stage and that of the device under test at high temperatures. To characterize the true temperature of the device throughout the experiment, a resistance temperature detector (RTD) was integrated with a Hall plate during a temperature sweep. The temperature difference between the chuck and the device was additionally confirmed during a temperature sweep

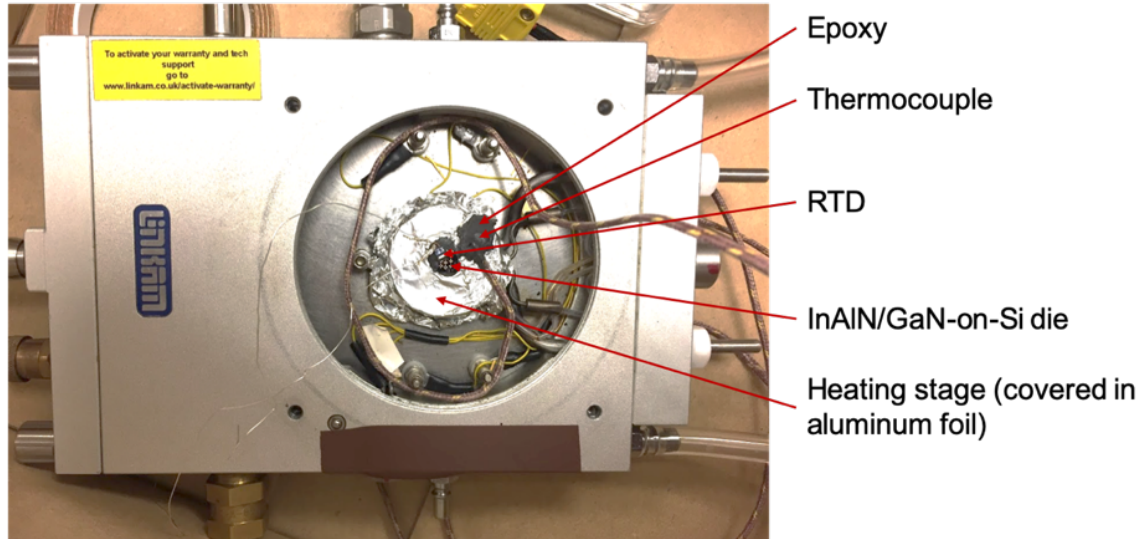


Figure 4.2: Image of test setup used to characterize difference of temperature between the control unit setting and the chuck itself. Reprinted from [73], with the permission of AIP Publishing.

up to 200°C in which a thermocouple was epoxied to the aluminum sheet in the same manner as the devices under test, shown in Fig. 4.2. The temperature readouts between the thermocouple and the RTD matched to within 1.3% and thus are the temperatures reported here (see Table 4.1).

4.1.3 Voltage-Scaled Sensitivity

Fig. 4.3 plots the voltage-scaled sensitivity from room temperature to 576°C for the InAlN/GaN and AlGaIn/GaN devices with a bias voltage of 0.3 V. The voltage-scaled sensitivities dropped from 53 to 8.3 mV/V/T for the InAlN/GaN sample and from 89 to 8.5 mV/V/T for the AlGaIn/GaN sample over the temperature range. The mobility of the 2DEG was calculated from Equation 3,

TC Temperature	RTD Temperature	Percent Difference
20.8	20.8	0.1%
44.5	44.6	0.3%
84.2	83.6	-0.7%
125.1	123.5	-1.3%
160.9	161.3	0.05%
200	200.8	0.4%

Table 4.1: Comparison of temperatures measured by the thermocouple (TC) and the resistance temperature detector (RTD). Reprinted from [73], with the permission of AIP Publishing.

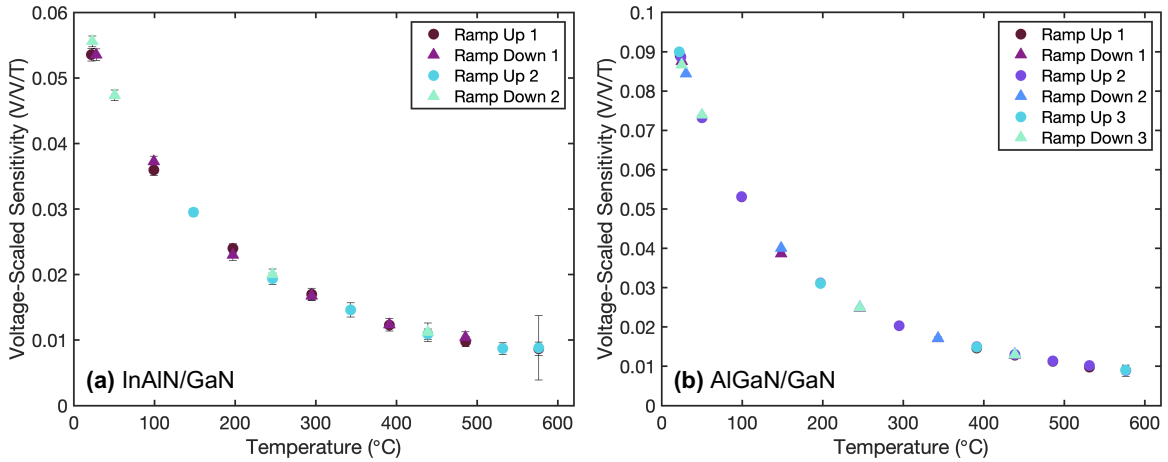


Figure 4.3: Voltage-scaled sensitivity of (a) InAlN/GaN and (b) AlGaIn/GaN samples between room temperature and 576°C. Reprinted from [73], with the permission of AIP Publishing.

using the voltage-scaled sensitivity, geometry factor, and the scattering factor of the device. Fig. 4.4 plots the temperature dependence of the mobility for the InAlN/GaN and AlGaIn/GaN Hall-effect sensors. The devices have a room temperature mobility of 1052 cm²/V·s and 1704 cm²/V·s for the InAlN/GaN and AlGaIn/GaN respectively, and a mobility of 169 cm²/V·s and 172 cm²/V·s at 576°C. The mobility decrease with increasing temperature follows a power law of $0.11 \times (T/300K)^{-1.79}$ for the InAlN/GaN sample and $0.18 \times (T/300K)^{-2.35}$ for the AlGaIn/GaN sample, which agrees with many results published in literature [145]. The decline in voltage-scaled sensitivity at high temperature is largely due to the corresponding decrease in electron mobility, caused by increased scattering at high temperatures [146]. The fact that the mobility of the InAlN/GaN and AlGaIn/GaN samples are quite different at room temperature but similar at high temperature suggests that while the dominant scattering mechanism at room temperature differs between the two materials, polar optical phonon scattering likely dominates in both materials at high temperature.

4.1.4 Current-Scaled Sensitivity

The current-scaled sensitivity of the two devices stayed relatively constant with temperature (Fig. 4.5), indicating a stable 2DEG sheet density (Fig. 4.6). The current-scaled sensitivity varied by 13.1% from the mean of 26.3 V/A/T for the InAlN/GaN sample and 10.5% from the mean of 60.2 V/A/T for the AlGaIn/GaN sample over the whole temperature range. Upon closer examination, during the first temperature ramp, the AlGaIn/GaN showed a decrease in 2DEG density until about 350-400°C and then subsequently an increase (inset of Fig. 4.6). This same behavior was described in Ref. [72] and attributed to conduction band lowering. However, in the subsequent temperature ramps this profile flattened out dramatically (Fig. 4.7), suggesting that conduction

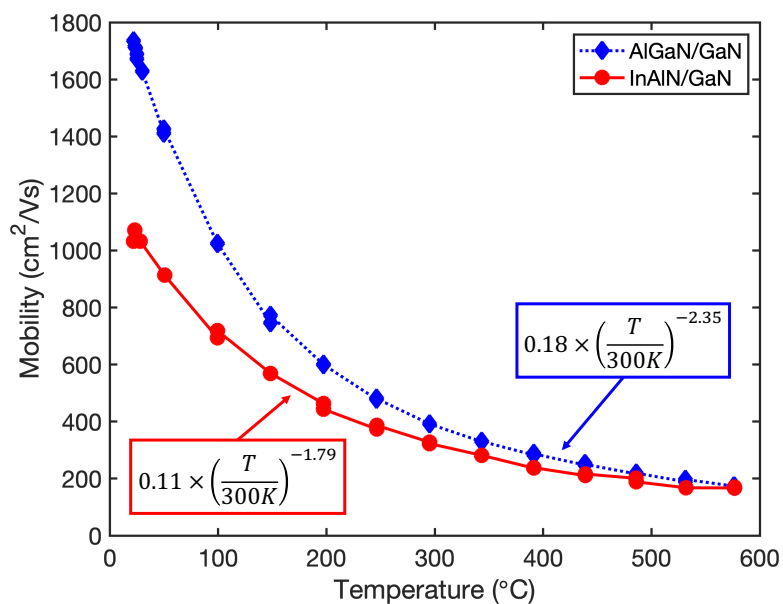


Figure 4.4: Mobility of AlGaIn/GaN and InAlN/GaN samples between room temperature and 576°C. Reprinted from [73], with the permission of AIP Publishing.

band lowering may not actually be the sole cause of this behavior.

Another change that appeared to take place between the first temperature cycle and the ensuing cycles was the current-scaled sensitivity at room temperature. For both material platforms, the current-scaled sensitivity was at its minimum the first time it was measured, and it then increased in following cycles. While we at first attributed this to a permanent change in the material (e.g., thermally-induced strain), conducting further testing revealed this same behavior (having the lowest sensitivity at the start of the first thermal cycle) many days later. One possible explanation is that moisture that accumulated on the device was burned off during the first temperature cycle, temporarily changing the device resistance [147]. This hypothesis could be tested by examining the behavior of devices with passivation layers, which may prevent moisture from reaching the device surface. Alternatively, the devices could be stored and tested in an inert gas environment. Another possibility is that the electronics and equipment require a certain amount of time to warm up, which could be easily tested by running equally long tests just at room temperature and seeing how the sensitivity changes.

4.1.5 12-Hour High Temperature Exposure

Sensitivity measurements taken before and after storing an AlGaIn/GaN device at 576°C for 12 hours showed the ability of the sensor to survive extreme temperatures for an extended period of time. The voltage-scaled sensitivity changed from 92 mV/V/T before being subjected to high temperature to

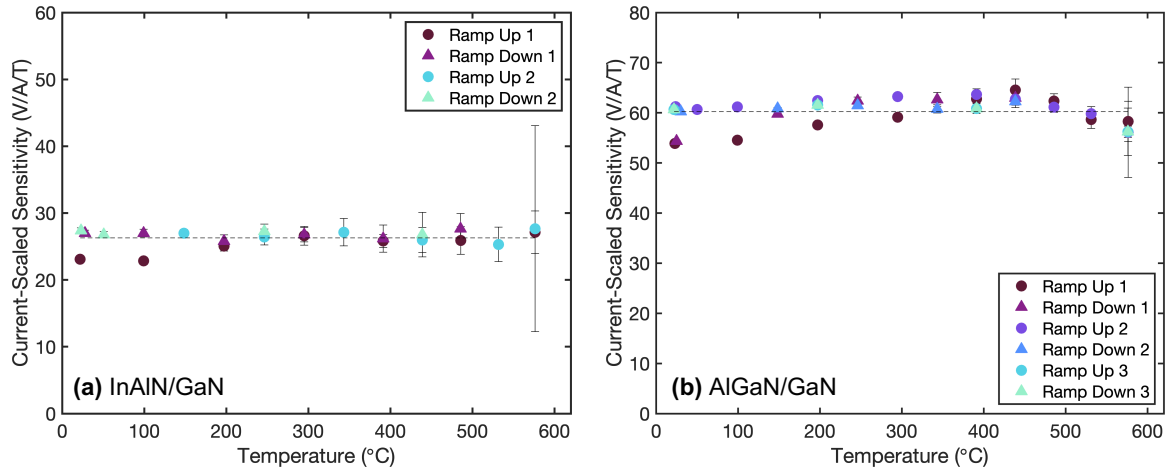


Figure 4.5: Current-scaled sensitivity of (a) InAlN/GaN and (b) AlGaIn/GaN samples between room temperature and 576°C. Reprinted from [73], with the permission of AIP Publishing.

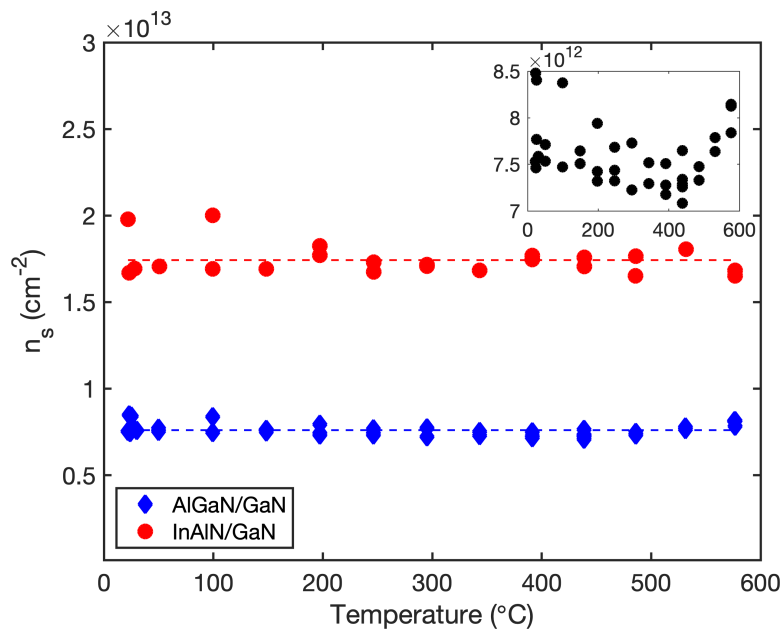


Figure 4.6: 2DEG sheet density of InAlN/GaN and AlGaIn/GaN samples as a function of temperature from room temperature to 576°C. The inset shows the AlGaIn/GaN 2DEG sheet density over temperature on tighter axes. Reprinted from [73], with the permission of AIP Publishing.

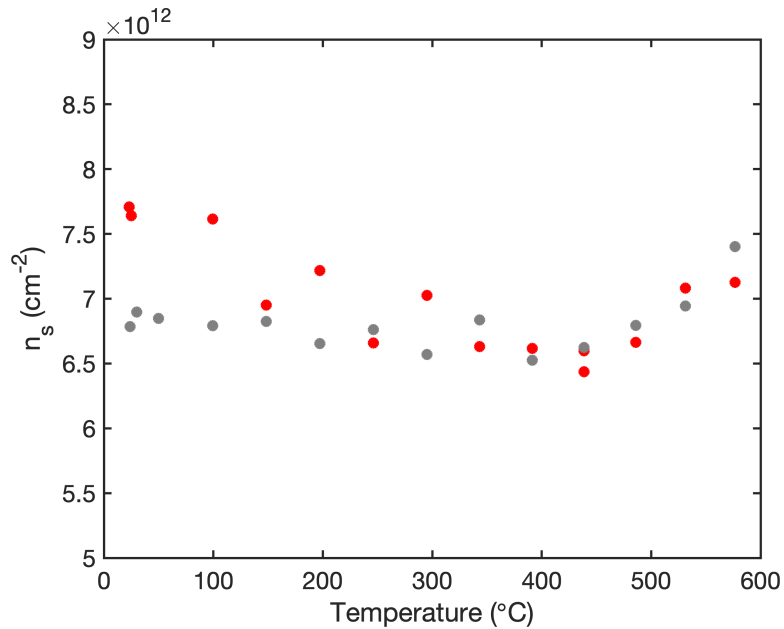


Figure 4.7: 2DEG sheet density as a function of temperature, with first temperature cycle depicted with red markers and ensuing temperature cycles with gray. Reprinted from [73], with the permission of AIP Publishing.

86 mV/V/T afterward, while the current-scaled sensitivity changed from 38.9 V/A/T to 39.7 V/A/T. Thus, the voltage- and current-scaled sensitivities shifted by -6.5% and 2.6% respectively, suggesting nearly full recovery. The variation between the ten measurements taken before the thermal storage was less than 1% for both sensitivity metrics, as was also the case for the ten measurements taken after thermal storage.

4.1.6 Reliability and Accelerated Aging Testing

InAlN/GaN Hall-effect sensors

Ten InAlN/GaN devices of differing sizes and geometries underwent 96 hours of a high temperature storage (HTS) test at 450°C, as part of an effort to characterize lifetime and degradation modes of the sensors in various harsh conditions. I-V curves were taken before the HTS test started and then again after 8 hours, 16 hours, 24 hours, 48 hours, and 96 hours. The resistances of the ten devices are plotted in Fig. 4.8. Most of the devices had a <10% change in resistance over the course of the test. While for the first 48 hours it appeared that there was no strong correlation between device size or geometry and change in resistance, after 96 hours, it became apparent that the devices with the smallest contacts may be more impacted by the high temperature exposure. One explanation for this is that over the course of the high temperature storage test, a void or high resistance alloy

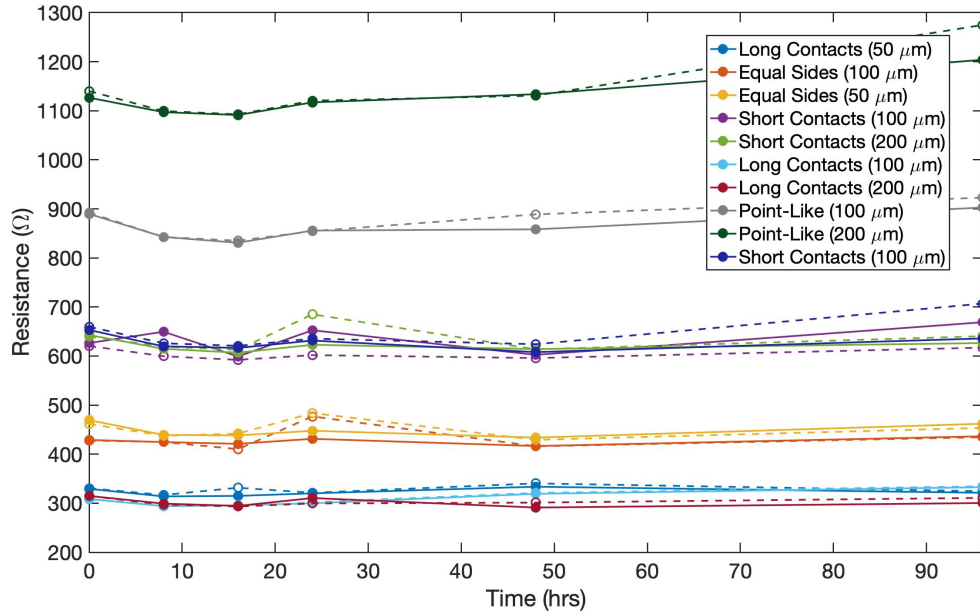


Figure 4.8: Resistance of ten InAlN/GaN devices measured throughout 96-hour storage at 450°C.

may form in the contact and take up a certain amount of space. This defect would cover a larger portion of the area for devices with smaller contacts than for devices with larger contacts. Thus, for devices with small contacts, these defects would more significantly hinder the flow of electrons, leading to a larger change in device resistance.

SEM images were taken before and throughout the HTS tests. Fig. 4.9 shows images of a device before the high temperature exposure and then after 8 hours, 16 hours, and 24 hours at 450°C. There is very little change in the appearance of the device over the course of the HTS test; the contacts were very stable and did not show any evidence of metal migration or intermixing.

AlGaIn/GaN Hall-effect Sensors

In contrast to the InAlN/GaN Hall-effect sensors, Fig. 4.10 shows the resistance of five AlGaIn/GaN devices from a previous fabrication run (described in [144]) over the course of 368 hours at 450°C. These devices had a different contact stack (Ti/Al/Pt/Au) and a 50 nm alumina (Al_2O_3) passivation layer. Additionally, there were various known issues with these devices; I-V curves showed that the contacts were not perfectly Ohmic, the device resistance varied with supply voltage by $-5\%/V$ resulting in large residual offsets (2-4 mT), and an analysis of the noise characteristics of these devices showed extremely high Hooge parameters and corner frequencies (on the order of 10^4 - 10^6 [62]). A major contributor to the low quality of the contacts is likely a slight mask misalignment

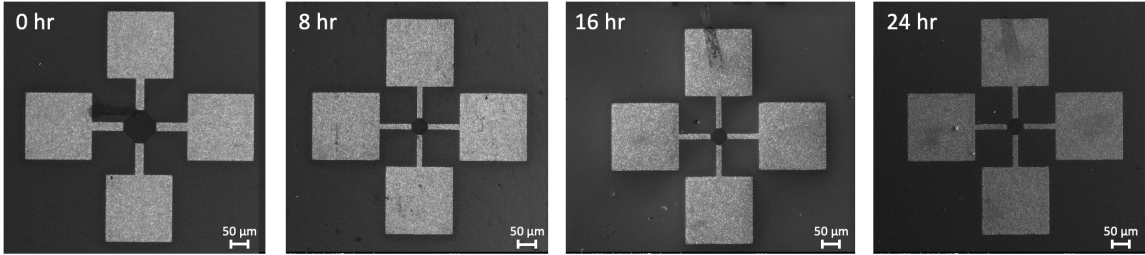


Figure 4.9: SEM images of an InAlN/GaN device before the high temperature exposure and then after 8 hours, 16 hours, and 24 hours at 450°C. The last three images are all of the 50- μm device with short contacts, while the first image is of the 100- μm device of the same geometry.

during fabrication, which resulted in two issues, described below.

1. The *transfer length* of a contact is the average distance that a carrier travels below the contact in a semiconductor before it flows up into the contact, and can be thought of as the effective length of the contact. To make contacts symmetric, it is important to either (a) have identical overlaps between the semiconductor and the contact for every contact, or (b) have the overlap be larger than the transfer length, so that the effective length of all contacts is just the transfer length. In this device, the overlap between the AlGaIn/GaN mesa structure and the Ohmic contact was designed to be 5 μm . However, the transfer length (L_T) was calculated by

$$L_T = \sqrt{\frac{\rho_c}{R_{sh}}} \quad (4.1)$$

to be $\sim 4.4 \mu\text{m}$. Thus, a mask misalignment by just 1 μm would result in asymmetric contacts. The difference in contact lengths, and thus resistances, can lead to asymmetric heating profiles and high offsets.

2. The mask misalignment may have resulted in exposed surfaces (not passivated) on the contact pad, which could result in increased interdiffusion events at high temperatures.

From Fig. 4.10, it is clear that the majority of the change throughout the 368 hours HTS test at 450°C occurred within the first 25 hours of the exposure, and there was essentially no change beyond 50 hours. SEM images (such as Fig. 4.11) showed several changes in the contacts throughout the HTS test. The SEM images, in combination with X-ray photoelectron spectroscopy (XPS) analysis, showed contact pad cracking, gallium out-diffusion, and metal intermixing. Gallium has been shown to have increased out-diffusion and wear in the presence of water vapor and humid conditions [148]; thus, performing these tests in an ambient environment may have contributed to this problem.

These AlGaIn/GaN devices showed different changes in resistance during 200°C and 600°C exposure tests. The devices were exposed to 200°C for 1200 hours and showed a steady increase in

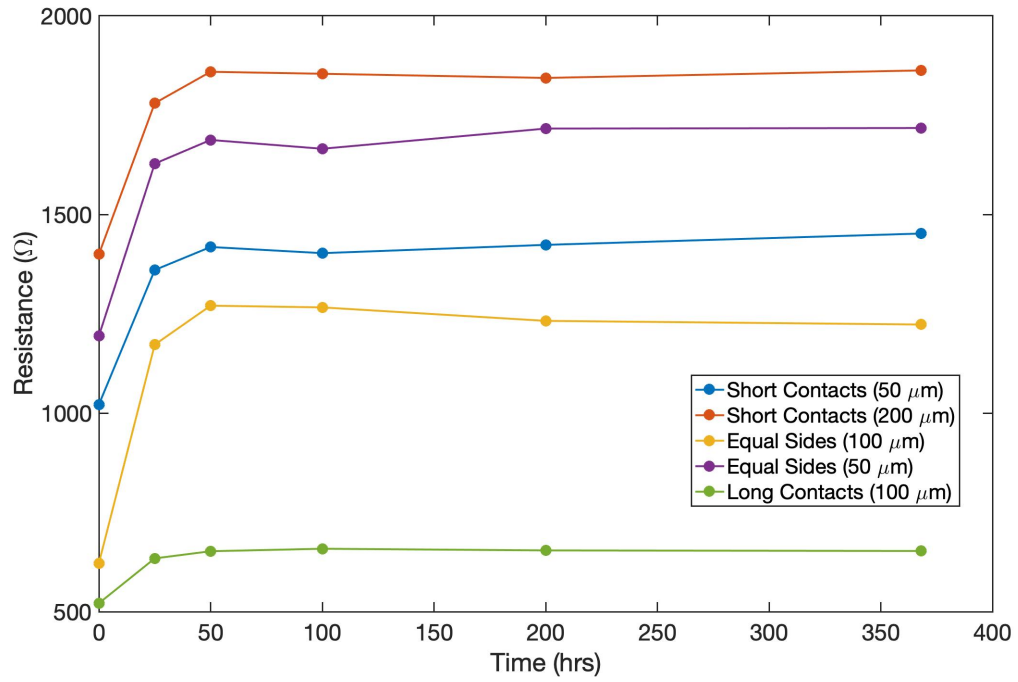


Figure 4.10: Resistance of five AlGaIn/GaN devices measured throughout 368-hour storage at 450°C.

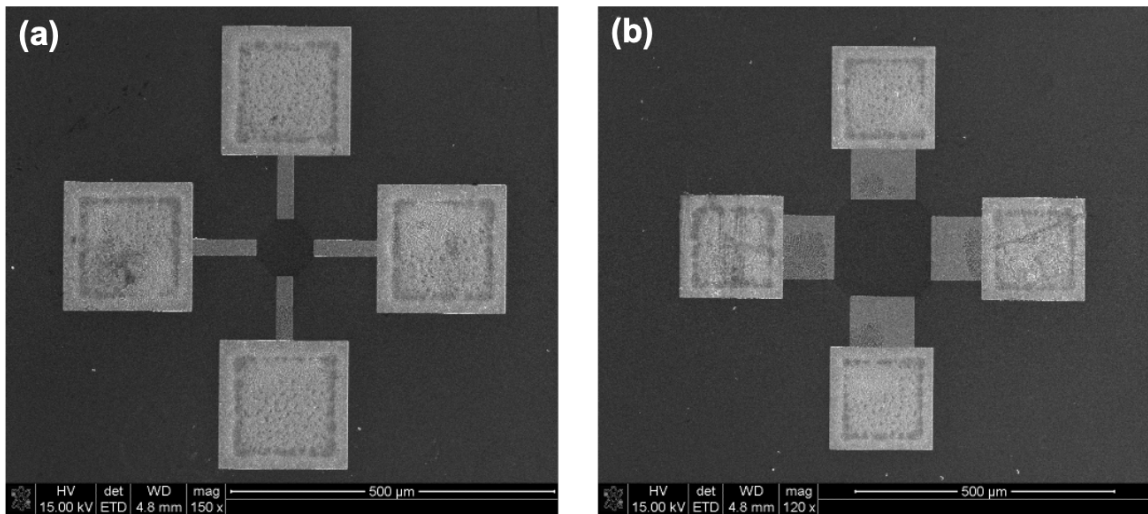


Figure 4.11: SEM images of two AlGaIn/GaN devices after being exposed to 450°C for 368 hours.

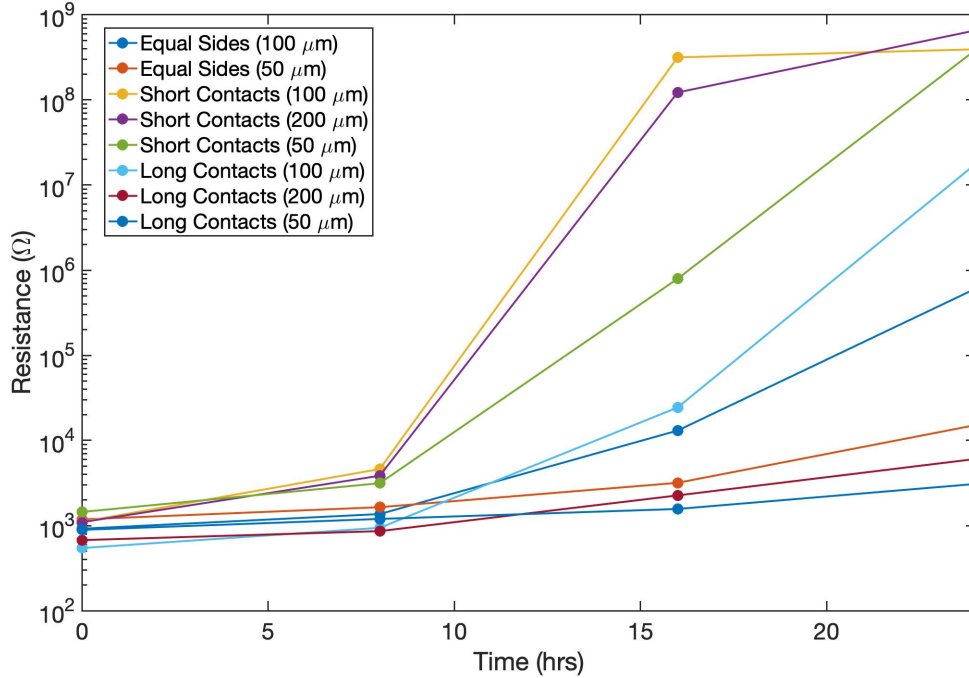


Figure 4.12: Resistance of eight AlGaIn/GaN devices measured throughout 24-hour storage at 600°C.

resistance throughout that time, but did not exhibit a plateau as seen in the 450°C case. Over the course of the HTS test, most devices showed a trend of linearly rising resistance, eventually reaching an increase by ~10-20% after 1200 hours.

During the 600°C HTS test, the first measurements took place after 8 hours. Many of the devices with shorter contacts showed increases in resistance of up to a factor of 10 just within the first 8 hours. Other devices showed milder increases after 8 hours, but eventually also exhibited a large increase in resistance by up to a factor of ~100 after 16 to 24 hours, as shown in Fig. 4.12.

4.2 Outer Space Environments

4.2.1 Venus Chamber

Three InAlN/GaN Hall-effect plates (one passivated and two unpassivated) were exposed to a Venus-analogue environment for 244 hours. The environment included a temperature of 460°C, a CO₂ atmosphere, and a pressure of 96.5 bar. While subsequent tests will also include sulphuric acid, this test did not. Fig. 4.13 shows five sensitivity measurements taken before and after exposure in the Venus chamber. The devices tended to exhibit <10% change in sensitivity before and after the test.

Additionally, measurements of mobility, sheet resistance, and 2DEG sheet density were taken of the samples that had been exposed to the Venus-analogue environment as well as virgin samples. The results, summarized in table 4.2, show that there was very little difference in the mobility and sheet resistance between the samples that had been exposed to the Venus environment and those that had not. The differences between the values can be attributed to die-to-die variation, thus indicating that the 2DEG properties in the InAlN/GaN heterostructure were preserved after the prolonged exposure to the harsh Venusian conditions.

This study was one of the first to investigate the electrical integrity of GaN heterostructures in a Venus-analog environment; the promising results suggest that GaN-based devices have potential applications in the collection and readout of sensor data in for Venus exploration.

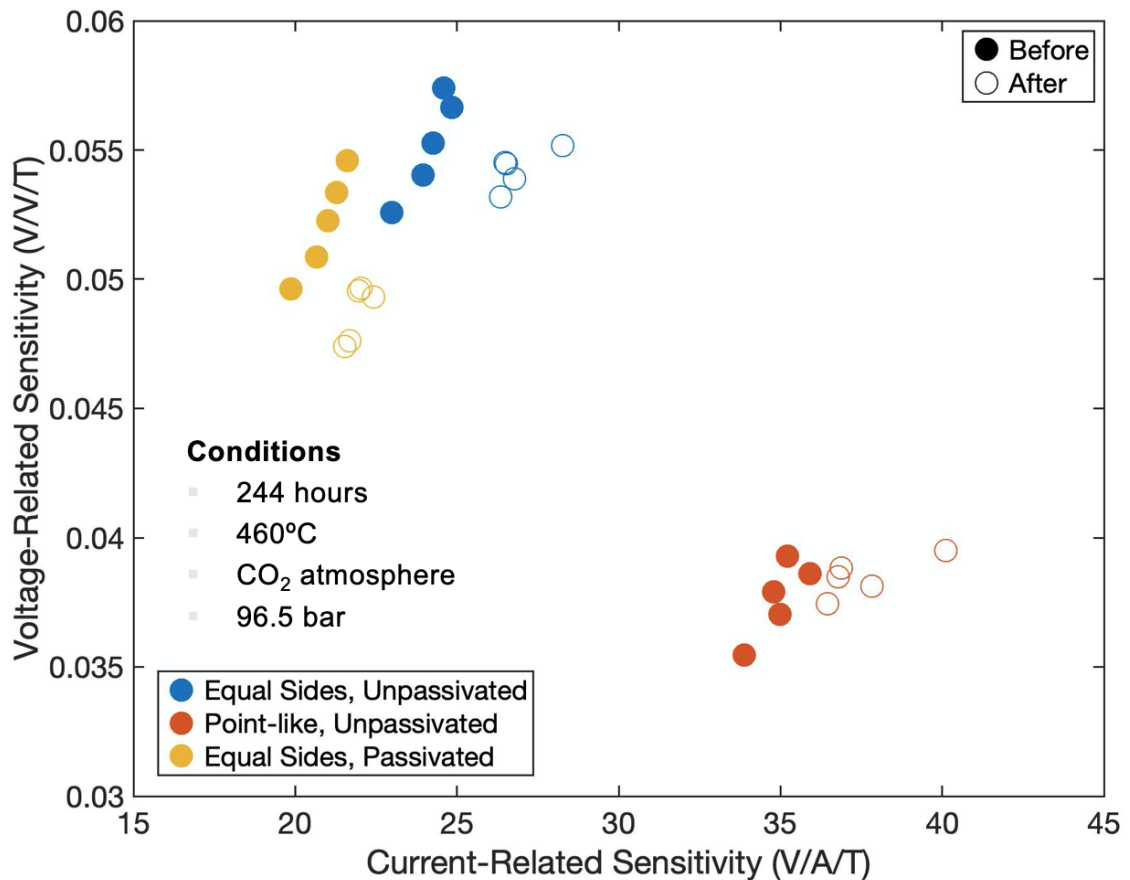


Figure 4.13: Voltage-scaled sensitivity vs. current-scaled sensitivity for three InAlN/GaN Hall-effect sensors before (solid points) and after (open points) exposure in Venus chamber.

	ρ_s (Ω/\square)	μ ($cm^2/V \cdot s$)	n_s (cm^{-2})
Virgin Sample, Unpassivated	272	1124	2.04×10^{13}
Post-Venus Chamber, Unpassivated	302	1076	1.92×10^{13}
Virgin Sample, Passivated	252	1031	2.41×10^{13}
Post-Venus Chamber, Passivated	248	1026	2.45×10^{13}

Table 4.2: Sheet resistance, mobility, and 2DEG carrier concentration of devices that were exposed to a Venus environment and identical devices that had not be exposed.

4.2.2 KickSat-2

KickSat-2 was a CubeSat mission led by Prof. Zachary Manchester that put 100 “Sprites” (3.5 cm \times 3.5 cm spacecraft made on PCBs) into space. Each Sprite contained its own microcontroller, radio, and solar cells, and some also included their own sensor payloads. The goals of the project were (1) to present a platform that would dramatically decrease the cost of spaceflight and (2) demonstrate swarming and networking algorithms that allow the Sprites to communicate with one another as well as with ground stations [149].

Two 5 mm \times 5 mm chips containing multiple functional InAlN/GaN Hall-effect sensors were integrated into the motherboard of the CubeSat (Fig. 4.14). KickSat-2 was launched to the International Space Station (ISS) on November 17, 2018 on the Cygnus spacecraft, and the CubeSat was deployed for operation in March of 2019. Fig. 4.15 shows a NASA image of the Cygnus spacecraft docked with the ISS, where KickSat-2 can be seen attached near the docking arm of the ISS. The Hall-effect sensors collected data for 52 days in orbit and survived the whole time (the data packets did not contain any “device-failure” flags). Dosimeter data from a radiation sensor (“RadFET”) on the motherboard shows an accumulated dose of 34 Rads over the 90 days in which the CubeSat was docked to the ISS [150].

Because of the difficulty of decoding data packets (due to the nature of the radio modulation scheme as well as variable signal integrity from crowd-sourced ground stations), much of the Hall-effect sensor data has not been decoded. Data packets collected from a high-gain antenna in the Netherlands proved easiest to decode, and as such a few of these data packets were decoded manually by Prof. Manchester. The measurements from one Hall-effect sensor over the course of eight days are shown in Fig. 4.16; these data points show evidence of consistent readings throughout that period. The three points vary by up to 18% from the mean, which is certainly within the range of the magnetic field variation due to changes in CubeSat orientation, electronic components, and environmental conditions.

4.2.3 Radiation Testing

In conjunction with sending the Hall-effect sensors into low Earth orbit, the devices were tested in a controlled radiation environment at NASA Ames. Four different sensors underwent *in situ* testing:

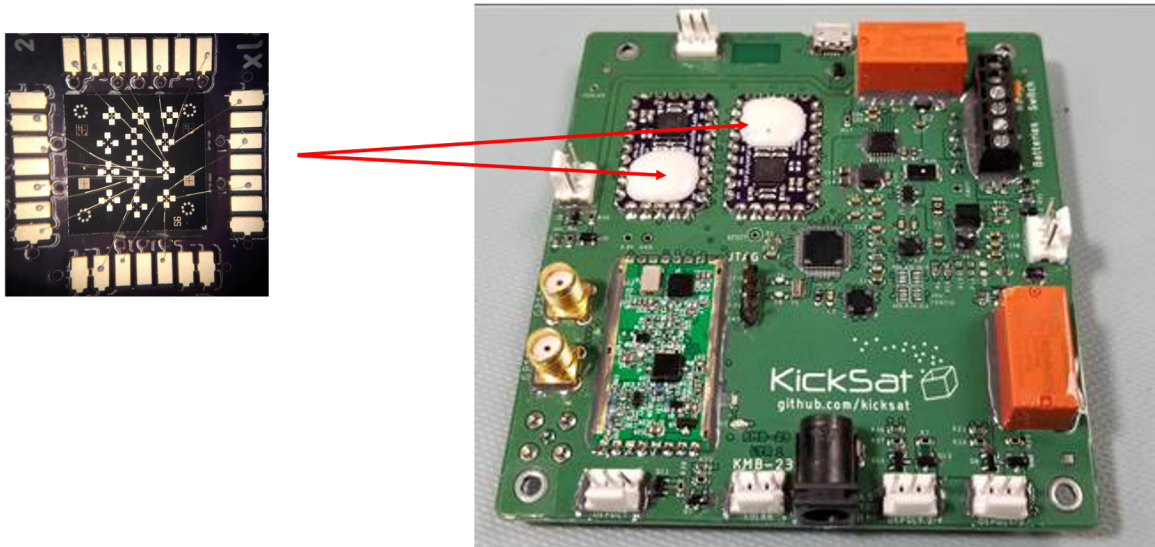


Figure 4.14: Image of $5\text{ mm} \times 5\text{ mm}$ chip containing InAlN/GaN Hall-effect sensors and the KickSat-2 motherboards on which they were integrated.

two devices with long contacts and two devices with short contacts, with one passivated and one unpassivated of each geometry. The resistance across the devices were measured as they were exposed to ~ 20 krad of gamma radiation. In Fig. 4.17, bumps near the beginning of radiation exposure can be seen, particularly in the unpassivated device with short contacts. This initial dip in resistance may be attributed to a parasitic capacitance within the device. Additionally, the unpassivated devices showed a greater change in resistance than the passivated ones, suggesting that the change in resistance could be related to speed with which trapped charges can move through the material. Overall, the ~ 20 krad dose of gamma radiation had very little effect on device performance, and as such the behavior of the sensors under a higher dose and different types of radiation should be investigated.

4.3 Conclusions

In this chapter, we investigated the functionality of AlGaIn/GaN and InAlN/GaN Hall-effect sensors in various space-relevant environments, including in high temperatures, in Venus-analogue conditions, and on a CubeSat in low Earth orbit. We characterized the sensitivity of Hall-effect sensors up to a record high temperature of 576°C . The Hall-effect sensors showed continued functionality at high temperature, little hysteresis through 2-3 thermal cycles, and full recovery of its initial performance characteristics at room temperature. The long-term high temperature study of the InAlN/GaN Hall-effect sensor, combined with the 244-hour Venus chamber exposure and the 52 days it spent in low Earth orbit, further suggest the viability of this material platform, including the

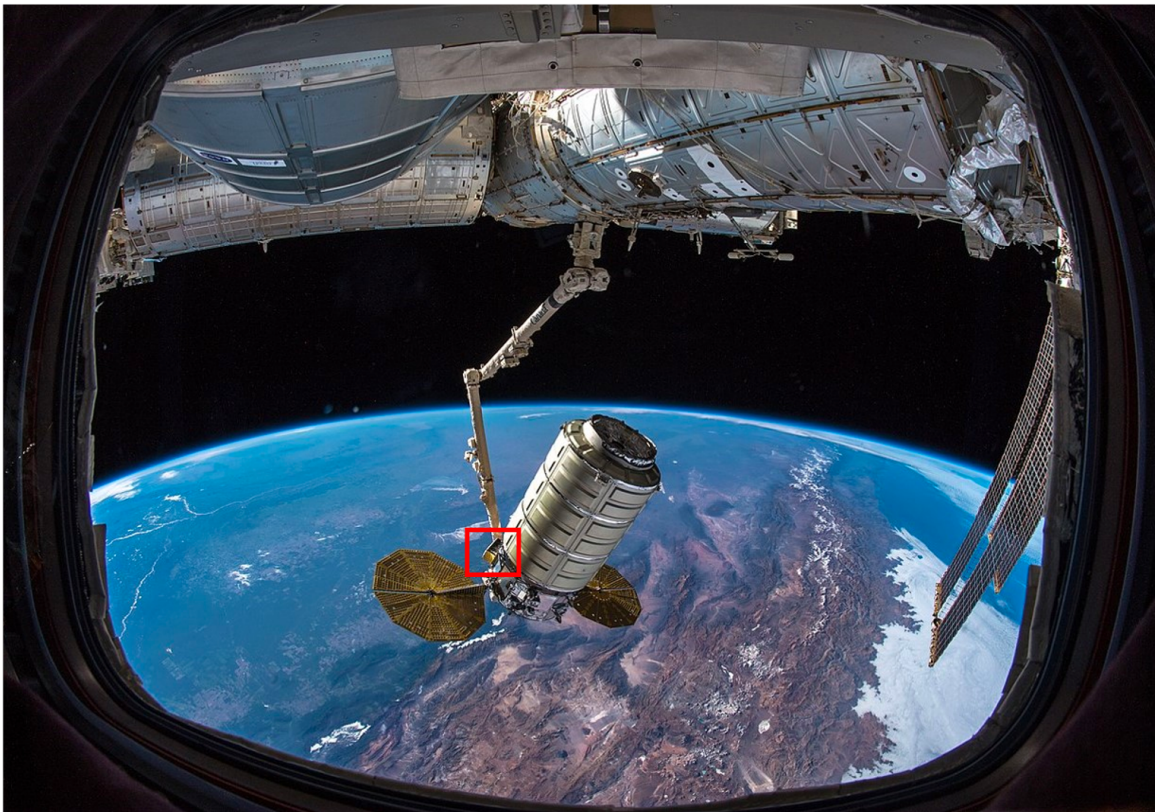


Figure 4.15: NASA image of the Cygnus spacecraft docked with the ISS, where KickSat-2 can be seen attached near the docking arm of the ISS.

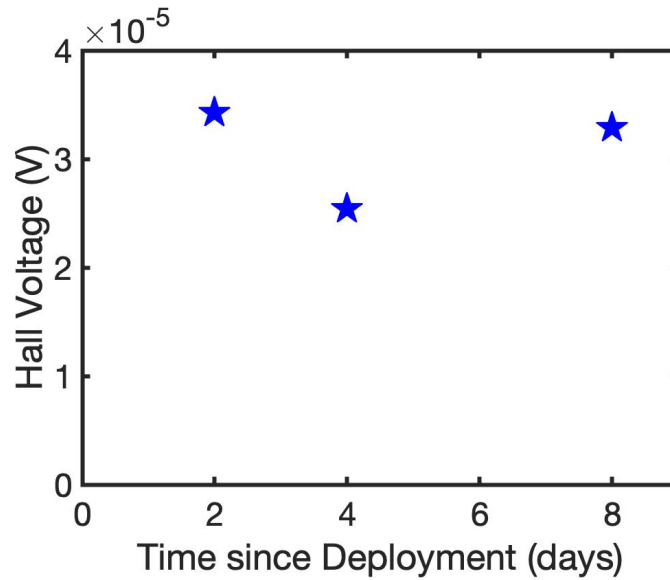


Figure 4.16: Plot of Hall-effect sensor measurements from KickSat-2 over 8 days in orbit.

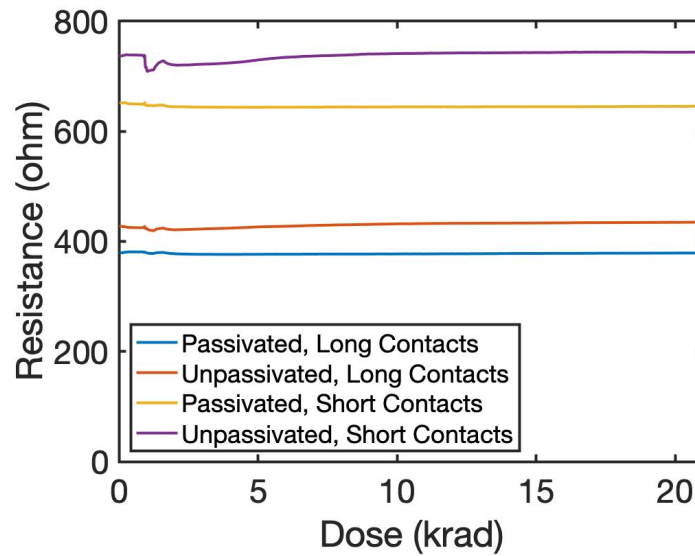


Figure 4.17: Plot of resistance measurements across Hall-effect sensors during exposure to ~ 20 krad of gamma radiation.

contact stack, for use in high temperature and space environments for an extended period of time.

Chapter 5

Ultraviolet Photodetectors

In this chapter the performance of AlGaIn/GaN UV photodetectors under high temperatures is examined. Much of this chapter was previously published in [151] (© 2019 IEEE).

5.1 AlGaIn/GaN UV Photodetector

An image and cross-sectional diagram of the UV photodetector used in this study, designed by Satterthwaite and Yalamarthy et al. (2018), is shown in Fig. 5.1. The device active area is $200 \mu\text{m} \times 200 \mu\text{m}$ and contains 13 pairs of 2DEG interdigitated transducers (IDT). The gain of the device, further described in [83], was found to be

$$G = \frac{n_e(\phi_b)\mu_e V}{n_{ph,tot}L}, \quad (5.1)$$

where $n_e(\phi_b)$ is the number of carriers per unit volume with enough energy to overcome the barrier keeping them in the 2DEG quantum well, μ_e is the electron mobility, V is the applied voltage, L is the spacing between the 2DEG electrodes, and $n_{ph,tot}$ is the number of photons incident on the photodetector. The number of electrons with sufficient energy to escape the 2DEG is approximated as

$$n_e(\phi_b) = \frac{k_b T m^*}{\pi \hbar^2} e^{-\frac{q(\phi_b - \Delta\phi_b)}{k_b T}}. \quad (5.2)$$

Here, T is the operating temperature, m^* is the effective mass, ϕ_b is the energy separation between the Fermi level in the 2DEG and top of the GaN conduction band, and $\Delta\phi_b$ is the amount of barrier lowering due to hole accumulation (illustrated in Fig. 2.10b). Thus, more hole accumulation leads to a higher gain, while less hole accumulation leads to a lower gain.

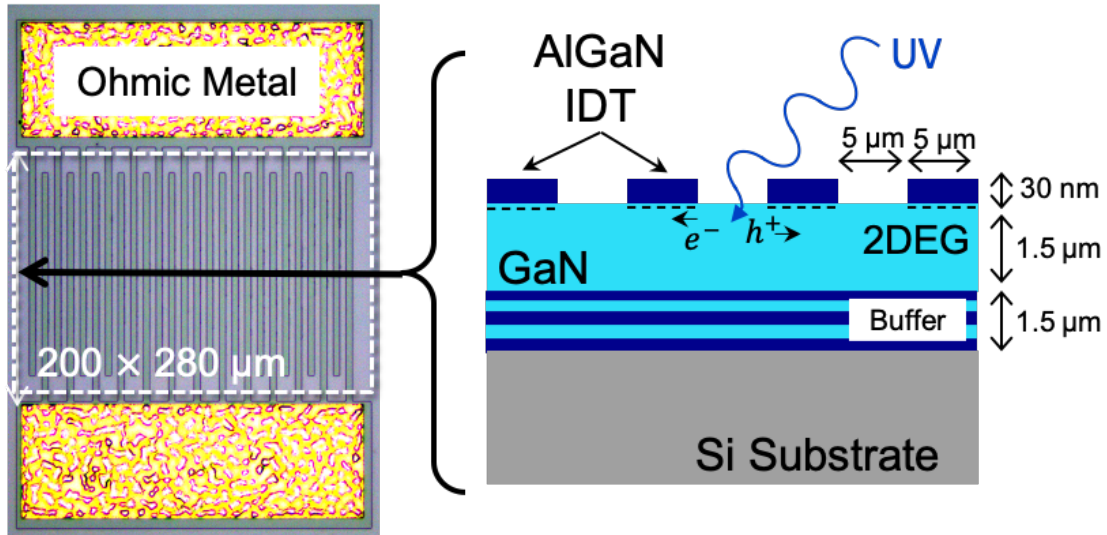


Figure 5.1: Image and cross-sectional diagram of AlGaN/GaN UV photodetector.

5.2 Device Calibration

In order to understand the optical properties of the device, we characterized its spectral response across a wide range of incident powers, from $\sim 10^4$ mW/cm² to ~ 1.5 mW/cm². An example of the spectral response at an optical power of $\sim 4 \times 10^{-3}$ mW/cm² is illustrated in Fig. 5.2. Here, it is seen that the responsivity peaks at a wavelength of ~ 362 nm. Further, the spectral response can be modeled as a rectangular window with a height corresponding to the peak responsivity at 362 nm (433 A/W) and a width of 16 nm. Fig. 5.2 also shows a UV-to-visible (362 nm to 425 nm) ratio of 4×10^6 . The variation in the responsivity across the range of incident optical powers at a wavelength of 362 nm is illustrated in Fig. 5.3a. The peak responsivity of ~ 7800 A/W occurs at a power of ~ 1 mW/cm². Since the area of the device is known, we can convert the responsivity into a measurement of the current across the device, which yields a calibration curve of the current versus the total optical power on the device, as shown in Fig. 5.3b. The calibration curve was constructed with data gathered on two different experimental setups - one for low power and one for high power. This calibration curve can be used to correlate the current measurement from the photodetector with the incident optical power on the device.

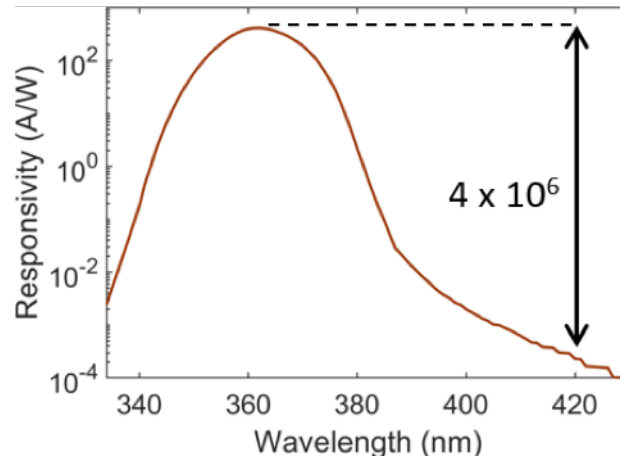


Figure 5.2: Spectral responsivity vs. wavelength, measured at a bias voltage of 5 V and incident power of 10^5 mW. © 2019 IEEE.

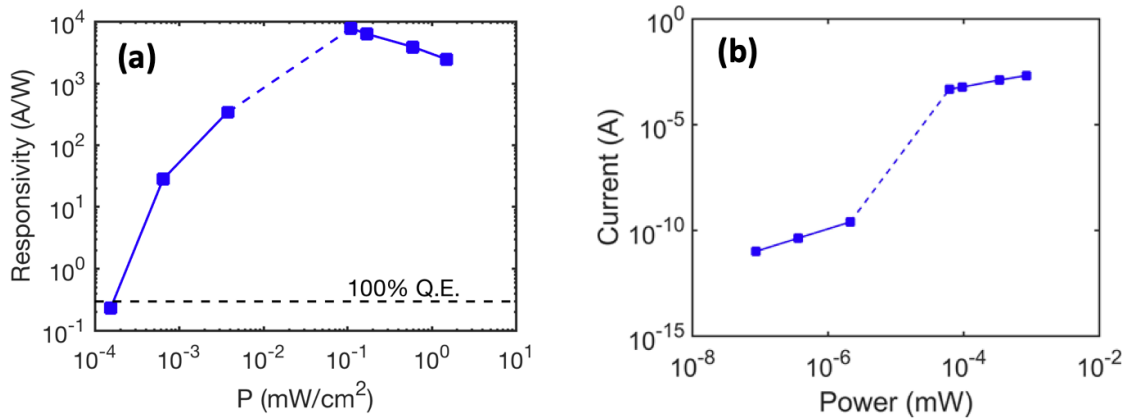


Figure 5.3: Plots of (a) responsivity versus incident power and (b) current versus incident power for a wide range of incident optical powers.

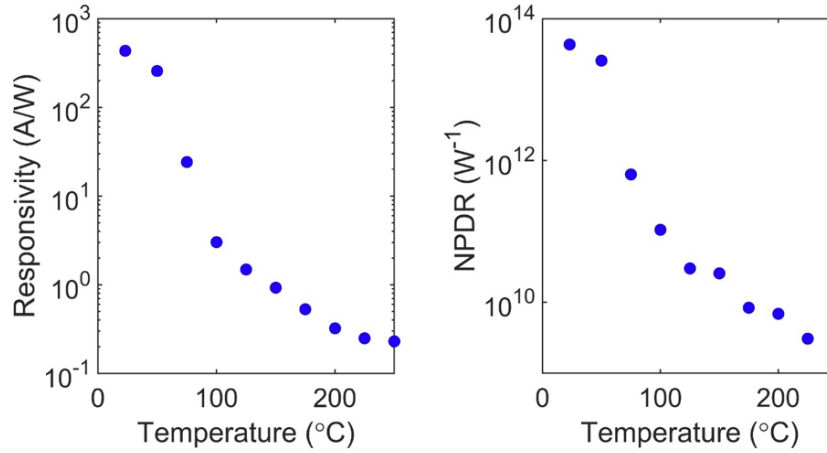


Figure 5.4: Plots of (a) responsivity and (b) Normalized photocurrent to dark current ratio (NPDR) versus temperature. © 2019 IEEE.

5.3 Extreme Environment Characterization of UV Photodetectors

5.3.1 High Temperature Testing

The high-temperature properties of the AlGaIn/GaN photodetector were investigated to evaluate its performance in extreme environment conditions. In these experiments, we fixed the incident optical power at $4 \times 10^{-3} \text{ mW/cm}^2$, although a similar trend is expected at other optical powers. The peak spectral responsivity of the photodetector fell by a factor of nearly 2,000 from room temperature to 250°C (Fig. 5.4a), but the NPDR still remained above 10^9 W^{-1} even at the highest temperatures (Fig. 5.4b), which is still higher than the values of several GaN photodetectors at room temperature in the published literature [152, 153, 154, 155, 156]. In particular, this NPDR of 10^9 W^{-1} at 250°C corresponds to a photocurrent-to-dark current ratio of ~ 20 , and thus amenable to photodetection at these high temperatures.

The steep fall in responsivity associated with the increase in temperature is the result of a combination of lower mobility of the charge carriers due to lattice scattering [146] as well as a higher recombination rate for the photo-excited electron-hole pairs. The previously described studies on Hall-effect sensors revealed that the electron mobility in the AlGaIn/GaN 2DEG drops by a factor of ~ 3 between room temperature and 250°C. Thus, the majority of decrease is likely due to the increased electron-hole pair recombination at high temperature. The increase in this rate leads to fewer electrons making it to the AlGaIn electrode before recombining with a hole, thus decreasing the photocurrent. Even more significantly, fewer holes are able to accumulate behind the AlGaIn

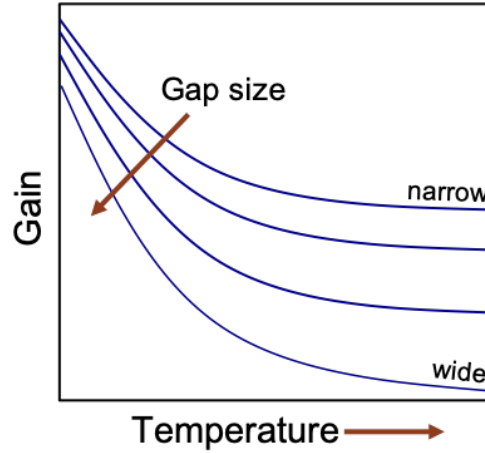


Figure 5.5: Expected trend of responsivity vs. temperature for devices with varying gap widths between electrodes. If the increase in electron-hole recombination rate is the main contributor to the responsivity reduction at high temperature, then devices with wider gaps would exhibit a greater decrease in responsivity.

barrier, which reduces the amount of barrier lowering. From Eqs. 5.1 and 5.2, it is clear that the gain is directly proportional to n_e , or the number of electrons with sufficient energy to escape from the 2DEG quantum well. However, n_e depends exponentially on the barrier lowering, so just a small change in hole population can cascade into a significant decrease in responsivity.

To test the hypothesis that the increased electron-hole pair recombination rate is the main contributor to the responsivity reduction at high temperature, we propose the following experiment. Measure the responsivity across the temperature range of a series of devices that have varying gap widths between electrodes, similar to those described in [83]. If the recombination rate is the driving factor in the responsivity decrease, then devices with larger gaps between electrodes will have a greater reduction in responsivity than those with smaller gaps because the electrons and holes have more time to recombine before reaching the electrodes. While all the devices will show some decrease in gain at high temperature, those with wider gaps will exhibit a more significant decrease, as illustrated in Fig. 5.5.

An additional effect of high temperature operation is that the wavelength at which the highest responsivity occurs shifted from ~ 362 nm at room temperature to ~ 375 nm at 250°C , as shown in 5.6a. This wavelength shift is due to the decrease in bandgap with increasing temperature. For GaN, the bandgap, in units of eV, is a function of temperature (T), and can be expressed using the Varshni parameters as [157]:

$$E_g = 3.51 - \frac{9.09 \times 10^{-4} \times T^2}{T + 830}. \quad (5.3)$$

The corresponding wavelengths for these temperature-dependent bandgaps are plotted in Fig. 5.6b,

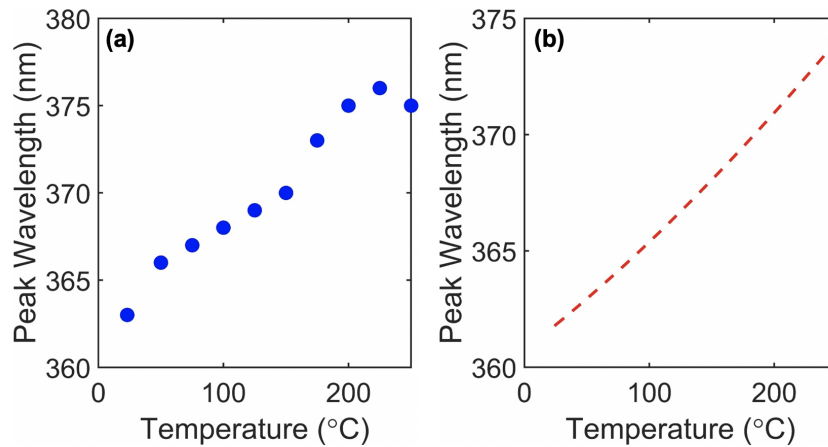


Figure 5.6: Plots of peak wavelength versus temperature for (a) measured data and (b) theoretical calculations. © 2019 IEEE.

showing excellent agreement with the experimentally measured wavelength where the peak responsivity occurs (Fig. 5.6a). This confirms that the shift to higher wavelengths of the peak spectral responsivity with temperature is due to the change in bandgap.

5.3.2 Venus Chamber Testing

Seven photodetectors were exposed to a Venus-analogue environment for 244 hours, as described in section 4.2.1. Tests of the response of the photodetectors before and after the Venus chamber exposure showed an average decrease in responsivity of 37% (Fig. 5.7). The decrease in responsivity is likely due to contact degradation, as was apparent from scanning electron microscope (SEM) images of devices that had undergone the Venus chamber testing as well as those that had not (Fig. 5.8).

5.4 Photodetector for Combustion Monitoring

After thorough characterization of the AlGaIn/GaN photodetectors at high temperature, they were implemented into a relevant aerospace system. Their low power consumption, fast response times, and ability to operate at high temperatures made them a good candidate for combustion monitoring. Photodetectors were used in two different experiments to monitor combustion in hybrid rocket motors. The first experiment was on a hybrid rocket motor igniter plume at the Jet Propulsion Lab (JPL), and the second was on a transparent hybrid rocket motor fuel grain at Stanford.

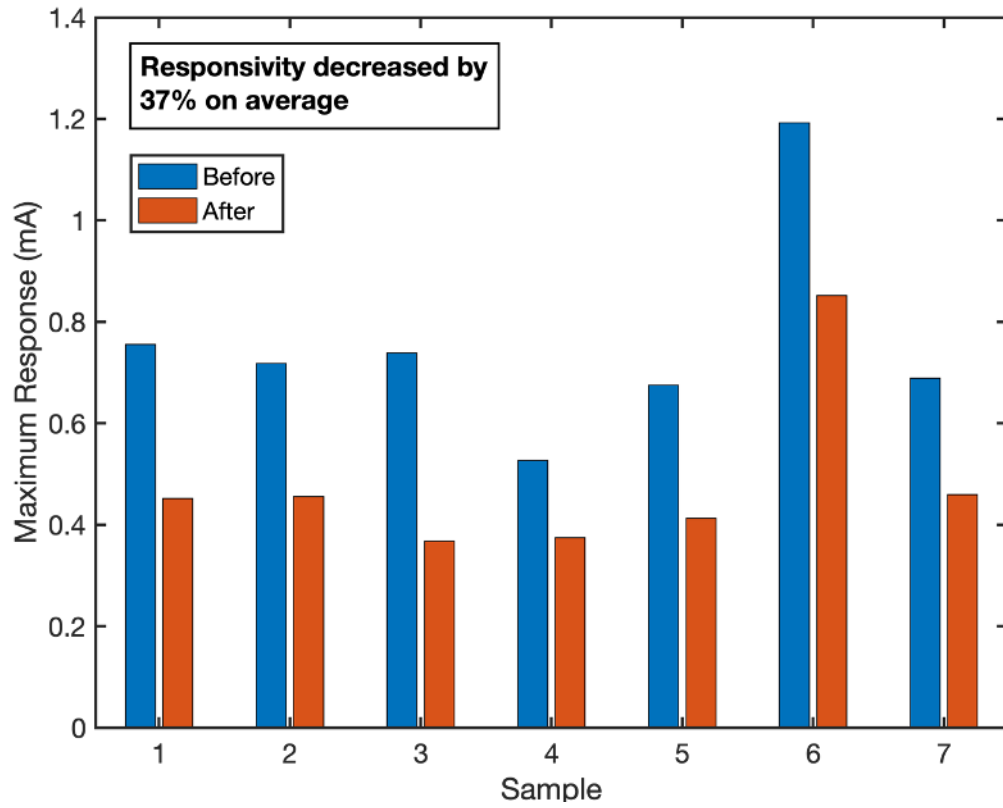


Figure 5.7: Response of photodetectors before and after exposure to Venus-analogue environment.

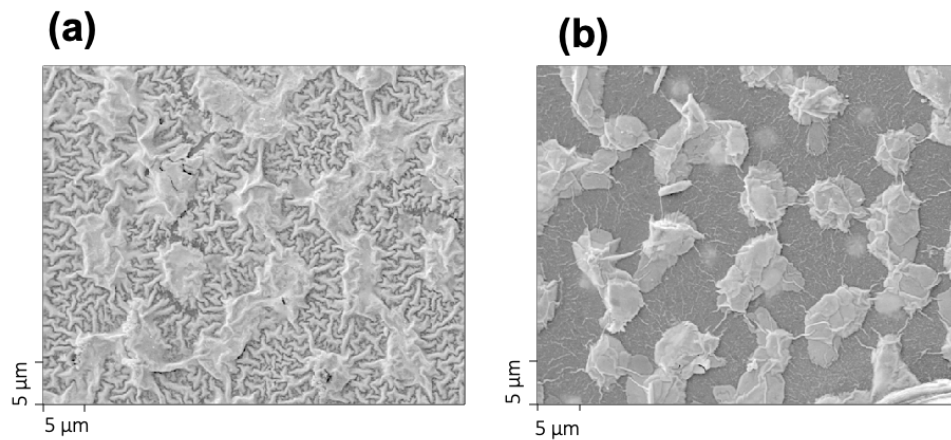


Figure 5.8: SEM images of photodetector contacts on photodetectors that (a) had not been exposed to Venus-analogue environment and (b) had been exposed to the Venus-analogue environment.

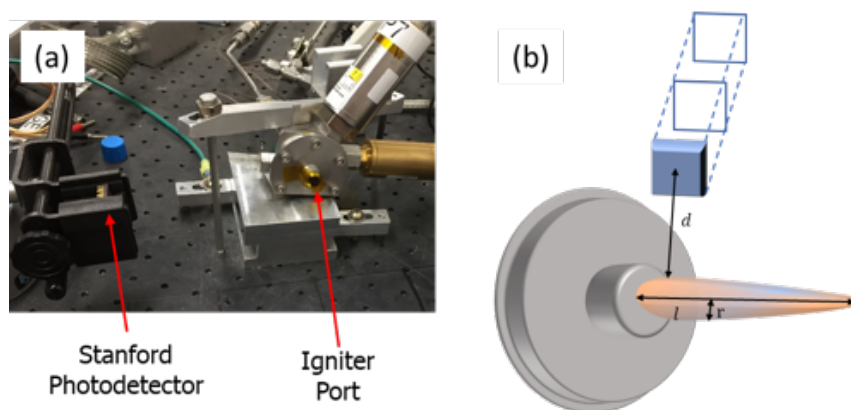


Figure 5.9: (a) Image of photodetector setup. The sensor is being held by the clamp on the left and the igniter plume is emitted from the hole in the middle. (b) Schematic of flame and photodetector where d is the radial distance between the two, l is the length of the flame, and r is the radius of the flame. © 2019 IEEE.

	Lean	Near Stoichiometric	Rich
CH ₄ Mass Flow Rate (g/s)	0.12	0.15-0.16	0.24
Oxidizer-to-Fuel Ratio	5.81-5.96	4.47-4.62	2.85-2.89
Average Chamber Pressure (psi)	70.0-72.8	82.6-84.4	104.6-109.1
Maximum Chamber Pressure (psi)	89.7-93.3	105.4-107.5	133.3-138.1

Table 5.1: Values associated with various test conditions. © 2019 IEEE.

5.4.1 JPL Hybrid Rocket Motor Igniter Plume

Experimental Methods

The AlGaIn/GaN photodetector was placed at three radial distances (3", 5.5", and 7") from the base of a hybrid rocket motor igniter plume, and the O₂/CH₄ oxidizer-to-fuel (O/F) ratio was varied to alter the size and strength of the plume. An image of the test setup is shown in Fig. 5.9a and a simplified diagram is illustrated in Fig. 5.9b. UV light from the entire plume is collected by the photodetector, since it is not collimated in our experimental setup. A more detailed description of the hybrid rocket motor and its characteristics can be found elsewhere [158]. A commercial spark plug was used to ignite the O₂/CH₄ mixture in the igniter combustion chamber. The feed pressure of oxygen was kept constant to provide a consistent mass flow rate of 0.70 g/s, while the methane pressure varied between 0.12 and 0.24 g/s to establish a range of O/F ratios. The igniter was fired under three conditions: lean, near stoichiometric, and rich, which correspond to O/F ratios by mass of 5.8, 4.5, and 2.9 respectively. The stoichiometric O/F ratio for the O₂/CH₄ reaction is 4.0. The average chamber pressures and maximum chamber pressures also varied for the different conditions, detailed in Table 5.1.

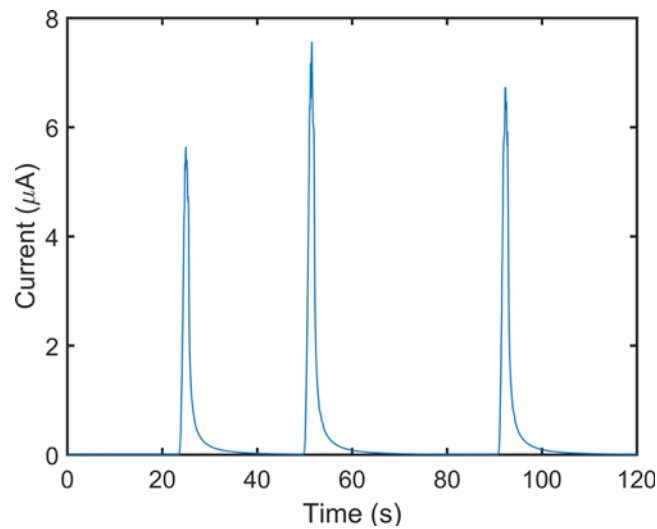


Figure 5.10: Plot of current measured across the photodetector versus time for a series of three fires. © 2019 IEEE.

The igniter was fired two to four times under each condition. Each burn lasted for one second and was followed by a three second purge and then a wait time of at least 30 seconds before the next burn. A sourcemeter (Keithley 2400) was used to bias the photodetector at 5 V and measure the device current at a sample rate of ~ 13.5 Hz. Each fire of the igniter caused a spike in the current proportional to the intensity of the UV emission from the flame, and an example of this response is shown in Fig. 5.10. We note that in these experiments, the photodetector is at room temperature due to the short duration of the fire and the large spatial separation from the plume.

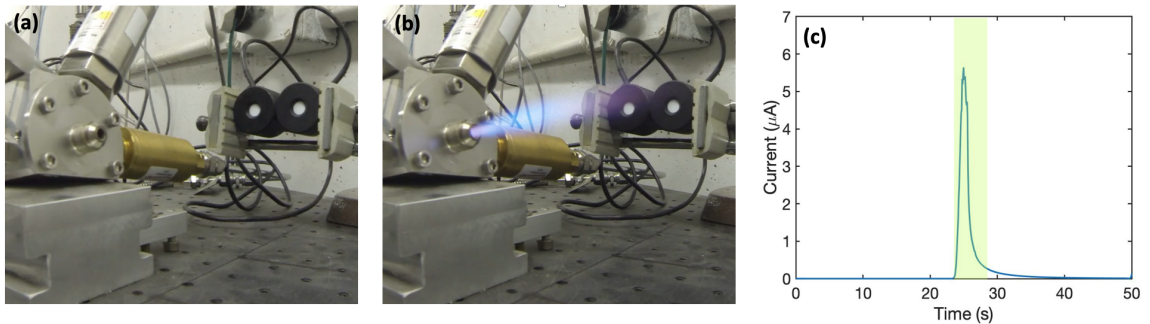


Figure 5.11: Images of (a) the igniter before the burn, (b) the igniter plume during the burn, and (c) the data from the photodetector throughout the course of the burn. © 2019 IEEE.

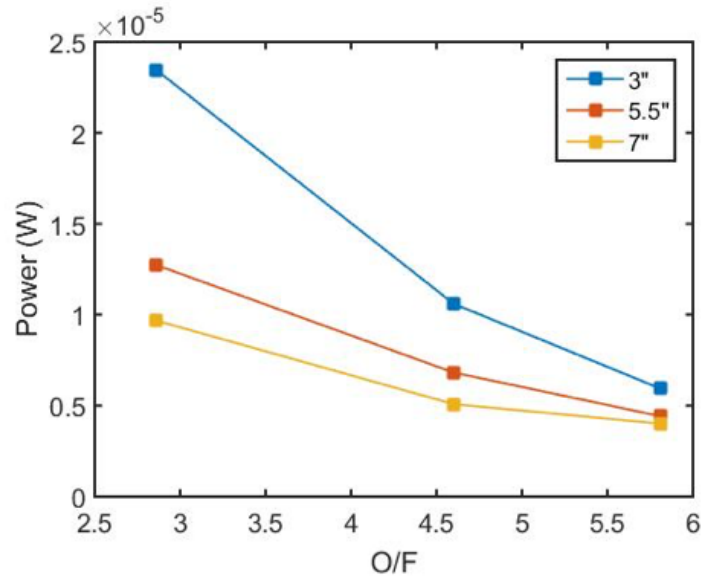


Figure 5.12: Plot of incident optical power versus O/F ratio, showing a trend of increasing optical power with increasing fuel concentration, and decreasing optical power with larger separation between photodetector and plume. © 2019 IEEE.

Combustion Monitoring Results

Images of the igniter before and during the burn, as well as the actual data from the photodetector throughout the course of the burn, are shown in Fig. 5.11. For the matrix of O/F ratios and distances of the photodetector from the plume, we converted the current into incident optical power using the calibration data in Figure 5.3b. The data from the photodetector demonstrates a clear trend of increasing optical power with increasing fuel concentration, as seen in Fig. 5.12. Further, the optical power decreases with larger separation between the photodetector and plume, since a smaller fraction of the UV radiation is incident on the photodetector.

Flame Temperature Calculation

The relationship between temperature and blackbody emissive power was used to estimate an average flame temperature, and a radiative configuration factor corresponding to the geometry of the emitter and the detector was incorporated to improve the model. In the model for radiative heat transfer between the plume and the photodetector, we assume that the plume and the photodetector can be approximated by a cylinder and rectangle (of size $200 \mu\text{m}$ by $280 \mu\text{m}$), respectively. The normal to the rectangle passes through one end of the cylinder and is perpendicular to its axis, with dimensions as shown in Figure 5.9b.

The intensity (i) of light at a given wavelength (λ) is a function of the temperature (T) of the

emitter. It is defined as the radiation emitted by a blackbody at temperature T per unit time, per unit surface area, per unit wavelength, with units of $\text{W}/\text{m}^2 \cdot \mu\text{m}$:

$$i(\lambda, T) = \frac{2C_1}{\lambda^5 (e^{\frac{C_2}{\lambda T}} - 1)}. \quad (5.4)$$

The constants C_1 and C_2 are defined as hc^2 and hc/k_B respectively, where h is Planck's constant, c is the speed of light, and k_B is the Boltzmann constant. The total intensity from a specific band of the electromagnetic spectrum can be calculated by integrating over the wavelengths of interest. In this case, the responsivity of the photodetector is a rectangular window centered around 362 nm (since it is at room temperature) with a width of 16 nm. Thus the power (P) incident on the photodetector, accounting for its spectral response, is given by:

$$P = \pi \times i(T) \times A_1 \quad (5.5)$$

where A_1 is the surface area of the emitter. A configuration factor is introduced to account for the effects of the geometry and orientation of the emitter and the detector. The configuration factor F_{ij} is the fraction of the radiation leaving the surface of the emitter (with surface area A_i) and striking the surface of the detector (with area A_j). The reciprocity relation for configuration factors states that $A_i F_{ij} = A_j F_{ji}$ [159]. The configuration factor for a square emitter and cylindrical detector is given in [21]; the reciprocity relation must then be used to attain the configuration factor for the cylindrical emitter (with surface area A_1) and square detector (with area A_2), resulting in the following:

$$F_{12} = \frac{A_2}{A_1} \times \left[\frac{1}{\pi H} \tan^{-1} \frac{L}{\sqrt{H^2 - 1}} + \frac{L}{H} \left(\frac{X - 2H}{H\sqrt{XY}} \right) \tan^{-1} \sqrt{\frac{X(H-1)}{Y(H+1)}} - \frac{1}{H} \tan^{-1} \sqrt{\frac{H-1}{H+1}} \right] \quad (5.6)$$

where L , H , X , and Y depend on l , r , and d from Fig. 5.9b:

$$L = \frac{l}{r} \quad (5.7)$$

$$H = \frac{d}{r} \quad (5.8)$$

$$X = (1 + H)^2 + L^2 \quad (5.9)$$

$$Y = (1 - H)^2 + L^2 \quad (5.10)$$

In this case, the area of the detector A_2 is $280 \mu\text{m} \times 200 \mu\text{m}$, and the surface area of the flame ($2\pi r l$) varies with O/F ratio, increasing as the combustion reaction increased in fuel content. Multiplying Eq. 5.5 by the configuration factor F_{12} (Eq. 5.6) results in the power emitted by the plume and detected by the photodetector.

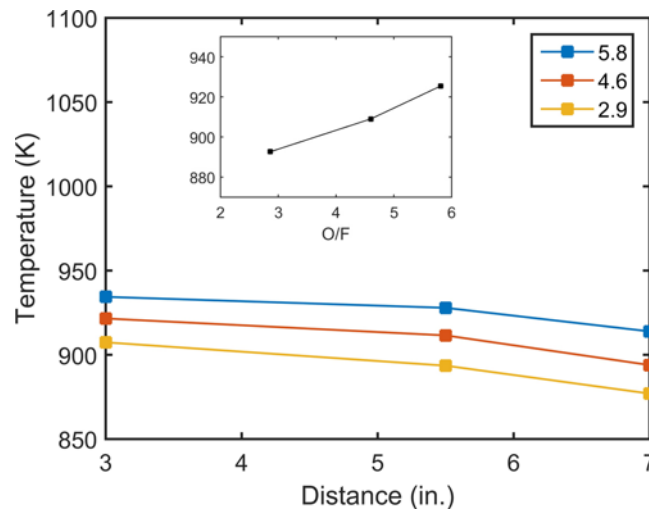


Figure 5.13: Plot of calculated average plume temperature vs. distance of the photodetector from the plume for the three O/F ratios. The inset shows that the average calculated plume temperature for each O/F ratio was between 880 K and 940 K. © 2019 IEEE.

Flame Temperature Results

The temperature was calculated to be roughly invariant (within 25 K) for each fixed fuel concentration for the three tested distances (Fig. 5.13). The theoretical nozzle temperatures for the test conditions are shown in Figure 11, with the two chamber pressures corresponding to the maximum and minimum seen in the experimental tests. The nozzle throat temperature varies by less than 100 K between the three O/F ratios, which was also seen in the calculated temperatures (inset of Fig. 5.13). As seen in Fig. 5.14, the nozzle temperatures are significantly higher than the calculated temperatures (from the photodetector). This is because the flame cools as it expands into the atmosphere, and the calculated temperatures are averages over the entire plume. Additionally, there is significant heat loss to the stainless steel igniter chamber itself, further reducing the temperature below the adiabatic flame temperature.

Measurement Uncertainty

The estimated plume temperatures contain considerable uncertainty. Several sources of uncertainty are described here.

1. The flame surface area, upon which the temperature estimation is highly dependent, was challenging to quantify accurately. In particular, the flame was barely visible in the lean condition. This source of uncertainty could be eliminated in future experiments by collimating the light to provide a known area.
2. Related to (1), the surface area of the flame based on visible light was likely quite different

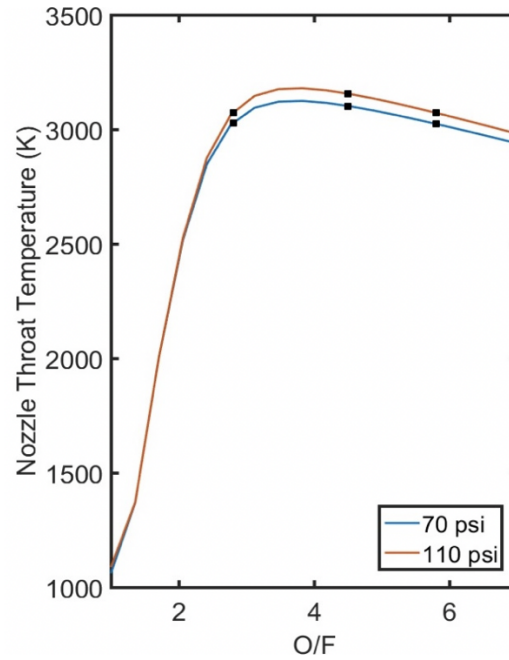


Figure 5.14: Plot of theoretical nozzle temperatures over a range of O/F ratios for two different chamber pressures calculated using CEA. © 2019 IEEE.

than that for UV light. Given that the photodetector had a response to the invisible flames in the lean O/F ratio condition, it is clear that some UV light was still being emitted even though visible light was not.

3. The model assumes that the temperature of the flame is uniform, but the temperature actually varies significantly throughout the plume [160].
4. The calculation of temperature ultimately relies on accurately knowing the incident optical power on the photodetector. This is determined by matching the output current to the calibration curve presented in Fig. 5.3b. While the low power part of the calibration curve is linear and the high power part of the calibration curve is linear, there is a range of power ($\sim 2 \mu\text{W}$ to $\sim 62 \mu\text{W}$) for which the relationship with current is unknown. Many of the measurements from the igniter plume fell within this uncertain region. This uncertainty could be eliminated with a more thorough calibration curve that includes several data points in the region of interest.

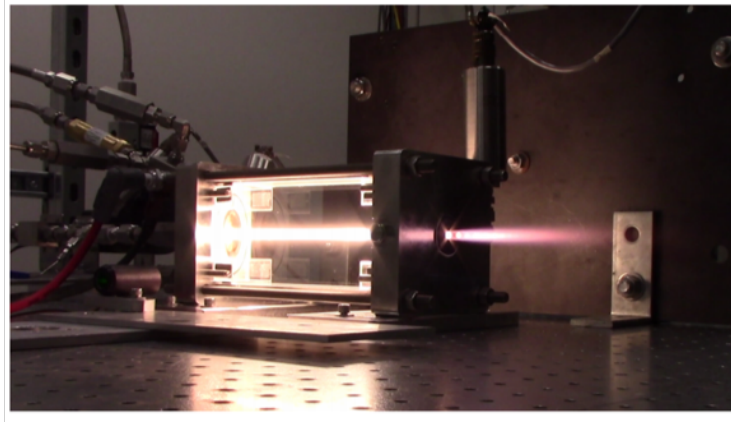


Figure 5.15: Photograph of combustion reaction taking place in hybrid rocket motor fuel grain (image from F.S. Mechantel et al., *AIAA 2018 Propulsion and Energy Forum*, (2018)).

5.4.2 Hybrid Rocket Motor Fuel Grain

Experimental Methods

A subsequent study was done on a hybrid rocket motor fuel grain in Prof. Brian Cantwell's lab at Stanford. Details about the fuel grain are described in [161] and [162] and an image of the operational motor is shown in Fig. 5.15. Two photodetectors were adhered on the outside of the transparent solid fuel grain made of polymethylmethacrylate (PMMA), with one placed towards the fore end and the other towards the aft end. The same experiment was repeated four times: three tests were conducted with the AlGaIn/GaN photodetectors described in the previous sections, while one was done with commercial photodetectors purchased from OSI Optoelectronics. Holders, shown in Fig. 5.16, were 3D-printed to keep the photodetectors securely in place and correctly aligned with the cylindrical port in the center of the fuel grain. During each test, gaseous oxygen was flowed through the central port, causing a combustion reaction with the PMMA fuel grain. The total burn time for each test was ~ 30 seconds. Images of the hybrid rocket motor fuel grain before and during the burn are shown in Fig. 5.17.

Flame Temperature Estimation with Commercial Photodetectors

The sensors purchased from OSI Optoelectronics were silicon Dual Sandwich or Two Color Detectors. Each sensor contains two photodetectors that have responsivity curves that cover different frequency ranges and peak at different wavelengths [163]. The top photodetector responds to light with wavelengths ranging from ~ 400 nm to over 1100 nm and has a peak responsivity of 0.48 A/W at a wavelength of ~ 963 nm. The bottom photodetector has a narrower range; it only responds to light with wavelengths above ~ 930 nm and has a peak responsivity of 0.14 A/W at a wavelength of



Figure 5.16: Image of 3D-printed holders that kept the AlGaIn/GaN (top) and commercial (bottom) photodetectors in place on the fuel grain.

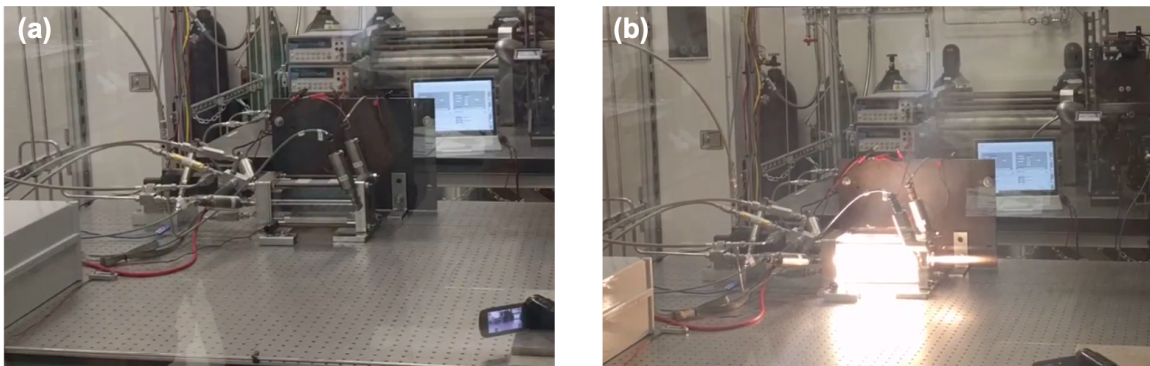


Figure 5.17: Images of the hybrid rocket motor fuel grain before and during the burn.

~ 1057 nm. These Two Color detectors are often used to measure temperature by taking the ratio of radiation intensities of two adjacent wavelengths and comparing them with the standard black body radiation curves.

To estimate the temperature of the flame, we used the following equation:

$$I = \int i(\lambda, T) R(\lambda) d\lambda \int d\Omega \quad (5.11)$$

where I is the output current, $i(\lambda, T)$ is the intensity of light at a given wavelength and temperature taken from Eq. 5.4.1, $R(\lambda)$ comes from the responsivity curve, and Ω is the solid angle, which quantifies that field of view from the photodetector to the flame. Because both photodetectors in the OSI sensor are the same size and in nearly the same place, the solid angles of the two are equal to one another. Setting the solid angles equal results in the equation:

$$\frac{I_1}{\int i_1(\lambda, T) R_1(\lambda) d\lambda} = \frac{I_2}{\int i_2(\lambda, T) R_2(\lambda) d\lambda}. \quad (5.12)$$

The only unknown in the above equation is temperature (T); it can be solved for analytically. Fig. 5.18 shows the responses of the top and bottom photodetectors in two OSI sensors, placed near the fore end and the aft end of the fuel grain. In both locations, the top photodetector has a peak output of ~ 8 mA while the bottom photodetector peaks at ~ 1.7 mA. These measurements resulted in temperature estimates of 1215 K from the sensor on the fore end and 1197 K for the sensor on the aft end. These measurements differ by less than 1.5% and result in an average temperature measurement of 1206 K.

AlGaIn/GaN Photodetector Results

As expected, the current from the AlGaIn/GaN photodetectors increased dramatically over the course of the burn. An example of the current output from a photodetector for one burn is shown in Fig. 5.19a. The current spiked over the ~ 20 seconds of the burn and then returned to close to zero when the burn finished. The peak current (in this case ~ 6 nA) was matched up to the calibration curve to determine the incident optical power that was shining on the photodetector. The same process described in Eqs. 5.6-5.10 was implemented and the temperatures were calculated to be between 1000 and 1013 K.

Many of the same sources of uncertainty listed in the previous section remained during this experiment, but there were a few differences. In this case, the area of the flame was well-constrained because the dimensions of the fuel grain were known. An added source of uncertainty, however, is that there was some material (PMMA) between the flame and the photodetector, which could have blocked some of the UV light from reaching the device.

Despite the uncertainty, the flame temperatures measured are not unreasonable, based on a literature survey. In a 2008 study, Beaulieu and Dembsey used an infrared pyrometer to measure

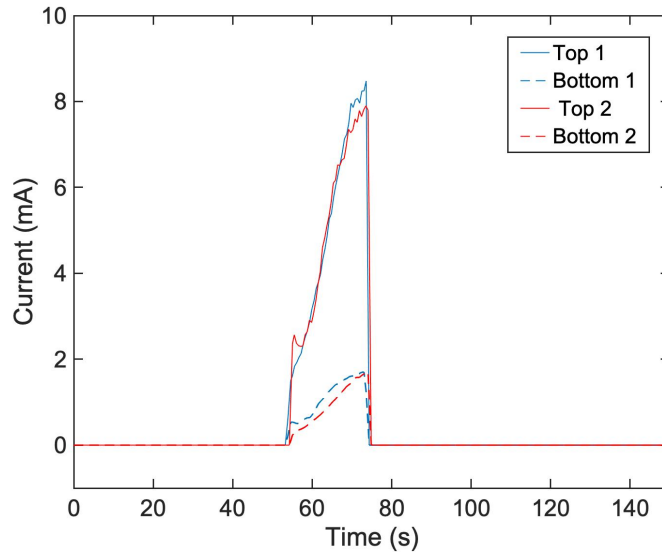


Figure 5.18: Current output from top and bottom photodetectors in OSI sensors over the course of the hybrid rocket motor burn, placed near the fore end (1) and the aft end (2) of the fuel grain.

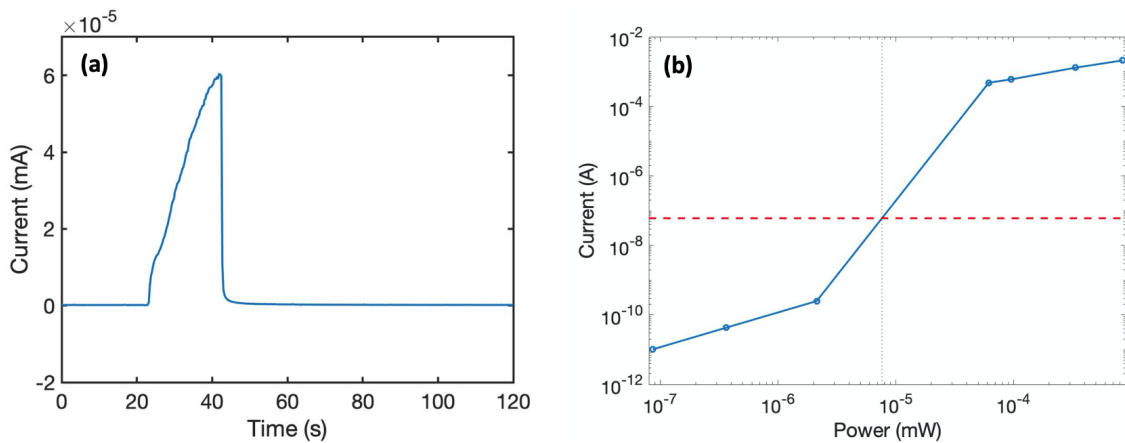


Figure 5.19: (a) Current output from an AlGaIn/GaN photodetector over the course of the hybrid rocket motor burn. (b) Output current (red dashed line) overlaid on top of calibration data (also shown in Fig. 5.3b).

the flame temperature immediately above a sample of burning black PMMA with 20.9% and 40% oxygen concentration. They report a flame temperature of 1184 ± 100 K and 1300 ± 100 K for the two cases respectively [164]. This measurement is lower than that reported in earlier papers; a 1981 study found the temperature of a PMMA flame burning in air to be 1200-1400 K using a “two-sensor, dual-beam, narrow-angle radiometer” in which the flame radiance was measured against a background of blackbody radiation [165]. A paper from 1977 measured the temperature of a PMMA flame to be 1367 K [166], while another paper from the same year states that the PMMA flame temperature is 1420 ± 100 K, with the uncertainty arising due to the unsteady nature of flames [167]. In a more recent paper, Kacem et al. (2016) placed four chromel/alumel thermocouples at different heights in the flame above a burning slab of clear PMMA. They measured the flame temperature to be ~ 1200 K right above the slab, which naturally decreased as the thermocouples were placed further from the surface of the PMMA [168]. Finally, in 2017, Alibert et al. measured the flame temperature close to the burning PMMA surface to be 1087 ± 20 K in an environment with 21% oxygen concentration. As the oxygen concentration decreased, the flame temperature also decreased, down to ~ 1025 K with 18% oxygen concentration [169].

5.5 Conclusions

In this chapter, we examined the performance of a novel AlGaIn/GaN photodetector at high temperature and discussed why its responsivity decreased so significantly up at 250°C . We then implemented it onto two different hybrid rocket motor systems to monitor combustion and estimate flame temperature. While the unknown flame surface area led to significant uncertainty in calculating the temperature of the hybrid rocket igniter plume at JPL, the photodetector measurements were able to shed light on the oxygen-to-fuel ratio of the plume. The temperature estimation of the combustion flame in the transparent PMMA hybrid rocket motor fuel grain was better constrained, but still suffered from uncertainty in the calibration curve. However, the photodetector’s performance at high temperature and its flame detection ability make it a good candidate for use in combustion monitoring applications.

Chapter 6

Concluding Remarks and Future Work

6.1 Conclusions

In this thesis, we investigated the performance of 2DEG-based magnetic field and UV light detectors in space-simulant environments. The results from extensive characterization of these two types of devices suggests that sensors made with GaN heterostructures may be considered for use in outer space and other terrestrial high temperature applications.

In Chapter 3, we conducted a thorough study of how the shape factor (related to the length of Ohmic contacts) of the Hall-effect sensor impacts its sensitivity and noise performance. While the behavior trends been proposed in the literature for silicon Hall-effect plates years ago, this experimental study confirmed that the theory was correct, not only for silicon Hall-effect sensors but for 2DEG-based devices as well. The experimental results showed that the sensitivity behavior followed the shape factor theory quite precisely; the devices with the smallest contacts produced the highest current-scaled sensitivity and the devices shaped as regular octagons resulted in the highest voltage-scaled sensitivity. The shape factor theory only accounts for thermal noise in evaluating the SNR of the devices, but we additionally measured flicker noise to analyze the noise behavior. We determined that larger contacts lead to a higher corner frequency and Hooge parameter, thus suggesting that devices with smaller contacts will have better noise behavior at low frequency operation. At higher frequency operation the flicker noise will be below the thermal noise floor, and then the devices with long contacts are ideal under voltage bias, while those with short contacts are better under current bias.

In Chapter 4, we covered a variety of extreme environment tests conducted on the Hall-effect

sensors. We characterized the voltage-scaled and current-scaled sensitivity between room temperature and 576°C, showing that the devices were functional at this high temperature and exhibited very little hysteresis over 2-3 thermal cycles. This result, combined with preliminary results from the reliability testing being performed on the InAlN/GaN devices, showed the potential for long-term survival in high temperature environments. We additionally showed that the InAlN/GaN Hall-effect sensors had only minor changes in sensitivity after a 10-day exposure to a Venus-analogue environment (460°C, 96.5 bar, CO₂ atmosphere), and that they survived 52 days in low Earth orbit. These results indicate that AlGaN/GaN and InAlN/GaN are promising material platforms for electronics that need to operate in harsh conditions; demonstrating them in these environments raises their technology readiness level as they inch closer to commercialization.

Finally, in Chapter 5, we characterized the behavior of an AlGaN/GaN photodetector at high temperature and analyzed its performance during two different combustion monitoring experiments. We found that the responsivity and NPDR of the photodetector dropped dramatically at 250°C, likely due to the increased hole-electron pair recombination rate. This leads to a reduction in hole accumulation behind the AlGaN barrier; the energetic barrier is thus not lowered enough for many electrons from the 2DEG quantum well to spill out and flow as photocurrent. Despite the worse performance at high temperature, the sensitivity and NPDR proved to be on par with MSM photodetectors in literature operating at room temperature, and thus are still quite functional. We showed that the photodetector was able to monitor the combustion from a hybrid rocket motor igniter plume and in a transparent hybrid rocket motor fuel grain, indicating its potential for use in this application space.

6.2 Ongoing and Future Work

6.2.1 Implementation of Hall-Effect Sensors for Power Applications

The next step towards commercialization of the GaN-based Hall-effect sensors is demonstrating their functionality in industrial applications.

Bucket Transformer

While there is ongoing work to implement the sensors into various power electronics and industrial testbeds, the most successful project was conducted by Janowitz et al. in 2020, described in more detail in [170]. In this project, an InAlN/GaN Hall-effect sensor was implemented into a bucket transformer in Mexico in collaboration with Prolec GE. The sensor was first comprehensively characterized in several industry-relevant conditions, including a temperatures up to 140°C, operating range up to 300 mT with 0.1 mT resolution, survival after exposure to a 2.5 T flux density, and functionality while submerged in mineral oil. The sensor was integrated with an analog-to-digital

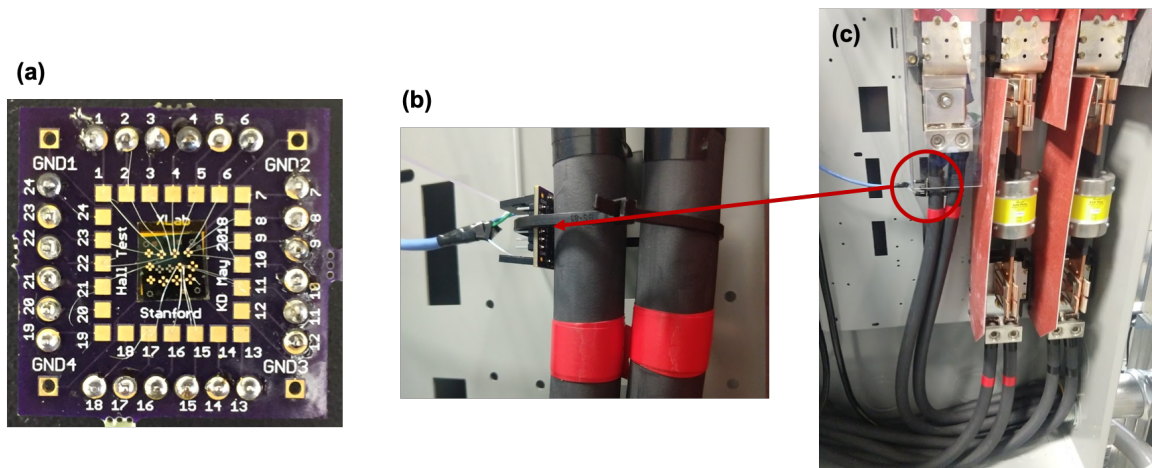


Figure 6.1: (a) Image of InAlN/GaN Hall-effect sensor wirebonded to PCB. (b) and (c) Images of placement of sensor in the power electronics testbed at the University of Illinois Urbana-Champaign for current monitoring of the DC link between a rectifier and inverter.

converter (ADC), micro-controller, memory card, and battery. Data was successfully collected from multiple AC field tests on a dry transformer core and from a DC field test in mineral oil. Further improvements to make this technology more usable in industry include wireless data transfer and renewable power sources.

Other Power Electronics Applications

Work has also been done to integrate the InAlN/GaN Hall-effect sensors into a power electronics testbed at the University of Illinois Urbana-Champaign for current monitoring. The purpose is to demonstrate their use for measuring current into a motor as well as into a DC link between a rectifier and inverter. An image of the sensor placement for current monitoring of the DC link is shown in Fig. 6.1.

Two other projects are also underway: one to monitor current in an electric drive traction system with the University of Arkansas (with Prof. Juan Balda and Prof. Yue Zhao) [171], and the other to monitor the position and speed of a mega-Watt scale electric motor at the University of Illinois (with Prof. Kiruba Haran) [172]. Successful demonstration of current monitoring on these testbeds is necessary before they can be adopted for condition-based monitoring and diagnostics of critical electro-thermal components in industrial systems.

6.2.2 Reliability and Accelerated Aging Testing

As discussed in Chapter 4, long-term high temperature storage tests are being conducted to evaluate the reliability of the InAlN/GaN Hall-effect sensors. Storage at 200°C, 350°C, 450°C, and 600°C is

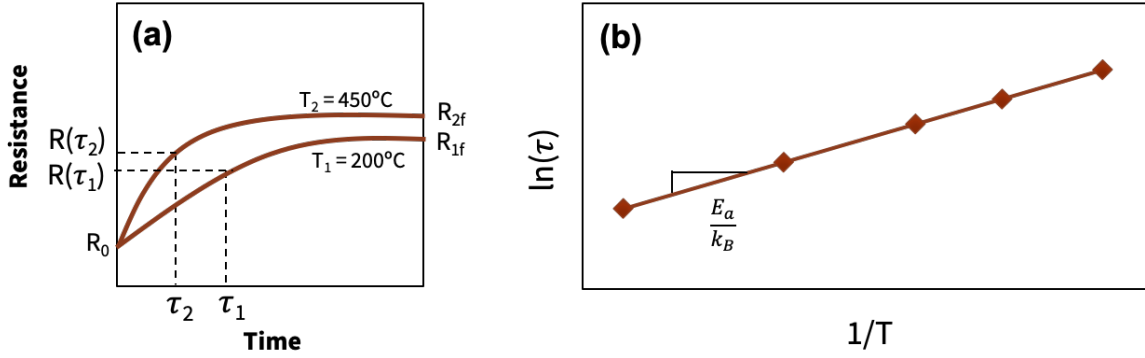


Figure 6.2: Depiction of how Arrhenius model is used in calculating activation energy required for device failure.

being done for up to 1200 hours (at the lower temperatures). Once these tests are complete, the goal is to use an Arrhenius model to determine the activation energy (E_a) that results in device failure. The equation to calculate activation energy is

$$\frac{\tau_2}{\tau_1} = e^{-\frac{E_a}{k_B} \left(\frac{1}{T_1} - \frac{1}{T_2} \right)} \rightarrow E_a = k_B \frac{\ln\left(\frac{\tau_2}{\tau_1}\right)}{\left(\frac{1}{T_2} - \frac{1}{T_1}\right)}. \quad (6.1)$$

The time constants τ_1 and τ_2 are defined as the time it takes for the resistance across the device to reach 67% of its final resistance when exposed to temperatures T_1 and T_2 respectively, as depicted in Fig. 6.2a. After determining the time to failure (τ) at many different temperatures, the natural log of τ can be plotted against the inverse temperature (Fig. 6.2b). The slope of the resulting line is E_a/k_B [173]. These calculated activation energy values may be matched to degradation modes in the literature to shed light on how these sensors fail.

There are also other environmental conditions that may affect the reliability of Hall-effect sensors in industry. These include dynamic magnetic fields, rapid thermal cycling, and humidity exposure. Further testing must be done under all of these conditions to understand the limits of these sensors. Additionally, packaging plays an important role in device reliability, both in protecting it from external conditions and also creating additional potential failure modes or sources of stress. A comprehensive investigation into reliable packaging of these Hall-effect sensors should be conducted.

6.2.3 High Mobility Materials

Ongoing work is being done on fabricating Hall-effect sensors on an AlGaAs/GaAs platform because its high electron mobility of $\sim 5000\text{-}8000 \text{ cm}^2/\text{V}\cdot\text{s}$ at room temperature has proven to result in high sensitivity and low noise devices [174, 175, 50]. While it is known that the narrow bandgap of GaAs results in less temperature stability than GaN, further work may be done to fully characterize its

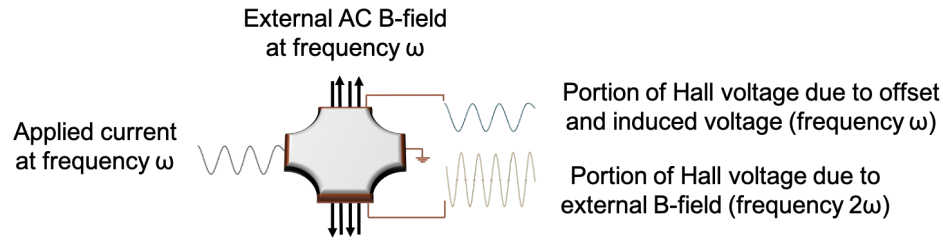


Figure 6.3: Schematic showing operational principles of the 2ω technique.

high temperature behavior. Additionally, a comprehensive study on offset in AlGaAs/GaAs devices would be beneficial, and could inform its use in some applications, such as in the automotive sector.

6.2.4 Novel Methods to Measure AC Magnetic Fields

Because many industrial applications require accurate measurement of AC magnetic fields (e.g., motors, transformers), some recent work has focused on improved methods to measure such fields. In particular, Lalwani et al. (2020) describe a technique, called the “2-omega” method, in which the applied current is supplied at the same frequency as the external magnetic field (ω) [176]. In this case, the output voltage contains three terms: the portion of the signal proportional to the offset is at frequency ω , the portion proportional to the induced voltage (due to Faraday’s law of induction) is at frequency ω , and the portion of interest proportional to the external magnetic field (the true Hall voltage) is at frequency 2ω . Thus, by only measuring the part of the signal at frequency 2ω , the induced voltage and offset terms can be eliminated. A schematic showing the operational principles of this technique is shown in Fig. 6.3. An advantage of this method is that it eliminates much of the offset without needing to implement the current spinning technique. However, further work needs to be done to determine the set of auxiliary components that would be most beneficial for commercial implementation of this method. Additionally, it would be useful to understand the limits of this technique in high temperature environments.

6.2.5 Spinning Frequency

The current spinning technique to reduce offset from the Hall-effect sensor was described in Chapter 2. However, throughout this thesis, the frequency at which the current could be spun was quite limited (on the order of 1 Hz) due to the use of a mechanical switching matrix. There is an open question of whether the rate of current spinning may affect the offset measurement from the sensor. Using an electronic, rather than mechanical, switches could greatly increase the current spinning rate and enable this type of study.

6.2.6 Final Remarks

This thesis illustrates how Hall-effect and ultraviolet light sensors were developed, characterized, and tested under harsh conditions to increase the technology readiness level of GaN-based sensors. Because of its capacity for high power density and ability to operate in extreme environments, GaN-based sensors have the potential to contribute to improving the efficiency of electrified vehicles, miniaturizing wearable and other internet-of-things devices, and allowing us to explore deeper into outer space. As we continue to push the technology forward, we come ever closer to the widespread use of GaN in these and other high power density and harsh environment applications.

Bibliography

- [1] R. Kumar. Sensor market by type, technology, and end user: Global opportunity analysis and industry forecast, 2017 - 2025. Technical report, Allied Market Research, 2019.
- [2] S. Rajaram. Global markets for automotive sensor technologies. Technical report, BCC Research, 2019.
- [3] N. Tyler. Demand for automotive sensors is booming. <http://www.newelectronics.co.uk/electronics-technology/automotive-sensors-market-is-booming/149323/>, Dec. 2016.
- [4] S. Theo. Sensors for the automotive industry. <https://electronicsforu.com/technology-trends/tech-focus/automobile-industry-sensor>, Nov. 2018.
- [5] M. Kraft and N. M. White. *MEMS for Automotive and Aerospace Applications*. Woodhead, Oxford, 2013.
- [6] T. S. Balint, J. A. Cutts, E. A. Kolawa, and C. E. Peterson. Extreme environment technologies for space and terrestrial applications. Technical report, Jet Propulsion Laboratory, California Inst. of Tech., 2008.
- [7] T. George, K. A. Son, R. A. Powers, L. Y. Del Castillo, and R. Okojie. Harsh environment microtechnologies for NASA and terrestrial applications. In *Proc. of IEEE SENSORS Conf.*, 2005.
- [8] A. T. Basilevsky and J. W. Head. The surface of venus. *Rep. Prog. Phys.*, 66:1699–1734, 2003.
- [9] M. P. Petkov. The effects of space environments on electronic components. Technical report, Jet Propulsion Laboratory, California Inst. of Tech., 2003.
- [10] K. P. Hand, C. F. Chyba, J. C. Priscu, R. W. Carlson, and K. H. Nealson. *Astrobiology and the Potential for Life on Europa*. U. Of Arizona Press, Tuscon, 2009.
- [11] Venus technology plan. Technical report, NASA, May 2014.

- [12] S. Duzellier. Radiation effects on electronic devices in space. *Aerospace Sci. and Tech.*, 9:93–99, 2005.
- [13] J. W. Howard and D. M. Hardage. Spacecraft environments interactions: Space radiation and its effects on electronic systems. Technical report, NASA Marshall Space Flight Center, July 1999.
- [14] M. Ohadi and J. Qi. Thermal management of harsh-environment electronics. In *Proc. of IEEE SEMI-THERM Symposium*, volume 20, San Jose, USA, 2004.
- [15] H. Lu, P. Sandvik, A. Vertiatchikh, J. Tucker, and A. Elasser. High temperature hall effect sensors based on AlGa_N/Ga_N heterojunctions. *J. App. Phys.*, 99:114510–1–114510–4, 2006.
- [16] S. R. Hout and S. Middelhoek. A 400°C silicon hall sensor. *Sensors and Actuators A*, 60:14–22, 1997.
- [17] P. G. Neudeck, R. S. Okojie, and L.-Y. Chen. High-temperature electronics - a role for wide bandgap semiconductors? *Proc. of IEEE*, 90(6), 2002.
- [18] H. A. Mantooth, M. D. Glover, and P. Shepherd. Wide bandgap technologies and their implications on miniaturizing power electronic systems. *IEEE Journal of Emerging and Selected Topics in Power Electronics*, 2(3):374–385, 2014.
- [19] H. Morkoç, S. Strite, G. B. Gao, M. E. Lin, B. Sverdlov, and M. Burns. Large-band-gap sic, iii-v nitride, and ii-vi znse-based semiconductor device technologies. *Journal of Applied Physics*, 76(3):1363–1398, 1994.
- [20] R. Stuck, E. Fogarassy, J.J. Grob, and P. Siffert. Solubility limit of impurities in silicon after laser induced melting. *Appl. Phys.*, 23:15–19, 1980.
- [21] D. Maier, M. Alomari, N. Grandjean, J.-F. Carlin, M.-A. Diforte-Poisson, C. Dua, S. Delage, and E. Kohn. InAlN/GaN HEMTs for operation in the 1000°C regime: A first experiment. *IEEE Electron Dev. Lett.*, 33(7):985–987, 2012.
- [22] A. Abderrahmane, P. J. Ko, H. Okada, S.-I. Sato, T. Ohshima, and A. Sandhu. Proton irradiation enhancement of low-field negative magnetoresistance sensitivity of AlGa_N/Ga_N-based magnetic sensor at cryogenic temperature. *IEEE Electron Dev. Lett.*, 35(11):1130–1132, 2014.
- [23] J. Grant, R. Bates, W. Cunningham, A. Blue, J. Melone, F. McEwan, J. Vaitkus, E. Gaubas, and V. O’Shea. Ga_N as a radiation hard particle detector. *Nuclear Instr. And Methods in Phys. Research Section A*, 576(1):60–65, 2007.

- [24] P. Hazdra and S. Popelka. Radiation resistance of wide-bandgap semiconductor power transistors. *physica status solidi (a)*, 214(4):1600447, 2017.
- [25] A. M. H. Kwan, Y. Guan, X. Liu, and K. Chen. A highly linear integrated temperature sensor on a gan smart power IC platform. *IEEE Trans. on Electron Dev.*, 61(8):2970–2976, 2014.
- [26] O. Ambacher, B. Foutz, J. Smart, J. R. Shealy, N. G. Weimann, K. Chu, M. Murphy, A. J. Sieakowski, W. J. Schaff, L. F. Eastman, R. Dimitrov, and M. Stutzmann. Two dimensional electron gases induced by spontaneous and piezoelectric polarization in undoped and doped AlGa_N/Ga_N heterostructures. *J. of App. Phys.*, 87:334–344, 2000.
- [27] X. G. He, D. G. Zhao, and D. S. Jiang. Formation of two-dimensional electron gas at Al-GaN/GaN heterostructure and the derivation of its sheet density expression. *Chinese Phys. B*, 24(6), 2015.
- [28] O. Ambacher, J. Smart, J. R. Shealy, N. G. Weimann, K. Chu, M. Murphy, W. J. Schaff, L. F. Eastman, R. Dimitrov, L. Wittmer, M. Stutzmann, W. Rieger, and J. Hilsenbeck. Two-dimensional electron gases induced by spontaneous and piezoelectric polarization charges in n- and ga-face algan/gan heterostructures. *Journal of Applied Physics*, 85(6):3222–3233, 1999.
- [29] L. Hsu and W. Walukiewicz. Effect of polarization fields on transport properties in algan/gan heterostructures. *Journal of Applied Physics*, 89(3):1783–1789, 2001.
- [30] J. P. Ibbetson, P. T. Fini, K. D. Ness, S. P. DenBaars, J. S. Speck, and U. K. Mishra. Polarization effects, surface states, and the source of electrons in algan/gan heterostructure field effect transistors. *Applied Physics Letters*, 77(2):250–252, 2000.
- [31] X. He, D. Zhao, W. Liu, J. Yang, X. Li, and X. Li. Effect of gan buffer polarization on electron distribution of algan/gan heterostructure. *Journal of Alloys and Compounds*, 670:258–261, 2016.
- [32] A. Asgari, M. Kalafi, and L. Faraone. The effects of gan capping layer thickness on two-dimensional electron mobility in gan/algan/gan heterostructures. *Physica E: Low-dimensional Systems and Nanostructures*, 25(4):431–437, 2005.
- [33] T. P. White, S. Shetty, M. E. Ware, H. A. Mantooth, and G. J. Salamo. AlGa_N/Ga_N micro-hall effect devices for simultaneous current and temperature measurements from line currents. *IEEE Sensors J.*, 18(7):2944–2951, 2015.
- [34] X. G. He, D. G. Zhao, and D. S. Jiang. AlGa_N/Ga_N HEMTs – an overview of device operation and applications. *Proc. of the IEEE*, 90(6), 2002.

- [35] A. J. Suria, A. S. Yalamarthy, H. So, and D. G. Senesky. DC characteristics of ALD-grown $\text{Al}_2\text{O}_3/\text{AlGaIn}/\text{GaIn}$ MIS-HEMTs and HEMTs at 600°C in air. *Semicond. Sci. Tech.*, 31(11), 2016.
- [36] Y. de Charentenay. Magnetic sensor market and technologies. Technical report, Yole Développement, 2017.
- [37] R. L. Fagaly. Superconducting quantum interference device instruments and applications. *Review of Scientific Instruments*, 77(10):101101, 2006.
- [38] P. Marcon and K. Ostanina. Overview of methods for magnetic susceptibility measurement. 2012.
- [39] J. Lenz and S. Edelstein. Magnetic sensors and their applications. *IEEE Sensors Journal*, 6(3):631–649, 2006.
- [40] T. N. Smekalova, O. Voss, and S. L. Smekalov. *Magnetic Surveying in Archaeology*. Wormianum, St. Petersburg, 2 edition, 2008.
- [41] T. M. Tierney, N. Holmes, S. Mellor, J. D. López, G. Roberts, R. M. Hill, E. Boto, J. Leggett, V. Shah, M. J. Brookes, R. Bowtell, and G. R. Barnes. Optically pumped magnetometers: From quantum origins to multi-channel magnetoencephalography. *NeuroImage*, 199:598–608, 2019.
- [42] Marina Díaz-Michelena. Small magnetic sensors for space applications. *Sensors (Basel, Switzerland)*, 9:2271–2288, 2009.
- [43] G. B. Hospodarsky. Spaced-based search coil magnetometers. *Journal of Geophysical Research: Space Physics*, 121(12):12,068–12,079, 2016.
- [44] W. Y. Due. *Resistive, Capacitive, Inductive, and Magnetic Sensor Technologies*. CRC Press, Boca Raton, 2015.
- [45] B. Dieny. Giant magnetoresistance in spin-valve multilayers. *Journal of Magnetism and Magnetic Materials*, 136(3):335–359, 1994.
- [46] F. Radu and J. Sánchez-Barriga. *Ferrimagnetic Heterostructures for Applications in Magnetic Recording*, pages 267–331. 06 2018.
- [47] H.H. Yang, N.V. Myung, J. Yee, D.-Y. Park, B.-Y. Yoo, M. Schwartz, K. Nobe, and J.W. Judy. Ferromagnetic micromechanical magnetometer. *Sensors and Actuators A: Physical*, 97-98:88–97, 2002. Selected papers from Eurosenors XV.
- [48] E. Ramsden. *Hall Effect Sensors: Theory and Application*. Elsevier, Oxford, UK, 2 edition, 2006.

- [49] A. Krishna S. and L. Abraham. Analysis of different hall effect current sensors for space applications. *International J. of Innovative Sci., Eng., Tech.*, 1(5):380–386, 2014.
- [50] S. Koide, H. Takahashi, A. Abderrahmane, A. I. Shibasaki, and A. Sandhu. High temperature hall sensors using AlGa_xN/GaN HEMT structures. In *J. of Physics: Conf. Ser.*, volume 352, pages 879–888, 2011.
- [51] Dave Drachlis. Advanced space transportation program: Paving the highway to space. <https://www.nasa.gov/centers/marshall/news/background/facts/astp.html>.
- [52] B. K. Ridley, B. E. Foutz, and L. F. Eastman. Mobility of electrons in bulk GaN and Al_xGa_{1-x}N/GaN heterostructures. *Phys. Rev. B, Condens. Matter*, 611(24):16862–16869, 2000.
- [53] U. Auserlechner. The signal-to-noise ratio and a hidden symmetry of hall plates. *Solid-State Electron.*, 135:14–23, 2017.
- [54] G. S. Randhawa. Monolithic integrated hall devices in silicon circuits. *Microelectronics J.*, 12(6):24–29, 1981.
- [55] R. Popović. *Hall Effect Devices*. IOP, UK, 2 edition, 2004.
- [56] U. Auserlechner. Two simple formulate for hall-geometry factor of hall-plates with 90°symmetry. *U.P.B Sci. Bull. Ser. A*, 78(1):275–282, 2016.
- [57] U. Auserlechner. Closed form expressions for sheet resistance and mobility from van-der-pauw measurement on 90°symmetric devices with four arbitrary contacts. *Solid-State Electron.*, 116:46–54, 2016.
- [58] P. J. A. Munter. A low-offset spinning-current Hall plate. *Sensors and Actuators*, A21:743–746, 1990.
- [59] P. Ruther, U. Schiller, R. Janke, and O. Paul. Thermomagnetic residual offset in integrated hall plates. *IEEE Sensors J.*, 3(6):693–699, 2003.
- [60] V. Mosser and N. Matringe. A spinning current circuit for nanotesla range resolution in Hall measurements. In *Proc. IEEE Sensors Appl. Symp. (SAS)*, pages 1–6, Catania, Italy, 2016.
- [61] S. Bellekom and L. Sarro. Offset reduction of Hall plates in three different crystal planes. In *Proc. of the Int. Conf. on Solid-State Sensors, Actuators, and Microsystems*, pages 233–237, 1997.
- [62] K. Dowling. *Offset and Noise Behavior of Microfabricated Aluminum Gallium Nitride-Gallium Nitride Two-Dimensional Electron Gas Hall-Effect Sensors*. PhD thesis, Stanford University, 8 2019.

- [63] K. M. Dowling, T. Liu, H. S. Alpert, C. A. Chapin, S. R. Eisner, A. S. Yalamarthy, P. F. Satterthwaite, H. Köck, U. Ausserlechner, M. Asheghi, K. E. Goodson, and D. G. Senesky. Low offset and noise in high biased gan 2deg hall-effect plates investigated with infrared microscopy. *Journal of Microelectromechanical Systems*, pages 1–8, 2020.
- [64] H. S. Alpert, K. M. Dowling, C. A. Chapin, A. S. Yalamarthy, S. R. Benbrook, H. Köck, U. Ausserlechner, and D. G. Senesky. Effect of geometry on sensitivity and offset of AlGa_N/Ga_N and InAlN/GaN hall-effect sensors. *IEEE Sensors J.*, 19(10):3640–3646, 2019.
- [65] K. M. Dowling, H. S. Alpert, A. S. Yalamarthy, P. F. Satterthwaite, S. Kumar, H. Köck, U. Ausserlechner, and D. G. Senesky. Micro-tesla offset in thermally stable AlGa_N/Ga_N 2DEG hall plates using current spinning. *IEEE Sensors Lett.*, 3(3), 2019.
- [66] J. C. van der Meer, F. R. Riedijk, P. C. de Jong, E. A. van Kampen, M. J. Meekel, and J. H. Huijsing. CMOS quad spinning-current hall sensor system for compass application. In *Proc. Int. Conf. IEEE Sensors*, pages 1434–1437, 2004.
- [67] J. C. van der Meer, F. R. Riedijk, E. van Kampen, K. A. A. Makinwa, and J. H. Huijsing. A fully integrated CMOS hall sensor with a 3.65 μ T 3 σ offset for compass applications. In *Proc. Int. Conf. IEEE Sensors*, pages 246–247, San Francisco, CA, USA, 2005.
- [68] U. Ausserlechner. Hall effect devices with three terminals: Their magnetic sensitivity and offset cancellation scheme. *J. of Sensors*, 2016, 2016.
- [69] C. Sander, C. Leube, T. Aftab, P. Ruther, and O. Paul. Isotropic 3D silicon hall sensor. In *Proc. 28th Int. Conf. IEEE Micro. Electro. Mech. Syst.*, pages 893–896, Estoril, Portugal, 2015.
- [70] L. Bouguen, L. Konczewicz, S. Contreras, B. Jouault, J. Camassel, and Y. Cordier. High temperature behaviour of AlGa_N/Ga_N hall-FET sensors. *Materials Sci. and Eng. B*, 165:1–4, 2009.
- [71] A. Abderrahmane, S. Koide, S.-I. Sato, T. Ohshima, A. Sandhu, and H. Okada. Robust hall effect magnetic field sensors for operation at high temperatures and in harsh radiation environments. *IEEE Trans. on Magnetics*, 48(11):4421–4423, 2012.
- [72] M. J. Wang, B. Shen, F. J. Xu, Y. Wang, J. Xu, S. Huang, Z. J. Yang, K. Xu, and G. Y. Zhang. High temperature dependence of the density of two-dimensional electron gas in Al_{0.18}Ga_{0.82}N/GaN heterostructures. *Appl. Phys. A*, pages 715–718, 2007.
- [73] H. S. Alpert, C. A. Chapin, K. M. Dowling, S. R. Benbrook, H. Köck, U. Ausserlechner, and D. G. Senesky. Sensitivity of 2DEG-based Hall-effect sensors at high temperatures. *Review of Scientific Instruments*, 91(2):025003, 2020.

- [74] V. Mosser, N. Matgringe, and Y. Haddab. A spinning current circuit for Hall measurements down to the nanotesla range. *Transactions on Instr. and Meas.*, 66(4):637–650, 2017.
- [75] V. Cambel, G. Karapetrov, P. Elias, S. Hasenohrl, W.-K. Kwok, J. Krause, and J. Manka. Approaching the pT range with a 2DEG InGaAs/InP Hall sensor at 77 k. *Microelectronic Eng.*, 51-52:333–342, 2000.
- [76] N. Haned and M. Missous. Nano-tesla magnetic field magnetometry using an InGaAs-AlGaAs-GaAs 2DEG Hall sensor. *Sensors and Actuators A, Phys.*, 102(3):216–222, 2003.
- [77] U. Ausserlechner. Limits of offset cancellation by the principle of spinning current hall probe. In *Proc. of IEEE Sensors*, Vienna, Austria, 2004.
- [78] H. Chen, K. Liu, L. Hu, A. A. Al-Ghamdi, and X. Fang. New concept ultraviolet photodetectors. *Materials Today*, 18(7):493–502, 2015.
- [79] E. Monroy, F. Omnes, and F. Calle. Wide-bandgap semiconductor ultraviolet photodetectors. *Semiconductor Sci. Tech.*, 18(4):R33–R51, 2003.
- [80] L. Sang, L. Meiyong, and M. Sumiya. A comprehensive review of semiconductor ultraviolet photodetectors: from thin film to one-dimensional nanostructures. *Sensors*, 13(8):10482–10518, 2013.
- [81] C. Chui, A. Okyay, and K. Saraswat. Effective dark current suppression with asymmetric msm photodetectors in group IV semiconductors. *IEEE Photonics Tech. Lett.*, 15(11):1585–1587, 2003.
- [82] Y. An, A. Behnam, E. Pop, and A. Ural. Metal-semiconductor-metal photodetectors based on graphene/p-type silicon Schottky junctions. *Appl. Phys. Lett.*, 102, 2013.
- [83] P. F. Satterthwaite, A. S. Yalamarthy, N. A. Scandrette, A. K. M. Newaz, and D. G. Senesky. High responsivity, low dark current ultraviolet photodetectors based on two-dimensional electron gas interdigitated transducers. *ACS Photonics*, 5(11):4277–4282, 2018.
- [84] P. R. Berger. MSM photodiodes. *IEEE Potentials*, 15(2):25–29, 1996.
- [85] F. Omnes. *Introduction to Semiconductor Devices*, chapter 1, pages 1–14. Wiley, 2009.
- [86] R. Miller. *Thermal and Radiation Exposure of Graphene-Enhanced Gallium Nitride Ultraviolet Photodetectors for Space Exploration*. PhD thesis, Stanford University, 3 2018.
- [87] H. Ferhati and F. Djefal. Performance assessment of gr/si/gr uv-photodetector: Design and optimization of graphene interdigitated electrodes. *Superlattices and Microstructures*, 132:106166, 2019.

- [88] J. Burm, K. I. Litvin, D. W. Woodard, W. J. Schaff, P. Mandeville, M. A. Jaspan, M. M. Gitin, and L. F. Eastman. High-frequency, high-efficiency msm photodetectors. *IEEE Journal of Quantum Electronics*, 31(8):1504–1509, 1995.
- [89] W. Yang, T. Nohava, S. Krishnankutty, R. Torreano, S. McPherson, and H. Marsh. High gain gan/algan heterojunction phototransistor. *Applied Physics Letters*, 73(7):978–980, 1998.
- [90] M. L. Lee, J. K. Sheu, and Y.-R. Shu. Ultraviolet bandpass $\text{Al}_{0.17}\text{Ga}_{0.83}\text{N}/\text{GaN}$ heterojunction phototransistors with high optical gain and high rejection ratio. *Applied Physics Letters*, 92(5):053506, 2008.
- [91] X. Zhou, M. J. Hobbs, and B. S. White. An InGaAlAs-InGaAs two-color photodetector for ratio thermometry. *IEEE Transaction on Electron Devices*, 61(3):838–843, 2014.
- [92] C. Palmer, A. Royce, and P. Sandvik. Application of silicon carbide photodiode flame temperature sensors in an active combustion pattern factor control system. *J. of Engineering for Gas Turbines and Power*, 133, 2011.
- [93] D. M. Brown, J. B. Fedison, J. R. Hibshman, J. W. Kretchmer, L. Lombardo, K. S. Matocha, and P. M. Sandvik. Silicon carbide photodiode sensor for combustion control. *IEEE Sensors J.*, 5(5):983–988, 2005.
- [94] J. L. Pau, J. Anduaga, C. Rivera, A. Navarro, I. Alava, M. Redondo, and E. Muñoz. Optical sensors based on III-nitride photodetectors for flame sensing and combustion monitoring. *Applied Optics*, 45(28):7498–7503, 2006.
- [95] L. Arias, S. Torres, D. Sbarbaro, and O. Farias. Photodiode-based sensor for flame sensing and combustion-process monitoring. *Appl. Optics*, 47(29):5541–5549, 2008.
- [96] L. Hsu and W. Walukiewicz. Electron mobility in $\text{Al}_x\text{Ga}_{1-x}\text{N}/\text{GaN}$ heterostructures. *Phys. Rev. B*, 56:1520–1528, Jul 1997.
- [97] K.W. Böer and U.W. Pohl. *Semiconductor Physics*. Springer, Cham, 2018.
- [98] S. B. Lisesivdin, A. Yildiz, N. Balkan, M. Kasap, S. Ozcelik, and E. Ozbay. Scattering analysis of two-dimensional electrons in algan/gan with bulk related parameters extracted by simple parallel conduction extraction method. *Journal of Applied Physics*, 108(1):013712, 2010.
- [99] K. Kaasbjerg, K. S. Thygesen, and A.-P. Jauho. Acoustic phonon limited mobility in two-dimensional semiconductors: Deformation potential and piezoelectric scattering in monolayer MoS_2 from first principles. *Phys. Rev. B*, 87:235312, Jun 2013.

- [100] O. Katz, A. Horn, G. Bahir, and J. Salzman. Electron mobility in an algan/gan two-dimensional electron gas. i. carrier concentration dependent mobility. *IEEE Transactions on Electron Devices*, 50(10):2002–2008, 2003.
- [101] I. P. Smorchkova, C. R. Elsass, J. P. Ibbetson, R. Vetury, B. Heying, P. Fini, E. Haus, S. P. DenBaars, J. S. Speck, and U. K. Mishra. Polarization-induced charge and electron mobility in AlGa_N/Ga_N heterostructures grown by plasma-assisted molecular-beam epitaxy. *Journal of Applied Physics*, 86(8):4520–4526, 1999.
- [102] B. Shen, T. Someya, and Y. Arakawa. Influence of strain relaxation of the Al_xGa_{1-x}N barrier on transport properties of the two-dimensional electron gas in modulation-doped Al_xGa_{1-x}N/GaN heterostructures. *Applied Physics Letters*, 76(19):2746–2748, 2000.
- [103] M. Horita and J. Suda. Characterization of lightly-doped n- and p-type homoepitaxial gan on free-standing substrates. In *2017 IEEE International Meeting for Future of Electron Devices, Kansai (IMFEDK)*, pages 86–87, 2017.
- [104] S. Birner. Mobility in two-dimensional electron gases (2DEGs). nextnano.de/nextnano3/tutorial/1Dtutorial_2DEGmobility.htm.
- [105] M. Shur, B. Gelmont, and M. Asif Khan. Electron mobility in two-dimensional electron gas in AlGa_N/Ga_N heterostructures and in bulk Ga_N. *Journal of Electronic Materials*, 25:777–785, 1996.
- [106] N. Maeda, K. Tsubaki, T. Saitoh, and N. Kobayashi. High-temperature electron transport properties in AlGa_N/Ga_N heterostructures. *Applied Physics Letters*, 79(11):1634–1636, 2001.
- [107] J. Kuzmík, G. Pozzovivo, C. Ostermaier, G. Strasser, D. Pogany, E. Gornik, J.-F. Carlin, M. Gonschorek, E. Feltn, and N. Grandjean. Analysis of degradation mechanisms in lattice-matched InAlN/GaN high-electron-mobility transistors. *J. Appl. Phys.*, 106:124503, 2009.
- [108] P. Herfurth, D. Maier, L. Lugani, J. Carlin, R. Rosch, Y. Men, N. Grandjean, and E. Kohn. Ultrathin body InAlN/GaN HEMTs for high-temperature (600 °c) electronics. *IEEE Electron Device Letters*, 34(4):496–498, 2013.
- [109] K. Jeganathan, M. Shimizu, H. Okumura, Y. Yano, and N. Akutsu. Lattice-matched InAlN/GaN two-dimensional electron gas with high mobility and sheet carrier density by plasma-assisted molecular beam epitaxy. *Journal of Crystal Growth*, 304(2):342–345, 2007.
- [110] M. Hiroki, H. Yokoyama, N. Watanabe, and T. Kobayashi. High-quality InAlN/GaN heterostructures grown by metal-organic vapor phase epitaxy. *Superlattices and Microstructures*, 40(4):214–218, 2006. E-MRS 2006 Symposium S: Material Science and Technology of Wide Bandgap Semiconductors.

- [111] J. Xue, Y. Hao, J. Zhang, X. Zhou, Z. Liu, J. Ma, and Z. Lin. Nearly lattice-matched InAlN/GaN high electron mobility transistors grown on SiC substrate by pulsed metal organic chemical vapor deposition. *Applied Physics Letters*, 98(11):113504, 2011.
- [112] J. Xue, J. Zhang, W. Zhang, L. Li, F. Meng, M. Lu, J. Ning, and Y. Hao. Effects of AlN interlayer on the transport properties of nearly lattice-matched InAlN/GaN heterostructures grown on sapphire by pulsed metal organic chemical vapor deposition. *Journal of Crystal Growth*, 343(1):110–114, 2012.
- [113] M. Hou. *Suspended Aluminum Gallium Nitride/Gallium Nitride-on-Silicon Microstructures for High-Temperature-Tolerant Micro-Electromechanical Systems*. PhD thesis, Stanford University, 5 2017.
- [114] D. J. Chen, K. X. Zhang, Y. Q. Tao, X. S. Wu, J. Xu, R. Zhang, Y. D. Zheng, and B. Shen. Temperature-dependent strain relaxation of the AlGaN barrier in AlGaN/GaN heterostructures with and without Si₃N₄ surface passivation. *Appl. Phys. Lett.*, 88(10):102106, 2006.
- [115] Z. Feng, Y. Zhou, S. Cai, and K.-M. Lau. Doping concentration and structural dependences of the thermal stability of the 2DEG in GaN-based high-electron-mobility transistor structures. *Jap. J. Appl. Phys.*, 44(1):L21–L23, 2005.
- [116] Z. H. Feng, Y. G. Zhou, S. J. Cai, and K. M. Lau. Enhanced thermal stability of the two-dimensional electron gas in GaN/AlGaN/GaN heterostructures by Si₃N₄ surface-passivation-induced strain solidification. *Applied Physics Letters*, 85(22):5248–5250, 2004.
- [117] D. Chen, B. Shen, K. Zhang, Y. Tao, X. Wu, J. Xu, R. Zhang, and Y. Zheng. High-temperature characteristics of strain in AlGaN/GaN heterostructures. *Japanese J. Appl. Phys.*, 45(18):18–20, 2006.
- [118] M. Hou, S. R. Jain, H. So, T. A. Houser, X. Xu, A. J. Suria, and D. G. Senesky. Degradation of 2DEG transport properties in GaN-capped AlGaN/GaN heterostructures at 600°C in oxidizing and inert environments. *J. Appl. Phys.*, 122:195102, 2017.
- [119] K. Houjou, K. Ando, S.-P. Liu, and S. Sato. Crack-healing and oxidation behavior of silicon nitride ceramics. *Journal of the European Ceramic Society*, 24(8):2329–2338, 2004.
- [120] G.M. Song, Y.T. Pei, W.G. Sloof, S.B. Li, J.Th.M. [De Hosson], and S. [van der Zwaag]. Oxidation-induced crack healing in ti3alc2 ceramics. *Scripta Materialia*, 58(1):13–16, 2008.
- [121] M. E. Lin, Z. Ma, F. Y. Huang, Z. F. Fan, L. H. Allen, and H. Morkoç. Low resistance ohmic contacts on wide band-gap GaN. *Applied Physics Letters*, 64(8):1003–1005, 1994.

- [122] N Chaturvedi, U Zeimer, J Würfl, and G Tränkle. Mechanism of ohmic contact formation in AlGa_N/Ga_N high electron mobility transistors. *Semiconductor Science and Technology*, 21(2):175–179, jan 2006.
- [123] B. Van Daele, G. Van Tendeloo, W. Ruythooren, J. Derluyn, M. R. Leys, and M. Germain. The role of Al on Ohmic contact formation on n-type Ga_N and AlGa_N/Ga_N. *Applied Physics Letters*, 87(6):061905, 2005.
- [124] Z. Fan, S. N. Mohammad, W. Kim, Ö. Aktas, A. E. Botchkarev, and H. Morkoç. Very low resistance multilayer ohmic contact to n-Ga_N. *Applied Physics Letters*, 68(12):1672–1674, 1996.
- [125] A. Motayed, R. Bathe, M. C. Wood, O. S. Diouf, R. D. Vispute, and S. N. Mohammad. Electrical, thermal, and microstructural characteristics of Ti/Al/Ti/Au multilayer ohmic contacts to n-type Ga_N. *Journal of Applied Physics*, 93(2):1087–1094, 2003.
- [126] M. Hou and D. G. Senesky. Operation of ohmic Ti/Al/Pt/Au multilayer contacts to Ga_N at 600°C in air. *Applied Physics Letters*, 105(8):081905, 2014.
- [127] S. N. Mohammad. Contact mechanisms and design principles for nonalloyed ohmic contacts to n-Ga_N. *Journal of Applied Physics*, 95(9):4856–4865, 2004.
- [128] V. Kumar, L. Zhou, D. Selvanathan, and I. Adesida. Thermally-stable low-resistance Ti/Al/Mo/Au multilayer ohmic contacts on n-Ga_N. *Journal of Applied Physics*, 92(3):1712–1714, 2002.
- [129] C.-T. Lee and H.-W. Kao. Long-term thermal stability of Ti/Al/Pt/Au ohmic contacts to n-type Ga_N. *Applied Physics Letters*, 76(17):2364–2366, 2000.
- [130] C. Wang and N. Kim. Electrical characterization and nanoscale surface morphology of optimized Ti/Al/Ta/Au ohmic contact for AlGa_N/Ga_N HEMT. *Nanoscale Res. Lett.*, 7(107), 2012.
- [131] A.N. Bright, D.M. Tricker, C.J. Humphreys, and R. Davies. A transmission electron microscopy study of microstructure evolution with increasing anneal temperature in Ti/Al ohmic contacts to n-Ga_N. *J. of Elec. Mater.*, 30:L13–L16, 2001.
- [132] D. Selvanathan, L. Zhou, V. Kumar, I. Adesida, and N. Finnegan. Long-term thermal stability of Ti/Al/Mo/Au ohmic contacts on n-Ga_N. *J. of Elec. Mater.*, 32:335–340, 2003.
- [133] M. Piazza, C. Dua, M. Oualli, E. Morvan, D. Carisetti, and F. Wyczisk. Degradation of TiAlNiAu as ohmic contact metal for Ga_N HEMTs. *Microelectronics Reliability*, 49(9):1222–1225, 2009.

- [134] J. Lienig and M. Thiele. *Fundamentals of Electromigration-Aware Integrated Circuit Design*. Springer International, 2018.
- [135] J. Kuzmík, D. Pogany, E. Gornik, P. Javorka, and P. Kordoš. Electrical overstress in AlGa_N/Ga_N HEMTs: study of degradation processes. *Solid-State Electronics*, 48(2):271–276, 2004.
- [136] R. Dietrich, A. Wieszt, A. Vescan, H. Leier, R. Stenzel, and W. Klix. Power handling limits and degradation of large area AlGa_N/Ga_N RF-HEMTs. *Solid-State Electronics*, 47(1):123–125, 2003.
- [137] D. Maier, M. Alomari, N. Grandjean, J. Carlin, M. Diforte-Poisson, C. Dua, A. Chuvilin, D. Troadec, C. Gaquière, U. Kaiser, S. Delage, and E. Kohn. Above 500°C operation of InAlN/GaN HEMTs. In *2009 Device Research Conference*, pages 285–286, 2009.
- [138] W. Versnel. Analysis of symmetrical Hall plates with finite contacts. *J. of Appl. Phys.*, 52:4659–4666, 1981.
- [139] K. K. Hung, P. K. Ko, C. Hu, and Y. C. Cheng. A unified model for the flicker noise in metal-oxide-semiconductor field-effect transistors. *IEEE Trans. Electron Dev.*, 37(3):654–665, 1990.
- [140] F. N. Hooge, T. G. M. Kleinpenning, and L. K. J. Vandamme. Experiment studies on 1/f noise. *Rep. Prog. Phys.*, 44:480–532, 1981.
- [141] K. Lundberg. Survey of noise sources in bulk CMOS. online, 2002.
- [142] M. Tacano, M. Ando, I. Shibusaki, S. Hashiguchi, J. Sikula, and T. Matsui. Dependence of Hooge parameter of InAs heterostructure on temperature. *Microelectronics Reliability*, 40(11):1921–1924, 2000.
- [143] J. Lee, I. Han, B.-Y. Yu, G.-C. Yi, and G. Ghibaudo. Physical understanding of the hooge parameter in ZnO nanowire devices. *J. Korean Phy. Soc.*, 53:339–342, 2008.
- [144] K. M. Dowling, H. S. Alpert, P. Zhang, A. N. Ramirez, A. S. Yalamarthy, H. Köck, U. Ausserlechner, and D. G. Senesky. The effect of bias conditions on AlGa_N/Ga_N 2DEG Hall plates. In *Proc. of Solid State Sensors, Actuators, and Microsystems Workshop*, Hilton Head, SC, 2018.
- [145] A. Aminbeidokhti, S. Dimitrijević, J. Han, X. Chen, and X. Xu. The power law of phonon-limited electron mobility in the 2-D electron gas of AlGa_N/Ga_N heterostructure. *IEEE Trans. Electron. Dev.*, 63(5):2214–2218, 2016.

- [146] T. T. Mnatsakanov, M. E. Levinshtein, L. I. Pomortseva, S. N. Yurkov, G. S. Simin, and M. A. Khan. Carrier mobility model for GaN. *Solid-State Electron.*, 47:111–115, 2003.
- [147] U. Ausserlechner, M. Motz, and M. Holliber. Drift of magnetic sensitivity of smart Hall sensors due to moisture absorbed by the IC-package [automotive applications]. In *SENSORS*, pages 455–458, Vienna, Austria, 2004.
- [148] G. Zeng, N. Tansu, and B. A. Krick. Moisture dependent wear mechanisms of gallium nitride. *Tribology International*, 118:120–127, 2018.
- [149] Z. Manchester, M. Peck, and A. Filo. Kicksat: A crowd-funded mission to demonstrate the world’s smallest spacecraft. In *2013 Small Satellite Conference*, 2013.
- [150] M. Holliday, A. Ramirez, C. Settle, T. Tatum, D. Senesky, and Z. Manchester. Pycubed: An open-source, radiation-tested cubesat platform programmable entirely in python. In *2019 Small Satellite Conference*, 2019.
- [151] H. S. Alpert, A. S. Yalamarthy, P. F. Satterthwaite, E. Jens, J. Rabinovitch, N. Scandrette, A. Newaz, A. C. Karp, and D. G. Senesky. Gallium nitride photodetector measurements of uv emission from a gaseous CH₄/O₂ hybrid rocket igniter plume. In *2019 IEEE Aerospace Conference*, pages 1–8, 2019.
- [152] C. H. Chen, S. J. Chang, Y. K. Su, G. C. Chi, J. Y. Chi, C. A. Chang, and J. K. Sheu. GaN metal-semiconductor-metal ultraviolet photodetectors with transparent indium-tin-oxide Schottky contacts. *IEEE Photonics Tech. lett.*, 13(8):848–850, 2001.
- [153] C. K. Wang, S. J. Chang, Y. K. Su, Y. Z. Chiou, S. C. Chen, C. S. Chang, T. K. Lin, H. L. Liu, and J. J. Tang. GaN MSM UV photodetectors with titanium tungsten transparent electrodes. *IEEE Transaction on Electron Dev.*, 53(1):38–42, 2006.
- [154] Ruth A. Miller, Hongyun So, Heather C. Chiamori, Karen M. Dowling, Yongqiang Wang, and Debbie G. Senesky. Graphene-enhanced gallium nitride ultraviolet photodetectors under 2 mev proton irradiation. *Applied Physics Letters*, 111(24):241902, 2017.
- [155] J. C. Carrano, T. Li, P. A. Grudowski, C. J. Eiting, R. D. Dupuis, and J. C. Campbell. Comprehensive characterization of metal–semiconductor–metal ultraviolet photodetectors fabricated on single-crystal gan. *Journal of Applied Physics*, 83(11):6148–6160, 1998.
- [156] Hongyun So, Jongwoo Lim, Ateeq J. Suria, and Debbie G. Senesky. Highly antireflective algan/gan ultraviolet photodetectors using zno nanorod arrays on inverted pyramidal surfaces. *Applied Surface Science*, 409:91–96, 2017.
- [157] A. Yalamarthy and D. G. Senesky. Strain- and temperature-induced effects in AlGa_N/Ga_N high electron mobility transistors. *Semiconductor Sci. Tech*, 31, 2016.

- [158] A. Conte, J. Rabinovitch, E. Jens, A. C. Karp, B. Nakazono, and D. Vaughan. Design, modeling, and testing of a O₂/CH₄ igniter for a hybrid rocket motor. In *Proc. Fluid Dynamics Conference, AIAA Aviation Forum*, 2018.
- [159] Y. Cengel and A. Ghajar. *Heat and Mass Transfer*. Tata McGraw Hill, New Delhi, India, 2 edition, 2011.
- [160] J. J. Girard, R. M. Spearrin, C. S. Goldstein, and R. K. Hanson. Compact optical probe for flame temperature and carbon dioxide using interband cascade laser absorption near 4.2 μm . *Combustion and Flame*, 178:158–167, 2017.
- [161] F. S. Mechente and B. J. Cantwell. Small-scale gaseous oxygen hybrid rocket testing facility upgrades for regression rate and combustion efficiency studies. In *AIAA Propulsion and Energy 2018 Forum*, Cincinnati, OH, 2018.
- [162] F. S. Mechente and B. J. Cantwell. Experimental findings on pre- and post-combustion chamber effects in a laboratory-scale motor. In *AIAA Propulsion and Energy 2019 Forum*, Indianapolis, IN, 2019.
- [163] OSI Optoelectronics. *Dual Sandwich Detector Series*.
- [164] P. A. Beaulieu and N. A. Dembsey. Effect of oxygen on flame heat flux in horizontal and vertical orientations. *Fire Safety Journal*, 43(6):410–428, 2008.
- [165] G. Santo and F. Tamanini. Influence of oxygen depletion on the radiative properties of PMMA flames. *Symposium (International) on Combustion*, 18(1):619–631, 1981. Eighteenth Symposium (International) on Combustion.
- [166] L. Orloff, A. T. Modak, and R.L. Alpert. Burning of large-scale vertical surfaces. *Symposium (International) on Combustion*, 16(1):1345–1354, 1977.
- [167] R.O. Buckius and C.L. Tien. Infrared flame radiation. *International Journal of Heat and Mass Transfer*, 20(2):93–106, 1977.
- [168] A. Kacem, M. Mense, Y. Pizzo, G. Boyer, S. Suard, P. Boulet, G. Parent, and B. Porterie. A fully coupled fluid/solid model for open air combustion of horizontally-oriented PMMA samples. *Combustion and Flame*, 170:135–147, 2016.
- [169] D. Alibert, M. Coutin, M. Mense, Y. Pizzo, and B. Porterie. Effect of oxygen concentration on the combustion of horizontally-oriented slabs of PMMA. *Fire Safety Journal*, 91:182–190, 2017.

- [170] J. Janowitz, J. Lopez, M. Holliday, K. Dowling, B. Yeung, S. Kumar, R. Peterson, H. Alpert, C. Chapin, and D. Senesky. Deployment of InAlN/GaN Hall-effect sensors for bucket transformer monitoring and forecasting. In press.
- [171] R. Alizadeh, T. Adamson, J. C. Balda, Y. Zhao, M. Asheghi, and K. E. Goodson. A compact 50-kW traction inverter design using off-the-shelf components. In *2019 IEEE Applied Power Electronics Conference and Exposition (APEC)*, pages 2614–2619, 2019.
- [172] Y. Wang, Y. Hoole, and K. Haran. Position estimation of outer rotor PMSM using linear Hall effect sensors and neural networks. In *2019 IEEE International Electric Machines Drives Conference (IEMDC)*, pages 895–900, 2019.
- [173] *Special Topics B: Applications to Accelerated Testing*, pages 207–223. John Wiley & Sons, Ltd, 2016.
- [174] Y. Liu, Z. L. Rang, A. K. Fung, C. Cai, P. P. Ruden, M. I. Nathan, and H. Shtrikman. Uniaxial-stress dependence of hall effect in an algaas/gaas modulation-doped heterojunction. *Applied Physics Letters*, 79(27):4586–4588, 2001.
- [175] V. Mosser, F. Kobbi, S. Contreras, J. M. Mercy, O. Callen, J. L. Robert, S. Aboulhouda, J. Chevrier, and D. Adams. Low-cost 2deg magnetic sensor with metrological performances for magnetic field and current sensing. In *Proceedings of International Solid State Sensors and Actuators Conference (Transducers '97)*, volume 1, pages 401–404 vol.1, 1997.
- [176] A.V. Lalwani, A. S. Yalamarthy, H. S. Alpert, M. A. Holliday, S. R. Eisner, C. A. Chapin, and D.G. Senesky. Hall-effect sensor technique for no induced voltage in AC magnetic field measurements without current spinning. Submitted.